DOES PATIENT-SPECIFIC IMPLANT DESIGN REDUCE SUBSIDENCE RISK IN LUMBAR INTERBODY FUSION? A BOTTOM UP ANALYSIS OF METHODS TO REDUCE VERTEBRAL ENDPLATE STRESS

by

RAVI RASIK PATEL

B.S., Georgia Institute of Technology, 2013

M.S., University of Colorado Denver, 2018

A thesis submitted to the

Faculty of the Graduate School of the

University of Colorado in partial fulfillment

of the requirements for the degree of

Doctor of Philosophy

Engineering and Applied Sciences Program

This thesis for the Doctor of Philosophy Degree by

Ravi Rasik Patel

Has been approved for the

Engineering and Applied Sciences Program

By

Christopher Yakacki, Chair

R. Dana Carpenter

Kai Yu

Carl Frick

Nick Willett

Date: December 15, 2018

Patel, Ravi Rasik (Ph.D., Engineering and Applied Sciences)

Development and Evaluation of Porous Poly(para-phenylene) as an Orthopedic Biomaterial for Patient-Specific Lumbar Interbody Fusion Cages

Thesis directed by Associate Professor R. Dana Carpenter.

ABSTRACT

This research focused on the analysis of vertebral endplate stresses due to varying designs of lumbar interbody fusion cages utilizing novel polymeric materials and patient specific properties and geometry. It was hypothesized that customizing the material properties of the implant body by varying the porosity of a cage made from poly(para-phenylene), stresses on the vertebral endplate could be reduced. First a thorough study of endplate material properties was conduced to devlelop a predictive model for apparent endplate properties based on demographic and radiographic data. It was found that it was possible to successfully predict endplate stiffness and Brinell Hardness using various indices. It was found that additional information was needed to build a predictive model for apparent modulus of the endplate, likely needing a higher resolution CT scan of the vertebral body. Further, the endplate moduli measured in this study was far below those previously reported and utilized in models. As such, it provided a useful tool in analysis of endplate stresses. Next, the biological response of porous PPP was analyzed by implanting porous and solid PPP and polyetheretherketone (PEEK) implants in rat tibia. After 8 weeks, radiographic imaging revealed that porous PPP implants permitted significantly more bone ingrowth compared to PEEK (76% vs 49%). Further, modelling of pushout testing revealed substantial increase in pushout force required for porous PPP implants compared to PEEK implants, highlighting PPP's potential as an orthopedic biomaterial. Finally, utilizing the endplate material properties measured in the first study, a systematic analysis of endplate stresses

under loading for various implant designs with varying geometric design, material properties, and patient bone contouring was conducted. This study revealed that increased contact area with the bone provides the largest reduction in endplate stresses while material variation with porosity provides negligible reductions in implants with relatively high contact areas. Though the results did not demonstrate a significant result for patient specific implants, this research provides valuable insight into the mechanics of porous materials in addition to overall implant design. These results can be used to guide development in novel surgical implants for lumbar interbody fusions as the field continues to mature.

The form and content of this abstract are approved. I recommend its publication.

Approved: R. Dana Carpenter

ACKNOWLEDGEMENTS

Chapter 2 of this dissertation was published previously in the Journal of Biomechanical Engineering. Chapter 3 of this dissertation was published previously in Acta Biomaterialia. The citations for these articles are provided below. I would like to thank my co-authors in these publications for their support and effort during the publication process.

- Patel RR, Noshchenko A, Dana Carpenter RR, *et al*. Evaluation and Prediction of Human Lumbar Vertebrae Endplate Mechanical Properties Using Indentation and Computed Tomography. ASME. J Biomech Eng. 2018;140(10):101011-101011-9.
- Hyunhee Ahn, Ravi R. Patel, Anthony J. Hoyt, Angela S.P. Lin, F. Brennan Torstrick, Robert E. Guldberg, Carl P. Frick, R. Dana Carpenter, Christopher M. Yakacki, Nick J. Willett, Biological evaluation and finite-element modeling of porous poly(para-phenylene) for orthopaedic implants, Acta Biomaterialia,Volume 72,2018,Pages 352-361

I would also like to thank Ryan Anderson for his assistance with indentation testing as well as Todd Baldini, MS and Ramesh Karki for their help with cadaver preparation and storage and CT imaging respectively. Thank you to my committee members, Dr. Christopher Yakacki, Dr. Dana Carpenter, Dr. Kai Yu, Dr. Carl Frick, and Dr. Nick Willett for supporting my research and agreeing to be on my committee and providing valuable feedback despite their busy schedules. I would also like to thank the members of the SMAB Lab for always being there to bounce ideas off of and willing to blow off work to have a beer. Finally, I am gracious for the support, encouragement, and love I have received from my family and friends during my time at UCDenver.

CONTENTS

CHAPTER

I. INTRODUCTION AND BACKGROUND 1

Lumbar interbody fusion 1

Complications of Lumber Interbody Fusion 2

Issues with current cage design 4

Poly(para-phenylene) 6

Research goals 9

II. EVALUATION AND PREDICTION OF VERTEBRAL ENDPLATE MECHANICAL PROPERTIES USING INDENTATION AND COMPUTED TOMOGRAPHY 10

Introduction 10

Methods 13

Computed Tomography 14

Indentation Testing 15

Statistical Analysis 18

Results 19

Oliver-Pharr Model Validation 19

Apparent Modulus 20

Stiffness 22

Brinell Hardness 23

Maximum Load and Maximum Tolerable Pressure 24

Correlation Between Studied Characteristics 25

Modeling Mechanical Characteristics Using Radiographic and Demographic Measures 26

Discussion 31

III. BIOLOGICAL AND FINITE-ELEMENT MODELING OF POROUS POLY(PARA-PHENYLENE) FOR ORTHOPEDIC IMPLANTS 38

Introduction 38

Materials and methods 41

Material Fabrication 41

In Vivo Animal Surgery 42

Digital Radiographic Evaluation 42

Histological Analysis 43

Finite Element (FE) Simulated Push-Out Test 43

Statistical Analysis 46

Results 46

Scaffold Fabrication 46

Implant Osseointegration 49

FE Simulated Push-Out Test 51

Discussion 55

IV. EVALUATION OF VERTEBRAL ENDPLATE STRESSES UNDER LOADING WITH VARIOUS IMPLANT DESIGNS: FINITE ELEMENT GUIDED DESIGN OF LUMBAR INTERBODY FUSION CAGES WITH POROSITY AND CONTOURING 63
Introduction 63
Methods 65
Designs Tested 65
Finite-Element Modeling 66
Results 70
Endplate Stresses 70
Implant Stresses 76
Discussion 78
V. CONCLUSIONS AND FUTURE WORK 85
Future Research Suggestions 87
References 89
APPENDIX 97

LIST OF TABLES

TABLE

1. Distribution of mechanical characteristics of the tested sites. 21

2. Summary of oliver-pharr measurements for all sites tested. A, B, C levels not connected by the same letter are significantly different (p>0.05) by the Tukey-Kramer multiple comparisons test. *P-value by F-test; **P-value by Wilcoxon test. 22

3. Summary of stiffness measurements for sites tested. A, B, C levels not connected by the same letter are significantly different (p>0.05) by the Tukey-Kramer multiple comparisons test. *P-value by F-test; **P-value by Wilcoxon test..... 23

4. Summary of Brinell Hardness measurements for sites tested. A, B, C levels not connected by the same letter are significantly different (p>0.05) by the Tukey-Kramer multiple comparisons test. *P-value by F-test; **P-value by Wilcoxon test. 24

5. Spearman's correlation between the studied mechanical characteristics. 25

6. Spearman's correlation coefficient between the measured mechanical characteristics and radiographic and demographic indices. 26

7. Sensitivity, specificity, positive and negative predictive value of each model as a diagnostic tool. 27

8. Mechanical characteristics of materials used for intervertebral implant manufacturing. 36

9. Material Properties assigned to bone and scaffolds in simulated push-out test..... 44

LIST OF FIGURES

FIGURE

1. Representative examples of fusion cages. a PLIF/TLIF cage (Left) made from titanium, an ALIF cage (center) made from PEEK, and an ALIF cage made from PEEK and coated in a layer of roughened titanium. 2
2. X-ray image depicting initial height following surgery (Left) and the same vertebral segment showing implant subsidence several weeks later. The resulting position following subsidence is no longer optimal for fusion, thus requiring follow-up surgery and additional recovery time and cost to the patient. 3
3. Endplate stresses seen after loading with a circular fusion cage. A clear outline of the implant can be seen and areas of high stress at the anterior portion of the spine indicate subsidence risk. 4
4. Ashby chart comparing properties of cortical and trabecular bone with commonly used implant materials. Few materials are comparable to trabecular bone; however, porous PPP falls within the range and can be tailored to match various properties of trabecular bone.
5. Chemical structure of Poly(para-phenylene). The backbone of the polymer is primarily made up of benzene rings providing axial rigidity to the chain, while the side groups prevent rotation through steric hindrance.
6. Cartesian map of the indentation sites across the vertebral endplate. Sites were defined relative to percentages of the dimensions of the endplate. 14
7. (a)Overall indentation protocol where E is the oliver-pharr modulus assessment at the endplate surface, stiffness is the load at 1 mm of probe displacement (N/mm), maximum load was defined as the peak of the load-displacement curve (n). (b) Oliver-pharr indentation protocol where S is the unloading stiffness of the curve (n/mm), Pmax is the

maximum load achieved during the loading step (10 N), and hm is the maximum indentation depth reached in the step (mm) 15

8. A) Calculated modulus vs indentation load for 5,8, 15, and 20 PCF sawbone foam blocks. It was found that a 10N indentation load allowed for the most accurate measurement of modulus. B) Experimental Experimentally measured and literature reported moduli for varying density polyurethane foam blocks. A strong correlation is seen between the moduli measured from indentation and those reported by the manufacturer. 19

9. Representative load-displacement curves for oliver-pharr measurements for specimens within the top 10% (404 MPa), top 25% (208 MPa) and bottom 50% (106 MPa) of all test data. 20

10. Representative stiffness curves for common spinal cage materials and vertebral endplates. The two bottom curves are representative of the top 10% of tested endplates and top 50% of endplates respectively. PEEK and cortical bone are shown to be stiffer than even the stiffest endplates 22

11. Correspondance between the predictive stiffness model and stiffness measured from indentation. Stiffness was modeled as a function of endplate thickness, endplate density, adjacent cancellous bone density, the presence of endplate defects, and patient age. The model showed a correlation of r^2=0.72 with the measured indentation stiffness. 27

12. Correspondence between predicted hardness and hardness measured from indentation. Brinell hardness was modeled as a linear and polynomial model using endplate density, endplate thickness, presence of and endplate defect, and patient weight. The linear fit used the equation y_{BH}=-2.9+0.002X_1+0.0011X_2+0.008X_4 where y_{BH} is the linear approximation of Brinell Hardness, X_1 is the endplate mineral density (mg/mm^3), X_2 is the

endplate thickness (μm), X_3 is the presence of an endplate defect or herniation (yes/no=±0.1), and X_4 is patient weight (kg). The polynomial fit was described by the equation $Y_{BH}=0.06 + 0.85\ y_{BH} + 0.36(y_{BH}-0.98)^2$ where Y_{BH} is the polynomial approximation of Brinell Hardness, and y_{BH} is the linear approximation obtained from the first equation. The linear fit showed a correlation of $R^2=0.64$ while the polynomial fit showed a correlation of 0.68 with the measured hardness values. 28

13. Correspondence between predicted apparent modulus and apparent modulus measured from indentation. Apparent Oliver-Pharr Modulus was modeled using endplate density, presence of endplate defects, and patient weight. Modulus was modeled using the equation $E= -71.35 + 1.57X_1 + X_2 \_0.092X_3$ where E is the linear approximation Oliver-Pharr modulus (MPa); X_1 is the patient weight (kg); X2 is the presence of an endplate defect or herniation parameter (yes/no=±19.3), and X_3 is the endplate mineral density (mg/mm3). The linear model showed a correlation of $R^2=0.19$. 29

14. Bland-Altman analysis of each model. the Y-axis of each graph shows the difference between the modelled and measured mechanical property and the x-axis shows the average of the two methods. Points should be randomly distributed vertically across the full range of values measured. Stiffness (top left) shows a well fitted model as points are distributed randomly above and below the 0 line. Modulus (top right) shows a model requiring additional information to fit the data well. Both hardness MODELS (bottom) demonstrate a well fitted model. The polynomial model shows a slight artifact at low hardness values, but the rest of the model fits the measured values well. 30

15. Depiction of equally spaced intervals for stress dissipation measurement. 45

16. Representative image of simulated ingrowth into a porous scaffold. Ingrowth was simulated from 0 to 100% infill layers contouring the inner surfaces of the pores. 45
17. Representative images of implants. Micro-CT (top), Cylindrical implants for insertion in rat tibia (middle), and disk-shaped cylinders for cell culture (bottom). 47
18. Surface roughness for each type of implant. No significant differences between each type was measured 47
19. Trabecular thickness measurements for pPPP (left) and pPEEK (right). Areas shown in black are pores within the implant and colored areas depict a heatmap of trabecular thickness of the implants. 48
20. Bone ingrowth throughout porous materials, especially PPP showed significantly increased bone ingrowth. A) in vivo x-ray radiographs post-surgery. B) representative micro-CT reconstructions of the same specimens from x-ray images. C) quantitative measurement of mineralized bone volume of implants. Solid scaffolds showed no significant difference of BV between groups. Porous PPP explants showed significantly increased BV value compared to any other explants *$p<0.05$; **$p<0.0001$; $n=6$; data presented as mean ± SEM 49
21. Histological analysis of bone ingrowth in implants. A) Coronal slices of implants with surrounding tissue. B) Magnified images of the same regions. Notably, pPPP showed enhanced cellularization and substantial bone formaiton. MB- mature bone (stained as pink in MF/AF staining or purple to green from Goldner's trichrome.; M- material (stained as brown); OS- Osteoid seam (red arrow); F-Fibrotic tissue (Black arrow); Osteocyte (yellow arrow); BM (bone marrow); P (implant pore) 50

22. Total pushout force and load sharing behavior of solid/porous PEEK and PPP. Reaction forces from the bone and implant were taken to determine load sharing. Porous PPP showed significantly higher push-out force than porous PEEK. Load sharing between bone and implant in porous scaffolds was nearly identical. Both solid scaffolds showed identical push-out force with all force transmission through the implant as there was no bone ingrowth. 52

23. Stress dissipation within scaffolds during simulated push-out testing. heatmaps of von Mises stress within each scaffold type (left) showed little stress in the center of the implant for solid PEEK and PPP while both porous scaffolds showed high stress at the top of the implant which then dissipates moving through the implant. Average stress in the implant at equally spaced intervals (right) in the implant show porous PPP and PEEK having similar stress dissipation responses while there is no dissipation within the solid implants. 53

24. Apparent modulus of various porosity PPP implants as a function of bone ingrowth. 54

25. Load sharing percentage for 50, 60, and 85% porous ppp implants. hollow Markers indicate load through the implant while solid markers indicate load through the bone..... 55

26. Design matrix depicting all implant designs and material variations tested..... 66

27. Representative image of the finite element model used in the study. The separately segmented endplate can be seen below the traditional geometry implant. 67

28. Heatmap of interpolated modulus on the endplate utilized in the finite element model. .. 68

29. Stress heatmaps of the endplate after loading with various implant designs..... 70

30. A) Box and whisker plot of endplate stresses for each implant design tested. B) box and whisker plot of endplate stresses for all designs tested. 74

31. Average endplate stress for each implant type normalized to average endplate stress for the traditional solid implant..... 74

32. Contact area between the bone and implant following loading for each implant design vs normalized average stress. A diminishing response is seen with increased contact area beyond approximately 50 mm^3. Changes in material within a given implant geometry do not appear to have a large effect on average endplate stresses. 75

33. Heatmaps of stress within the implant body. stresses greater than 5MPa are shown as red. It can be seen that stresses are highest in traditional solid implants. Conformed implants show the lowest stresses for any design type and increasing porosity..... 76

34. Distribution of stresses within the implant body for various implant designs. Whiskers represent the 90th and 10th percentiles, boxes represent 70th (top), median (center), and 25th (bottom) percentiles..... 77

CHAPTER I

INTRODUCTION AND BACKGROUND

Lumbar interbody fusion

Lumbar interbody fusion (LIF) is one of the most common surgical procedures performed in the United States, with over 267,000 procedures performed annually. This number is expected to grow to over 350,000 by 2023..[1] Fusion surgery is typically used for treatment of severe lower back pain due to degenerative disc disease, disc herniation, trauma, or other pathologies of the disc or intervertebral space. Typical costs for the treatment range between $40,000 to $54,000 over two years, including all follow-up visits. The ultimate goal of any fusion surgery is the decompression of the disc space, restoration of the natural disc height, and reducing impingement of neural bundles exiting the spinal cord between the vertebrae.

Surgeons have a wide variety of choices regarding approaches to the spine for lumbar fusion. Depending on patient anatomy, age, bone density, or number of vertebral segments requiring fusion, the surgeon may opt for one approach over another. The most common approaches currently used are posterior (PLIF), anterior (ALIF), and transforaminal (TLIF) lumbar interbody fusion, which describe the direction of approach to the disc space. Each procedure has advantages and disadvantages compared to others, but the ultimate goal for all procedures is reduce patient pain by restoring healthy disc height following fusion. During the procedure, an implantable device called an interbody spacer, or cage, is inserted into the disc space to restore disc height. The procedure achieves this by minimizing motion in the vertebral space by preventing axial, bending, and rotational motion across the intervertebral space, allowing for bone formation, fusing the two vertebra into a single bone.Each approach can

require a different cage design for optimal placement during the procedure; however, cages are generally made of a solid material such as polyetheretherketone (PEEK), titanium, or stainless steel, and most designs include large holes within the implant to hold bone graft material to

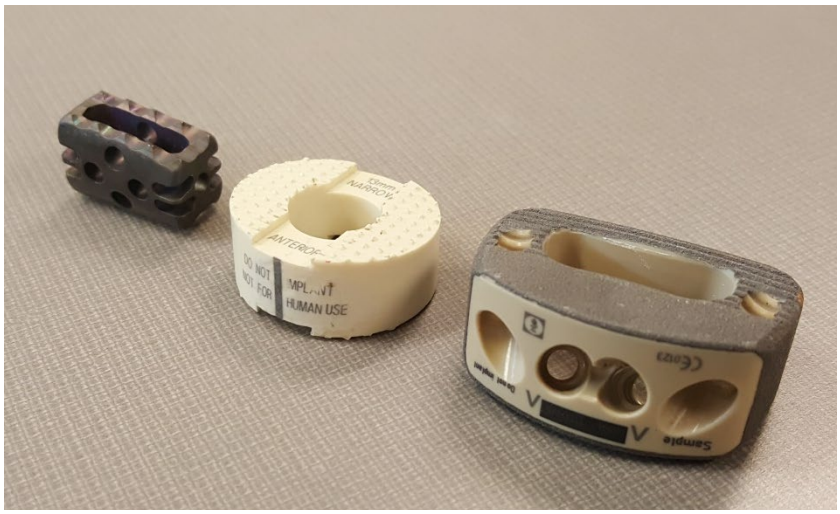

Figure 1: Representative examples of fusion cages. a PLIF/TLIF cage (Left) made from titanium, an ALIF cage (center) made from PEEK, and an ALIF cage made from PEEK and coated in a layer of roughened titanium.

enhance bone ingrowth following implantation. Representative examples of various implant designs can be seen in **Figure 1**. ALIF cages are typically the largest, as they are inserted from the anterior side of the disc, which has the largest opening. PLIF and TLIF cages are typically used in minimally invasive procedures from the posterior portion of the spine, and as such, are typically much smaller, as they must be inserted through smaller incisions, and multiple implants are often used rather than a single large one. Further, the implants may be supplemented with posterior fixation rods and pedicle screws to provide additional support and reduce loading on the vertebra.

Complications of Lumber Interbody Fusion

The most common complication seen in LIF procedures is subsidence, or the loss of disc height due to the implant sinking into or fracturing the vertebral endplate. An x-ray image of a subsided disc can be seen in **Figure 2**. The implant can be seen to have cut into the endplates

and the intervertebral space has been significantly reduced from the initial height following surgery. Subsidence rates vary significantly depending on patient anatomy, bone density, as well as implant type, often ranging from 17% up to 57% in some studies.[2,3] The exact mechanisms behind subsidence are unclear; however, several risk factors have been identified in the literature. Namely, a large mismatch in mechanical properties between the implant materials and endplate properties has been shown to significantly increase the risk of subsidence. In a biomechanical study of various implant materials, Vadapalli *et al*. found that decreasing the implant modulus by switching from titanium (E=110 GPa) to PEEK (E=3-5 GPa) cages significantly reduces stresses on the endplate and allows better load sharing with the bone graft material.[4] It is believed that reducing the modulus of the implant to be closer to that of the natural bone reduces the risk of subsidence.

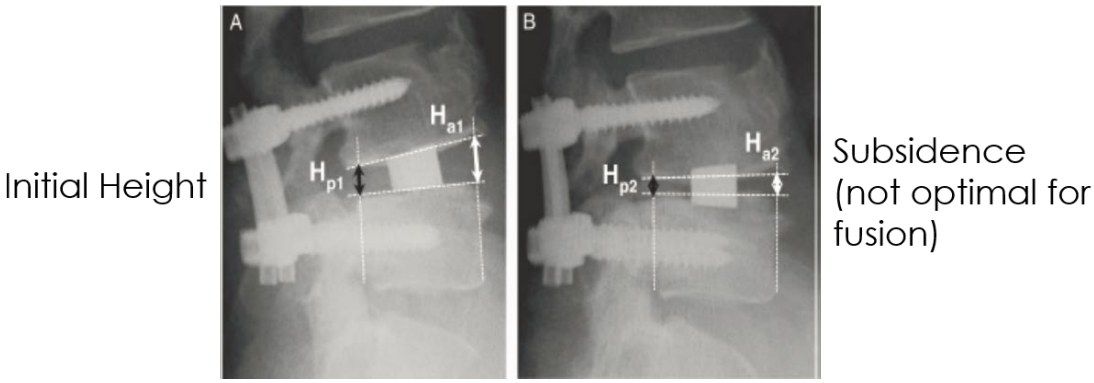

Figure 2: X-ray image depicting initial height following surgery (Left) and the same vertebral segment showing implant subsidence several weeks later. The resulting position following subsidence is no longer optimal for fusion, thus requiring follow-up surgery and additional recovery time and cost to the patient.

Other studies have suggested that subsidence can be due to accumulation of micro-damage at the implant-bone interface, and that this damage can lead to permanent deformation of the endplate.[5,6]

Typical onset times of subsidence after fusion surgery are between 6 weeks and 8 months. In a prospective study using an anterior approach, cage subsidence was seen at a median time of

2.75 months following surgery. Further, this study found that the risk of developing implant subsidence greater than 2 mm to be as high as 70.7% after 4 months.[7] As the majority of subsidence happens early in the fusion process, it is critical that the implant not be unduly loaded or undergo excessive motion during this time, as the contact area is limited to that of the implant surface, which can lead to stress concentrations at the endplate surface. For example, a representative endplate is shown in **Figure 3** after loading with a circular ALIF implant. The stresses are primarily concentrated around the periphery of the implant-bone interface, which would indicate areas of high subsidence risk.

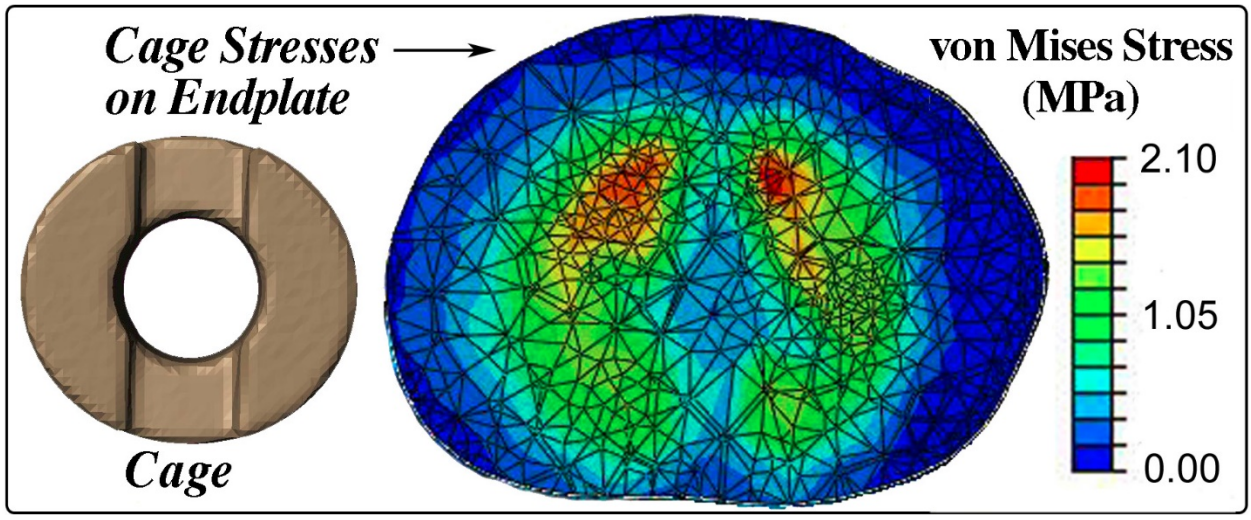

Figure 3: Endplate stresses seen after loading with a circular fusion cage. A clear outline of the implant can be seen and areas of high stress at the anterior portion of the spine indicate subsidence risk.

Issues with current cage design

Developing implants for the lumbar spine poses a unique problem in that vertebral bodies have a unique structure not seen in other bones. The majority of the volume of a vertebra is made up of low-density cancellous bone surrounded by a thin shell of cortical bone. This leads to the vertebral body having mechanical properties which vary significantly across the surface as well ones which behave similarly to a composite or structural material.

Current cages are typically made of solid materials such as PEEK and titanium, which have moduli significantly higher than the vertebral endplate. With these high-stiffness implants, subsidence often occurs due to the significant mismatch between the bone and implant material properties. Researchers have suggested that materials which can more closely match the bone stiffness would be beneficial to provide a better fusion construct. Van Dijk *et al*. found that vertebral trabecular and cortical bone have average moduli of 2.1 and 2.4 GPa, respectively, while typical materials used in fusion cages range between 4 and 200 GPa. The study suggested that these high-stiffness implants hinder proper fusion and bone ingrowth.[8,9] Other studies have also found similar responses when analyzing high modulus implants.[10] An Ashby chart

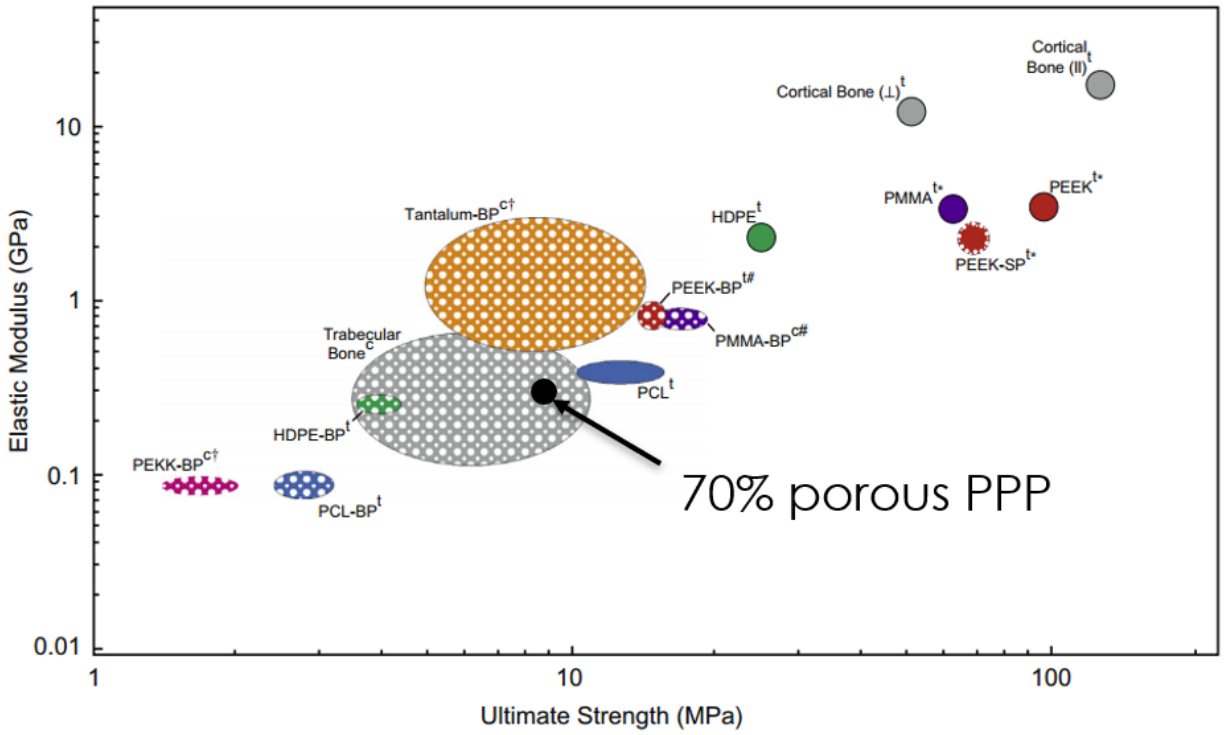

Figure 4: Ashby chart comparing properties of cortical and trabecular bone with commonly used implant materials. Few materials are comparable to trabecular bone; however, porous PPP falls within the range and can be tailored to match various properties of trabecular bone.

depicting commonly used materials for cages and trabecular bone can be seen in **Figure 4**. It can be seen that there are very few materials which fall within the range of trabecular bone.[11]

Current developments in the spinal device field are trending towards implants with materials closer to that of natural bone; however, there are few materials which can achieve this goal whole maintaining mechanical integrity.

Medical device companies are currently developing novel materials which attempt to minimize the mechanical property differences between cage materials and the native bone. Currently, implants have been developed which utilize porous materials to reduce the modulus of the implant. For example, NuVasive has developed a novel surface porous PEEK cage which lowers the modulus to approximately 3.36 GPa. Stryker developed a porous titanium cage which lowers the modulus to approximately 6.6 GPa. While an improvement compared to traditional cages, these implants are still significantly stiffer than the surrounding bone. In a numerical simulation of bone ingrowth following fusion surgery, Bashkuev *et al*. found the optimal implant modulus to promote bone ingrowth in the spine to be a cage with a modulus of approximately 500 MPa which then decreases as more bone grows into the material.[12] Their modelling demonstrated that current implant materials are significantly stiffer than the optimal cage. However, with current materials, this is difficult to achieve sufficient stiffness without sacrificing structural integrity within the implant. There are significant advances which need to be made in the realm of orthopedic biomaterials in this field. There is a need for a new material which can achieve these low moduli while still maintaining mechanical integrity.

Poly(para-phenylene)

Poly(*para*-phenylene) (PPP) is a novel, high-strength polymer with exceptional properties. It was first synthesized as a powder in 1963; however, the polymer was not easily processible for manufacturing on large scales. In 2003, Mississippi Polymer Technologies developed a modified PPP which was melt processible and was subsequently acquired by Solvay Specialty

Polymers in 2006.[13] A molecular diagram of this PPP is shown in **Figure 5**. The rigid backbone made up from benzene rings provides significant resistance to chain bending as well as steric hindrance from the side groups preventing chain rotation around the alkyl-alkyl bonds. PPP has shown significant promise as an orthopedic biomaterial due to its high modulus (5,520 MPa), yield strength (175 MPa), as well as its biocompatibility (as confirmed by ISO 10993 testing).[14-16] Additionally, PPP is currently the strongest unreinforced polymer commercially available.

The primary benefit of utilizing PPP in an orthopedic implant is the ability to introduce higher porosity compared to currently used materials without sacrificing mechanical integrity of the implant. As PPP has a significantly higher modulus than PEEK (the current gold standard of

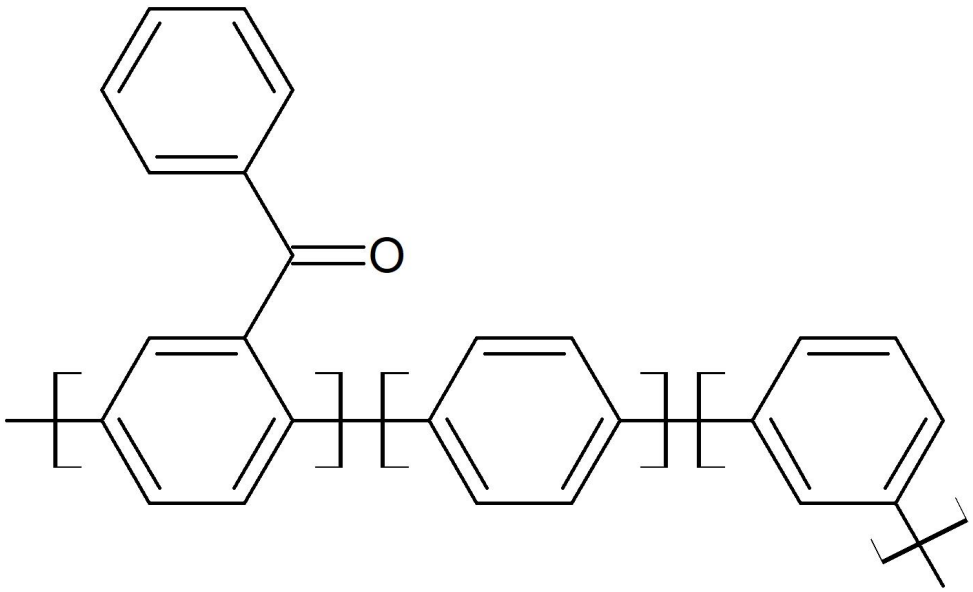

Figure 5: Chemical structure of Poly(para-phenylene). The backbone of the polymer is primarily made up of benzene rings providing axial rigidity to the chain, while the side groups prevent rotation through steric hindrance.

implantable polymeric biomaterials), one can introduce higher porosity into the material while achieving the same overall modulus. Further, with its increased yield stress compared to PEEK, PPP is less likely to yield at these higher porosities, allowing for a structurally sound implant with porosity throughout the material. In addition to its benefits over current polymers, PPP

provides additional benefits when compared to traditionally used metals as well. Namely, metallic implants typically have moduli approximately 2 orders of magnitude higher than the natural bone, which can lead to local stress concentrations as well as shielding bone from stress, a loading condition not particularly conducive to healthy fusion. Additionally, metal implants can lead to significant imaging artifacts in both magnetic resonance imaging (MRI) and computed tomography (CT). Conversely, PPP is radiolucent and does not interfere with common imaging modalities.

In a preliminary study of PPP as an orthopedic biomaterial, Yakacki *et al*. found that 70% porous PPP closely matched the mechanical properties of trabecular bone; additionally, the study quantified the mechanical properties of porous PPP for porosities ranging from 50 to 90%. An Ashby chart of various implant materials and bone can be seen in **Figure 4**. There is little overlap between any commonly used implant materials with trabecular bone; however, 70% porous PPP falls within the range of trabecular bone. By tailoring the porosity, a wide range of properties can be produced.

With the ability to vary porosity to control the mechanical properties of a PPP scaffold, it is logical to assume this material can be applied in an orthopedic implant; however, there are several factors which must first be analyzed to achieve this ultimate goal. Primarily, the material properties of the endplate are not fully understood at a scale level relevant to implant design. In order to create a patient-specific implant, there must be a strong understanding of the endplate mechanical properties and how they relate to the implant. Further, the osseointegrative behavior of PPP scaffolds has not previously been studied and must be analyzed to determine the behavior of PPP in-vivo.

Research goals

The ultimate goal of this research is to develop a fully porous patient-specific, spinal cage which minimizes subsidence by reducing stress concentrations on the endplate. In order to do this, there are three primary goals which must be achieved. First, we must develop a predictive model which allows for the estimation of endplate mechanical properties non-invasively. The application of this device in a clinical setting would require the ability to predict a patient's endplate modulus and strength and creating an implant accordingly. Secondly, as PPP has not been previously studied in-vivo for osseointegration or orthopedic implants, we must study its behavior in an osseointegration model to determine the rate of bone ingrowth and its effects on mechanical behavior of the material after implantation. Finally, using the information garnered from the two previous studies, an implant design which minimizes endplate stresses must be developed. In this research, a finite-element guided design method was used to rapidly explore the various effects of implant geometry and material properties on endplate stresses.

CHAPTER II

EVALUATION AND PREDICTION OF VERTEBRAL ENDPLATE MECHANICAL PROPERTIES USING INDENTATION AND COMPUTED TOMOGRAPHY

Introduction

Intervertebral arthrodesis (fusion) is one of the most effective treatment methods for lower back pain due to severe degenerative disc disease, herniation, and other pathologies affecting the disc and intervertebral space.[17] Over 267,000 surgical interventions of the lumbar and lumbosacral levels are performed annually in the United States, and this number is expected to climb to 350,000 by 2023.[1,18] Treatment costs range between $40,000 and $54,000 over two years.[19-21] Revision surgery is required in 15 to 17% of cases, often doubling the cost.[22,23] Additionally, the loss of disc height due to subsidence (i.e. the device sinking through the endplate) causes loss of correction in approximately 30% of the operated cases.[23,24] In cases of subsidence, the patient often requires additional surgery to restore the original corrected disc height If left uncorrected, the vertebrae may fuse improperly - leading to further complications and increased pain and cost to the patient.

A stronger understanding of the mechanical properties of the endplate is necessary for the development of effective implant designs that minimize and avoid subsidence. A method to predict mechanical properties such as hardness, stiffness, and modulus would allow clinicians to assess the risk of subsidence and other complications following surgery which are often due to weak bone and low mechanical strength of the endplate. Additionally, it would permit surgeons to determine the optimal implant placement to avoid areas susceptible to subsidence. It is generally known that the vertebral body is primarily made up of trabecular bone with a thin cortical shell, decreasing the mechanical integrity of the vertebra compared to solid bone. Pores within the bony endplate often decrease its stiffness and strength due to decreased cortical bone

thickness.[25-27] Additionally, current implant materials are often orders of magnitude stiffer and stronger than the native bone as guided by current design standards that are focused on minimizing failure of the implant material rather than the bone.[28] Current surgical practices further compound this mechanical property mismatch as the bony and cartilagenous endplates are often debrided to elicit bleeding and healing in the intervertebral space during surgery exposing the weaker underlying trabecular bone.

The overwhelming majority of studies investigating endplate mechanical properties have either performed measurements at the microscopic scale or used metrics which are not directly comparable to implant material properties.[29-32] For example, it is common to measure the modulus of the vertebral endplate bone tissue by nano- and micro-indentations of solid bone microstructures within the endplate.[29] However, properties measured using these techniques do not accurately capture the behavior of the endplate as it relates to its interaction with implants at the macroscopic scale. Rather, at this scale, the structure of the bone has a greater influence on the mechanical integrity of the endplate, and microindentation cannot capture the gradients in properties or composite interaction of cortical and trabecular bone regions. The contributing effects of bone defects, endplate thickness, and underlying trabecular bone structure are lost when performing indentation at the microscopic scale. Other studies have investigated the macroscopic properties of the endplate using a 3mm spherical indenter;[30-32] however, these studies measured properties, such as stiffness, which are not directly relatable to materials used in implants and are dependent on indenter geometry. Although stiffness has thoroughly been investigated in the endplate, it only allows for a general understanding of the endplate structure, whereas characterizing the endplate using traditional mechanical properties such as modulus and hardness would facilitate a direct comparison to implant materials. In previous studies, stiffness

was defined as a function of axial load provided by penetration of a 3 mm diameter hemispherical probe through the endplate.[31,32] It was shown that the stiffness is highly variable, ranging from 4.6 N/mm to 390 N/mm across the endplate and is typically higher at posterior and lateral locations. It was also found that whole vertebral body stiffness can be predicted using bone mineral density from computed tomography (*CT)*; however, these models do not account for bone defects, which significantly affect the modulus at the endplate-implant interface. [33] Additionally, stiffness measurements do not account for any time-dependent behavior of the endplate bone, where the combined contributions of elastic, plastic, and viscoelastic responses of the vertebral bone need to be quantified in order to fully understand the mechanical behavior of the endplate with regard to implant loading. Furthermore, these properties have only been quantified using techniques available for ex-situ studies in cadavers, but in order to use the endplate in a clinical setting, a method for predicting the properties of the endplate *in vivo* is required. A non-invasive method that uses currently available clinical tools and practices is necessary to estimate the properties of the endplate and predict the performance of implants following surgery, as it is not clinically feasible to directly measure the endplate properties of individual patients.

This study will introduce an indentation method to help separate and compare the elastic, plastic, and viscous effects in the vertebral endplate and correlate these effects using predictive parameters from clinical CT and demographic data. The purpose of this study is to develop a predictive model for endplate mechanical properties at a scale relevant to implant design and behavior. Specifically, this study seeks to build predictive mathematical models to predict modulus, stiffness, and Brinell Hardness from demographic and radiographic data. Brinell Hardness is a measure of the strength of the material as it transitions from elastic to plastic

deformation, while Oliver-Pharr modulus captures the elastic response of a material during indentation and allows for visualization of the viscoelastic effects of loading on the bone. Brinell Hardness is a very commonly used standard engineering material metric and allows for direct comparison between materials as it is easily quantifiable. The same is true for the apparent modulus as these material properties are often used to directly characterize engineering materials. It should be noted that the modulus, calculated from indentation using the Oliver-Pharr model, and Brinell Hardness have not been previously reported for the vertebral endplate. Further, the Oliver-Pharr modulus calculated in this study should be viewed as an apparent or effective modulus, as it is a measure of the overall behavior of a structure's mechanical properties and allows for direct comparison of the endplate properties to implant materials. Additionally, this study seeks to challenge the current paradigm of implant material and its relationship to bone mechanics.

Methods

Whole lumbar spine specimens (T12-S1) from 10 cadaveric donors (5 male and 5 female; age range, 44-65 yr.) with no cardiovascular or degenerative bone disease were obtained from Science Care (Phoenix, AZ, USA) and placed in a -20°C freezer upon delivery. Dual-energy x-ray absorptiometry was performed using a Discovery W DXA instrument (Hologic Inc, Waltham, Massachusetts, USA) on whole spines to define bone status and bone mineral density (g/cm^2) of each vertebra. Then conventional *CT* of each spine was performed (see detailed description below).

Each spine was thawed (0-4°C) and the L1 and L2 vertebrae gently separated. Soft tissues and the cartilaginous endplate were carefully removed by dissection with a small scalpel, leaving the bony endplate and cortical shell intact. Twenty vertebrae (10 L1; and 10 L2) were wrapped in

wet gauze to prevent drying. During preparation, each tested site was marked according to a Cartesian map (**Figure 6**) and photographed to guide the indentation test and *CT* images analysis; indentation testing was then performed to define stiffness, apparent Oliver-Pharr modulus, maximum tolerable pressure (*MTP*), and Brinell hardness of both cranial and caudal endplates of each vertebra.

Computed Tomography

Computed tomography was performed using a Gemini TF 64 (Philips Healthcare, Cleveland, OH, USA) scanner at 120 kVp with a slice thickness of 0.67 mm, interslice spacing of 0.33 mm, and in-plane resolution of 0.68 mm. Regions of interest for analysis at cranial and caudal surfaces of each vertebra were identified according to the Cartesian coordinate system defined in **Figure 6**. A detailed method for *CT* image analysis has been published previously.[32]

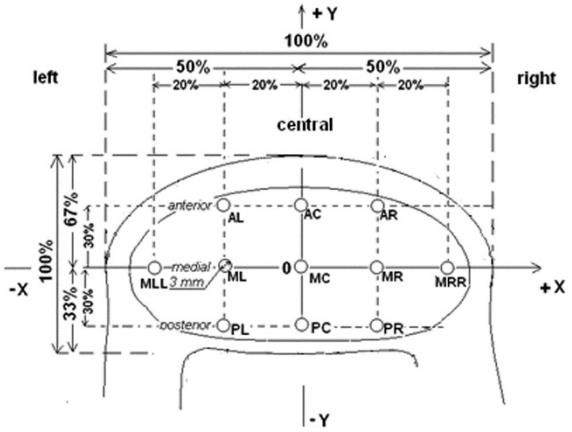

Figure 6:Cartesian map of the indentation sites across the vertebral endplate. Sites were defined relative to percentages of the dimensions of the endplate.

The following characteristics were defined at each test site: endplate thickness (μm), endplate mineral density (mg/mm^3), mineral density of underlying trabecular bone (mg/mm^3), and presence of endplate defects (e.g. local concavity, fracture, or other defects which affect the normal anatomy of the endplate) (yes/no). Hounsfield units were converted into bone mineral

density (mg/mm^3) using a calibration phantom provided by the manufacturer which displays known bone mineral densities allowing for direct conversion from Hounsfield units to mg/mm^3.

Indentation Testing

The procedures related to preparation and indentation of the vertebrae closely followed a study by Noshchenko *et al*. [32] The endplates were tested in a mechanical testing machine (MTS, Eden Prairie, MN, USA). Eleven sites were tested on each surface using a 3 mm diameter hemispherical aluminum indenter. The indentation test had two stages. The first stage measured the apparent modulus of the endplate surface.[34,35] The endplate was indented to a load of 10 N at a rate of 0.05 mm/s and held for 30 seconds and then unloaded at the same rate and held for 30 seconds (**Figure 7, a** and **b**). This loading rate was chosen to minimize overshoot during the 10

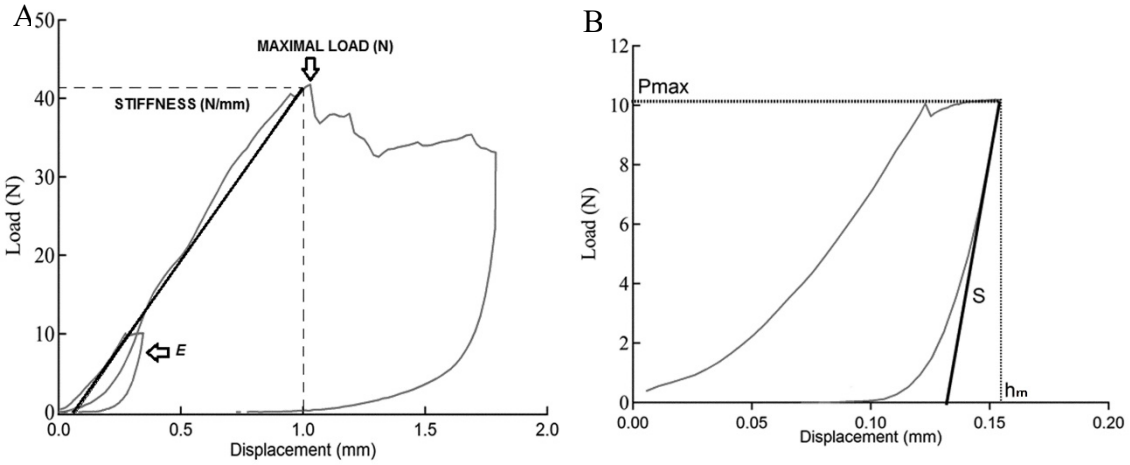

Figure 7: (a)Overall indentation protocol where E is the oliver-pharr modulus assessment at the endplate surface, stiffness is the load at 1 mm of probe displacement (N/mm), maximum load was defined as the peak of the load-displacement curve (n). (b) Oliver-pharr indentation protocol where S is the unloading stiffness of the curve (n/mm), Pmax is the maximum load achieved during the loading step (10 N), and hm is the maximum indentation depth reached in the step (mm)

N holding phase. The second stage then evaluated the stiffness, maximum load, MTP, and Brinell hardness by pressing the probe into the bone at a speed of 0.2 mm/s to a depth of 1.8 mm. Data was recorded at a rate of 10 Hz. This method was chosen to match that of previous indentation studies measuring stiffness.[31,32] This method was also used to measure the stiffness

of commonly used materials for spinal fusion cages made from *PEEK* and cortical bone rings for comparison of stiffness in a clinical application.

The apparent Oliver-Pharr modulus was calculated using the unloading stiffness after the 10 N holding period.[35] The unloading stiffness was defined as the slope of first 4 data points, or approximately 30%, of the unloading curve and measured in N/mm (**Figure 7b**).[36] Then the resultant modulus, E_r, was calculated as:

$$E_r = \frac{\sqrt{\pi}S}{2\sqrt{\pi(2Rh_c - h_c^{\,2})}} \quad , \tag{1}$$

where S is the unloading stiffness (N/mm); R is the radius of indenter (1.5 mm); $\pi \approx 3.14$; h_c, is the contact depth of the indenter tip, as defined by:

$$h_c = h_m - 0.75\frac{P_m}{S} \quad , \tag{2}$$

where h_c is the contact depth; h_m is the probe displacement (mm) at the maximum load of 10 N (**Figure 7b**); P_m is the load at maximum displacement (10 N); and S *is* the unloading stiffness (N/mm). Then, the apparent modulus was defined as:

$$E_s = \frac{1 - v_s^{\,2}}{\frac{1}{E_r} - \frac{1 - v_i^{\,2}}{E_i}} \quad , \tag{3}$$

where E_s is the apparent endplate modulus; v_s is the Poisson ratio of the endplate; v_i is the Poisson ratio of the indenter (0.33); E_r is the resultant modulus; and E_i is the modulus of indenter tip (70 GPa). It should be noted that the Oliver-Pharr method is relatively insensitive to variations in the Poisson's ratio, and the exact value of Poisson's ratio of the endplate is involved to determine; therefore, a constant value of 0.3 was used for all samples in this study.[37] Additionally, it is

assumed that during loading, the sample undergoes both plastic and elastic displacement, whereas, during unloading, the sample simply recovers the elastic deformation.

The Oliver-Pharr model used in this study was validated for the indentation method using polyurethane foam blocks used to simulate bone properties. Polyurethane foam blocks (Sawbones USA, Vashon Island, WA) with densities ranging from 5 pounds per cubic foot (PCF) to 20 PCF. Indentations were performed at loads ranging from 10N to 100N to determine the most accurate loading to measure modulus. Moduli calculated using each loading method were compared to the manufacturer reported values as well as those measured experimentally.

Methods of the maximum load and the *MTP* assessment are described as SM: **§S2**. In brief, the maximal load was taken as either the load at which the endplate failed or the load at the maximum indentation depth of 1.8 mm, and MTP was calculated as the maximal load divided by the cross-sectional area of the indenter.

The stiffness was defined as the load at 1 mm of the probe displacement to be in line with methods from previous studies (N/mm; **Figure 7a**).[32]

Brinell hardness was calculated as:[38]

$$HB = 0.102\frac{2F_m}{\pi D(D-\sqrt{D^2-d^2})} \tag{4}$$

and

$$d = 2*\sqrt{h(D-h)} \tag{5}$$

where *HB* is the hardness in units of Brinell scale; F_m is the maximum load (N)*; D* is the indenter tip diameter (3 mm); *h* is probe displacement (mm) at maximum load (**Figure 7a**); *d* is the diameter of indented probe tip at the maximum load, defined as a function of the probe

displacement: equal equation (5), if displacement (h) was < 1.5 mm; and 3 mm, if displacement was ≥ 1.5 mm.

Statistical Analysis

An analysis of distributions and variance was performed to characterize the studied numeric variables, the Wilcoxon test was applied to evaluate differences between 2 subgroups, and for multiple comparisons (more than 2 subgroups), Fisher and Tukey-Kramer tests were used.[39] Indentation data was pooled across all indentation locations and specimens. Correlations between mechanical, radiographic, and demographic characteristics were defined by the nonparametric Spearman's rank correlation coefficient.[39] Multiple regression analysis was performed to select optimal combinations of the radiographic and demographic parameters to develop a predictive model of studied mechanical properties. Linear and nonlinear approximations were applied and tested using the JMP-7 program (SAS, Cary, NC, USA). Correspondence between modeled and experimental values was defined by Pearson's correlation coefficient (r), coefficient of determination (r^2), root mean square error (RMSE), and p-value.[39] Sensitivity, specificity, positive and negative predictive values were defined to evaluate diagnostic abilities for each developed model.[39]

The modeling of stiffness was performed using the previously published equation:[32]

$$E(e) = -2.2 + 0.94y + 0.0045(y - 74.8)^2 \quad , \qquad (6)$$

where *E(e)* is a modeled equivalent of the stiffness (N/mm), and y is a function of radiographic and demographic characteristics defined as:

$$y = -360.8 + 0.11X_1 + 0.255X_2 + 0.025X_3 + X_4 - 0.07X_5 \quad , \qquad (7)$$

where X_1 is endplate thickness (μm); X_2 is density of the endplate (mg/mm^3); X_3 is adjacent cancellous bone apparent density (mg/cm^3); X_4 is existence of endplate defects or herniation parameter (yes, -5.5; no, +5.5); and X_5 is the age of the donor (yrs.*)*. These equations were determined using multiple regression analysis with demographic and radiographic measures. The correspondence between indentation results in this study and stiffness predicted by these equations was measured in this study.

Results

Oliver-Pharr Model Validation

A graph showing calculated modulus as a function of indentation load is shown in **Figure 8A**. Each density showed increasing modulus calculations as the hold load during indentation was increased. The 5 and 8 PCF samples were not able to resist higher loading, and as such were

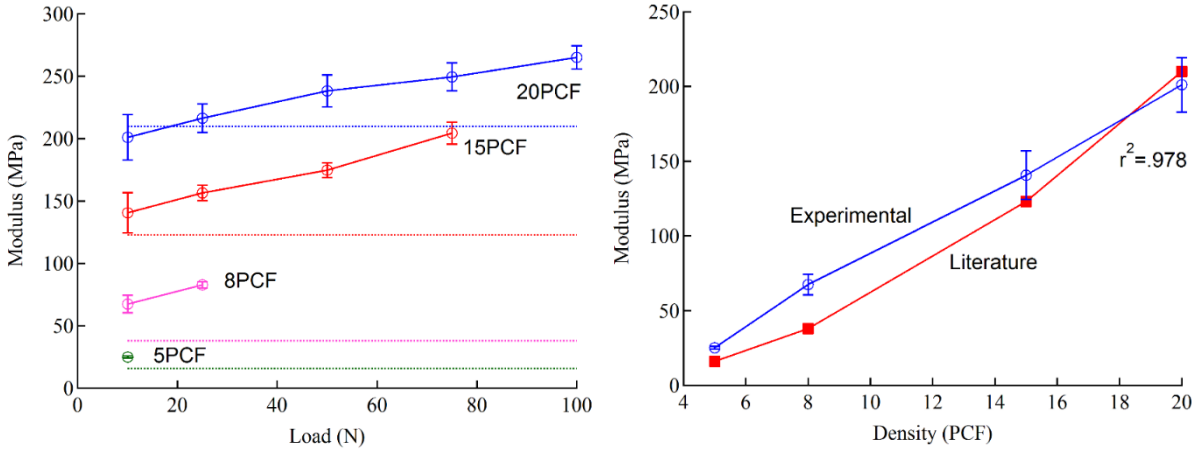

Figure 8: A) Calculated modulus vs indentation load for 5,8, 15, and 20 PCF sawbone foam blocks. It was found that a 10N indentation load allowed for the most accurate measurement of modulus. B) Experimental Experimentally measured and literature reported moduli for varying density polyurethane foam blocks. A strong correlation is seen between the moduli measured from indentation and those reported by the manufacturer.

only able to be reported at low indentation loads. Horizontal lines in the graph represent the true modulus of the foam as reported by the manufacturer and verified experimentally. From these results it was determined that a 10 N holding load during indentation provided the most accurate results for modulus calculation on the endplate. Using this loading, the reported values and

measured values were compared and showed a strong correlation (r^2=0.97). A graph of the literature and measured modulus values as a function of foam density is shown in **Figure 8B**. Both experimental and literature moduli showed a linear relationship between density and measured modulus as would be expected.

Apparent Modulus

Representative indentation results used to calculate the apparent Oliver-Pharr modulus are shown in **Figure 9;** these three curves represent the behavior seen from the top 10%, top 25%, and bottom 50% of the specimens with respect to the apparent modulus values of all tests.

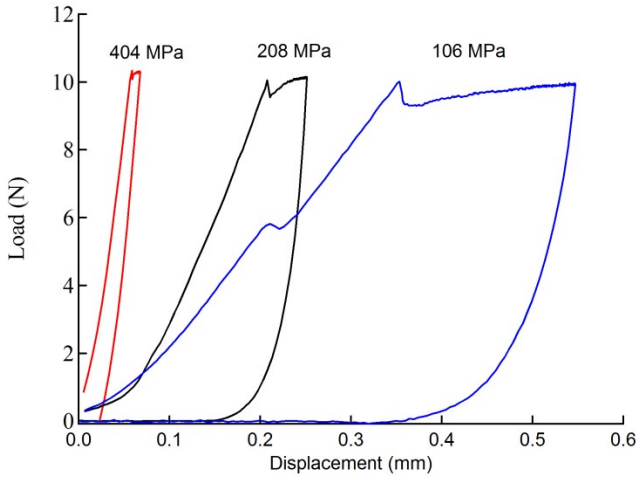

Figure 9: Representative load-displacement curves for oliver-pharr measurements for specimens within the top 10% (404 MPa), top 25% (208 MPa) and bottom 50% (106 MPa) of all test data.

For all samples, there was a slight drop in force due to overshoot as the machine reached 10 N, which was adjusted for during the 30-second hold using the machine's built-in PID controller. Overall, samples with a higher modulus experienced less creep deformation during the 10 N hold compared to samples with a lower modulus. The maximum indentation depth at load 10 N ranged from 0.01-1.2 mm, with the mean value 0.07 ± 0.11 mm, and the median 0.04 mm. The apparent modulus ranged from 50-761 MPa, having a right-skewed distribution with a mean of 194.7 ± 95 MPa and median of 171.4 MPa. For the samples tested, 50% were < 171 MPa and

90% were < 324 MPa (**Table 1**). The following factors significantly ($p \leq 0.002$) decreased modulus: osteoporotic or osteopenic status of the vertebrae, and female sex (**Table 2**). Bone status had the strongest correlation to apparent modulus, with the mean modulus being 244.9, 198.3, and 145.5 MPa for normal, osteopenic, and osteoporotic bone, respectively.

Table 1: Distribution of mechanical characteristics of the tested sites.

Distribution Statistics	Stiffness (N/mm)	Oliver-Pharr modulus (MPa)	Brinell hardness (BH)	Max Tolerable Pressure (MPa)
10th Percentile	113.6-333.7	324.4-760.6	1.75-3.99	14.0-31.7
15th percentile	72.4-113.5	237.3-324.3	1.19-1.74	9.8-13.9
25th percentile	48.6-72.3	171.4-237.2	0.82-1.18	6.7-9.7
Median	48.6	171.4	0.82	6.7
Mean	61.8	194.7	0.98	7.9
Standard deviation	44.6	95.0	0.63	4.9
Standard error of the mean	2.1	4.5	0.03	0.2
95% Confidence limits:				
lower	57.6	185.9	0.91	7.4
upper	65.9	203.6	1.03	8.3

Table 2: Summary of oliver-pharr measurements for all sites tested. A, B, C levels not connected by the same letter are significantly different (p>0.05) by the Tukey-Kramer multiple comparisons test. *P-value by F-test; **P-value by Wilcoxon test.

Modifying Factors	Tested Sites (#)	Mean Oliver-Pharr Modulus (MPa)	Standard Deviation	Standard Error of the Mean	95% Confidence Limits		P-value
					Min.	Max.	
Bone status:							
Normal	66	244.9 [A]	108.5	11.1	223	266.8	
Osteopenia	293	198.3 [B]	96.4	5.3	187.9	208.7	
Osteoporosis	88	145.5 [C]	42.9	9.6	126.6	164.5	<0.001*
Endplate defects:							
No	400	197.9	90.7	4.7	188.6	207.2	
Yes	47	168.2	123.4	13.8	141.1	195.3	<0.001**
Endplate:							
Cranial	221	195.7	90.7	6.1	183.7	207.8	
Caudal	226	193.8	99.1	6.6	180.8	206.8	0.685**
Endplate sites:							
Anterior	123	198.7 [A]	100.9	9.3	180.3	216.9	
Medial	202	196.9 [A]	99.4	7	183.1	210.8	
Posterior	122	189.5 [A]	82.5	7.5	174.6	204.4	0.723*
Sex:							
Female	220	180.1	84.1	5.7	168.9	191.4	
Male	227	208.9	102.6	6.8	195.5	202.3	0.002**

Stiffness

Representative curves used to calculate stiffness measured from testing are shown in **Figure 10**. These curves are also compared to *PEEK* and cortical bone tested in the same manner,

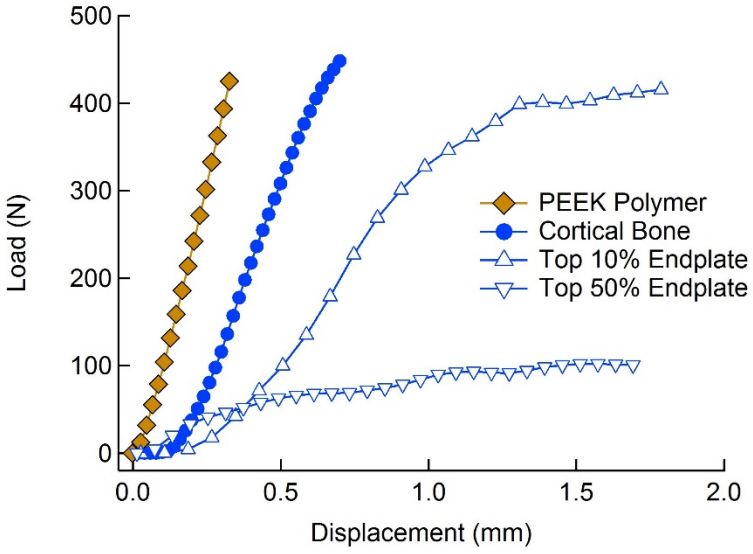

Figure 10: Representative stiffness curves for common spinal cage materials and vertebral endplates. The two bottom curves are representative of the top 10% of tested endplates and top 50% of endplates respectively. PEEK and cortical bone are shown to be stiffer than even the stiffest endplates

materials commonly used to create spinal fusion cages. It can be seen that both *PEEK* and

cortical bone show noticeably higher stiffness than the strongest tested endplates. The endplate stiffness measurements had a right-skewed distribution ranging from 2.5-333.7 N/mm. The mean value was 61.8 ± 44.6 N/mm, and the median was 48.6 N/mm. Fifty percent of tested sites had stiffness < 48.6 N/mm, and 90% < 113.6 N/mm (**Table 1**). The following factors were significantly ($p \leq 0.004$) linked with decreased stiffness: osteoporosis or osteopenia; the presence of endplate defects; cranial/caudal vertebral surface; anterior or medial locations across endplate; and sex (**Table 3**). The most influential factor in stiffness was again the bone status resulting in 115.7, 56.9 and 37.7 N/mm for normal, osteopenic, and osteoporotic bone, respectively.

Table 3: Summary of stiffness measurements for sites tested. A, B, C levels not connected by the same letter are significantly different (p>0.05) by the Tukey-Kramer multiple comparisons test. *P-value by F-test; **P-value by Wilcoxon test.

Modifying Factors	Tested sites (N)	Mean Stiffness (N/mm)	Standard Deviation	Standard Error of the Mean	95% Confidence limits		P-value
					Min.	Max.	
Bone status:							
Normal	66	115.7 [A]	70.6	4.7	106.5	124.9	
Osteopenia	293	56.9 [B]	32	2.2	52.5	61.2	
Osteoporosis	88	37.7 [C]	37.7	13.4	29.8	45.7	<0.001 *
Endplate defects:							
No	400	63.7	45	2.2	59.4	68.1	
Yes	47	45	37.6	6.5	32.3	57.7	<0.001**
Endplate:							
Cranial	221	56.9	39.8	2.7	51.7	62.2	
Caudal	226	66.6	48.6	3.2	60.2	72.9	0.004**
Endplate sites:							
Anterior	123	58.8 [B]	49.7	4.5	49.8	67.8	
Medial	202	56.6 [B]	38	2.7	50.8	61.4	
Posterior	122	75.8 [A]	47.4	4.3	67.3	84.5	<0.001 *
Sex:							
Female	220	49	22.8	1.5	45.9	52	
Male	227	74.2	55.8	3.7	66.9	81.5	<0.001**

Brinell Hardness

The Brinell hardness distribution was right-skewed ranging from 0.07-3.99, the mean was 0.98 ± 0.63, and the median was 0.82; 50% of measures were <0.82 and 90% were <1.75 (**Table 1**). The following factors were significantly ($p \leq 0.043$) linked with decreased hardness:

osteoporosis or osteopenic bone status; endplate defects; cranial/caudal vertebral surface; anterior or medial locations across the endplate; and female sex (**Table 4**). The largest contributing factor to the variation of Brinell hardness was again bone status, with hardness values of 1.77, 0.93, and 0.53 for normal, osteopenic, and osteoporotic bone, respectively.

Table 4: Summary of Brinell Hardness measurements for sites tested. A, B, C levels not connected by the same letter are significantly different (p>0.05) by the Tukey-Kramer multiple comparisons test. *P-value by F-test; **P-value by Wilcoxon test.

Modifying Factors	Tested sites (N)	Mean Brinell Hardness (BH)	Standard Deviation	Standard Error of the Mean	95% Confidence limits		P-value
					Min.	Max.	
Bone status:							
Normal	66	1.77 ^{A}	0.91	0.06	1.55	1.99	
Osteopenia	293	0.93 ^{B}	0.47	0.03	0.87	0.98	
Osteoporosis	88	0.53 ^{C}	0.19	0.02	0.49	0.58	<0.001 *
Endplate defects:							
No	400	0.99	0.63	0.03	0.93	1.05	
Yes	47	0.85	0.64	0.09	0.66	1.04	0.014**
Endplate:							
Cranial	221	0.9	0.53	0.04	0.83	0.97	
Caudal	226	1.04	0.71	0.05	0.96	1.14	0.043**
Endplate sites:							
Anterior	123	0.96 ^{B}	0.71	0.06	0.84	1.09	
Medial	202	0.91 ^{BA}	0.57	0.04	0.84	0.99	
Posterior	122	1.11 ^{A}	0.66	0.06	60.99	1.22	0.027 *
Sex:							
Female	220	0.83	0.33	0.02	0.74	0.91	
Male	227	1.11	0.8	0.05	1.04	1.12	0.018**

Maximum Load and Maximum Tolerable Pressure

The maximum load showed a right-skewed distribution ranging from 6.7-442 N with mean value = 73.5 ± 61.6 N and median value = 54.1 N. The probe displacement at the maximal load (depth at which resistance was maximal) ranged from 0.4-1.8 mm with a mean value of 1.1 ± 0.4 mm. The maximum tolerable pressure ranged from 0.6-31.7 N/mm^2, having a right-skewed distribution with a mean value of 7.9 ± 4.9 N/mm^2 and a median of 6.7 N/mm^2. 50% of values were found to be <6.7 N/mm^2 (**Table 1**).

Correlation Between Studied Characteristics

Statistically significant correlations existed between the measured mechanical properties (**Table 5**). The strongest correlations were found between MTP and Brinell Hardness (r^2=0.98). All studied mechanical characteristics had statistically significant ($p < 0.001$) correlations with radiographic (endplate thickness, endplate density, underlying cancellous bone apparent density, and bone mineral density) and demographic (age, and weight) indices (**Table 6**).

Table 5: Spearman's correlation between the studied mechanical characteristics.

Indices of distribution	Stiffness (N/mm)	Oliver-Pharr modulus (MPa)	Brinell hardness (BH)	Maximum Tolerable Pressure (MPa)
Stiffness (M/mm)	1.0	0.47	0.81	0.78
Oliver-Pharr modulus (MPa)		1.0	0.67	0.69
Brinell hardness (BH)			1.0	0.98

No statistically significant correlations were found with patient height for any of the mechanical properties. It was found that the strongest predictor for endplate stiffness was endplate thickness, with a correlation coefficient of 0.71. For Brinell hardness, the strongest predictor was found to be endplate density (ρ=0.64). Apparent Oliver-Pharr modulus only showed weak correlations with all of the radiographic and demographic indices. Additionally, it was found that the volumetric underlying cancellous bone mineral density provided a stronger correlation to the properties than areal bone mineral density from *DEXA*, both for stiffness and Brinell hardness.

Table 6: Spearman's correlation coefficient between the measured mechanical characteristics and radiographic and demographic indices.

Radiographic & demographic indices	Stiffness (N/mm)		Oliver-Pharr modulus (MPa)		Brinell hardness (BH)	
	ρ	P-value	ρ	P-value	ρ	P-value
Endplate thickness (mm)	0.71	<0.001	0.28	<0.001	0.59	<0.001
Endplate density (mg/mm^3)	0.67	<0.001	0.33	<0.001	0.64	<0.001
Underlying cancellous bone density (mg/mm^3)	0.49	<0.001	0.24	<0.001	0.46	<0.001
Bone mineral density (g/cm^2)	0.38	<0.001	0.30	<0.001	0.45	<0.001
Age (yr.)	0.26	<0.001	0.23	<0.001	0.44	<0.001
Weight (kg)	0.31	<0.001	0.38	<0.001	0.50	<0.001
Height (cm)	0.01	0.740	0.13	0.101	0.06	0.141

Modeling Mechanical Characteristics Using Radiographic and Demographic Measures

Correspondence between the experimental and modeled values of stiffness was strong, (**Figure 11**) with a correlation, r=0.85; coefficient of determination, $r^2 = 0.72$; and RMSE of 17.5 N/mm; $p < 0.001$. Using the model as a method to diagnose sites with stiffness <125 N/mm had the following predictive values: sensitivity, 97%; specificity, 91%; positive predictive value,

99%; negative predictive value, 70% (**Table 7**). Analysis of discrepancies over two RMSE (±35

Table 7: Sensitivity, specificity, positive and negative predictive value of each model as a diagnostic tool.

Developed model	Cut-off	Association of modeling with indentation test		Sensitivity	Specificity	Positive predictive value	Negative predictive value
		OR	P_{χ^2}	(%)	(%)	(%)	(%)
Stiffness (N/mm)	<125	303.2	<0.001	97	91	99	70
Oliver-Pharr modulus (MPa)	<200	5.7	<0.001	77	63	76	64
Brinell Hardness (BH)	<1.5	37.1	<0.001	95	65	94	69

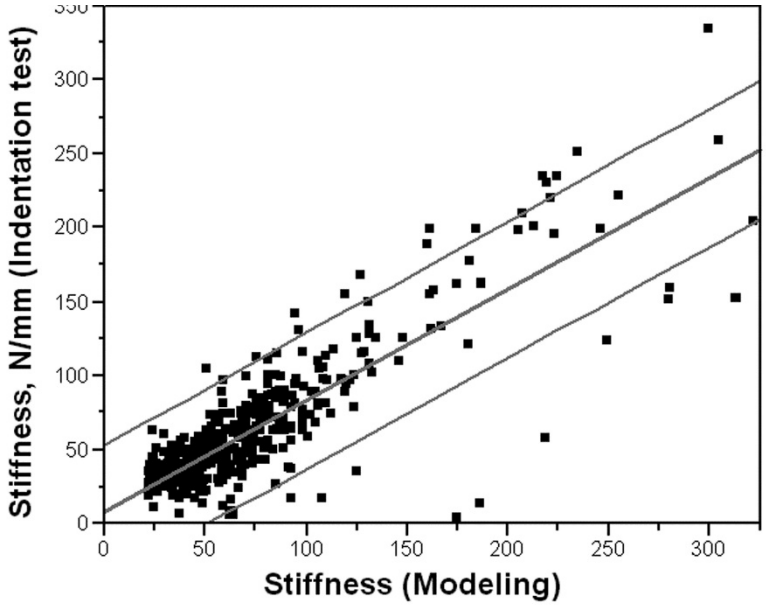

Figure 11:Correspondance between the predictive stiffness model and stiffness measured from indentation. Stiffness was modeled as a function of endplate thickness, endplate density, adjacent cancellous bone density, the presence of endplate defects, and patient age. The model showed a correlation of r^2=0.72 with the measured indentation stiffness.

N/mm) showed that 25 of 26 cases overestimated the stiffness when an endplate with relatively high average thickness and density had lacunarities, visible as black spots in enhanced contrast images, explaining the decreased negative predictive value of the model.[32]

A correlation between modeled and experimentally measured Brinell hardness is shown in **Figure 12**. Brinell hardness was predicted using endplate thickness and density, existence of endplate defects, and patient weight, which showed the strongest correlations with the

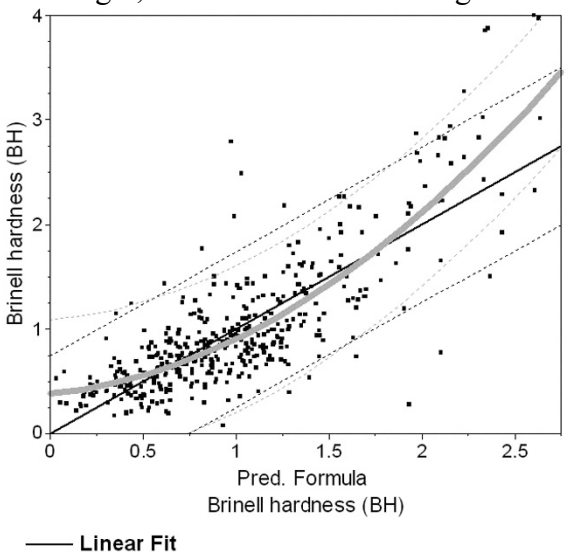

Figure 12: Correspondence between predicted hardness and hardness measured from indentation. Brinell hardness was modeled as a linear and polynomial model using endplate density, endplate thickness, presence of and endplate defect, and patient weight. The linear fit used the equation $y_{BH}=-2.9+0.002X_1+0.0011X_2+0.008X_4$ where y_{BH} is the linear approximation of Brinell Hardness, X_1 is the endplate mineral density (mg/mm^3), X_2 is the endplate thickness (μm), X_3 is the presence of an endplate defect or herniation (yes/no=±0.1), and X_4 is patient weight (kg). The polynomial fit was described by the equation $Y_{BH}=0.06 + 0.85\ y_{BH} + 0.36(y_{BH}-0.98)^2$ where Y_{BH} is the polynomial approximation of Brinell Hardness, and y_{BH} is the linear approximation obtained from the first equation. The linear fit showed a correlation of $R^2=0.64$ while the polynomial fit showed a correlation of 0.68 with the measured hardness values.

mechanical property (**Tables: 4,6**). Multiple linear approximation showed significant correspondence to the experimental data with correlation r = 0.80; coefficient of determination r^2 = 0.64; RMSE, 0.38 BH; $p < 0.001$ (**Figure 12**). However, analysis revealed a nonlinearity which was well described by a polynomial equation providing a better fit to the experimental data: r=0.82; r^2=0.68; and RMSE, 0.36 BH ($p < 0.001$) (**Figure 12**). Using the polynomial model to diagnose sites with Brinell hardness with a cutoff of < 1.5 had sensitivity, 95%; specificity, 65%; positive predictive value, 94%; negative predictive value, 69% (**Table 7**). Analysis of

discrepancies that exceeded 2 RMSE (±0.72 BH) showed significant (p=0.04) predominance of overestimation (17 of 22), corresponding with lower specificity and negative predictive value.

Apparent modulus was modeled using patient weight, existence of endplate defect, and endplate density using multiple linear regression modeling. A correlation of 0.44; coefficient of determination, r^2 =0.19; and RMSE, 85.3 MPa ($p < 0.001$; **Figure 13**) were found for the correspondence between the experimental and modeled values. Using the model to diagnose sites with modulus < 200 MPa as positive, the diagnostic capability for apparent modulus had sensitivity, 77%; specificity, 63%; positive predictive value, 76%; and negative predictive value, 64% (**Table 7**). Analysis of discrepancies that exceeded 2 RMSE (±171 MPa) showed predominance of underestimation (16 of 19 cases, p=0.02). Bland-Altman analysis of modeling

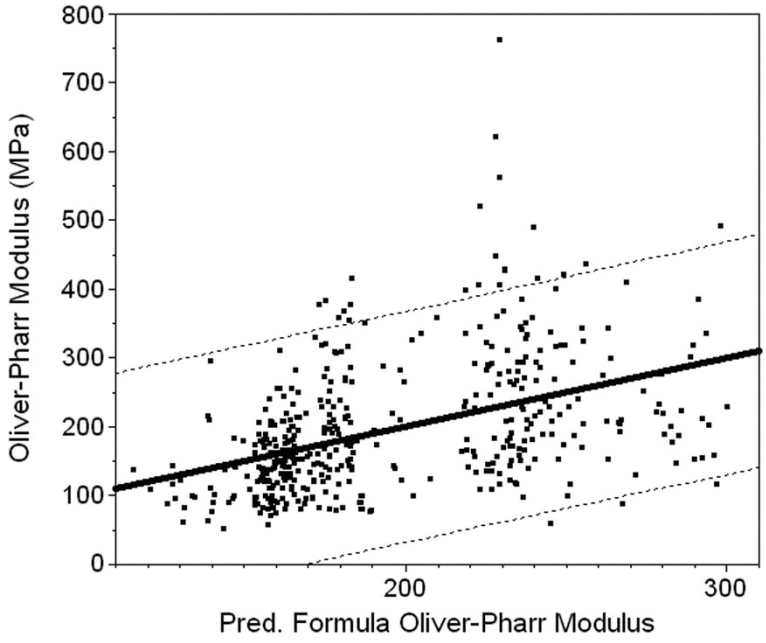

Figure 13: Correspondence between predicted apparent modulus and apparent modulus measured from indentation. Apparent Oliver-Pharr Modulus was modeled using endplate density, presence of endplate defects, and patient weight. Modulus was modeled using the equation $E= -71.35 + 1.57X_1 + X_2 \_ 0.092X_3$ where E is the linear approximation Oliver-Pharr modulus (MPa); X_1 is the patient weight (kg); X2 is the presence of an endplate defect or herniation parameter (yes/no=±19.3), and X_3 is the endplate mineral density (mg/mm3). The linear model showed a correlation of R^2=0.19.

for all 3 properties is shown in **Figure 14**. Hardness and stiffness models showed good correspondence with no significant bias; however, the modulus model showed a consistent negative bias for higher measured modulus, indicating that the model tends to under-predict modulus. Additionally, the two distinct bands in the analysis were found to be due to subject

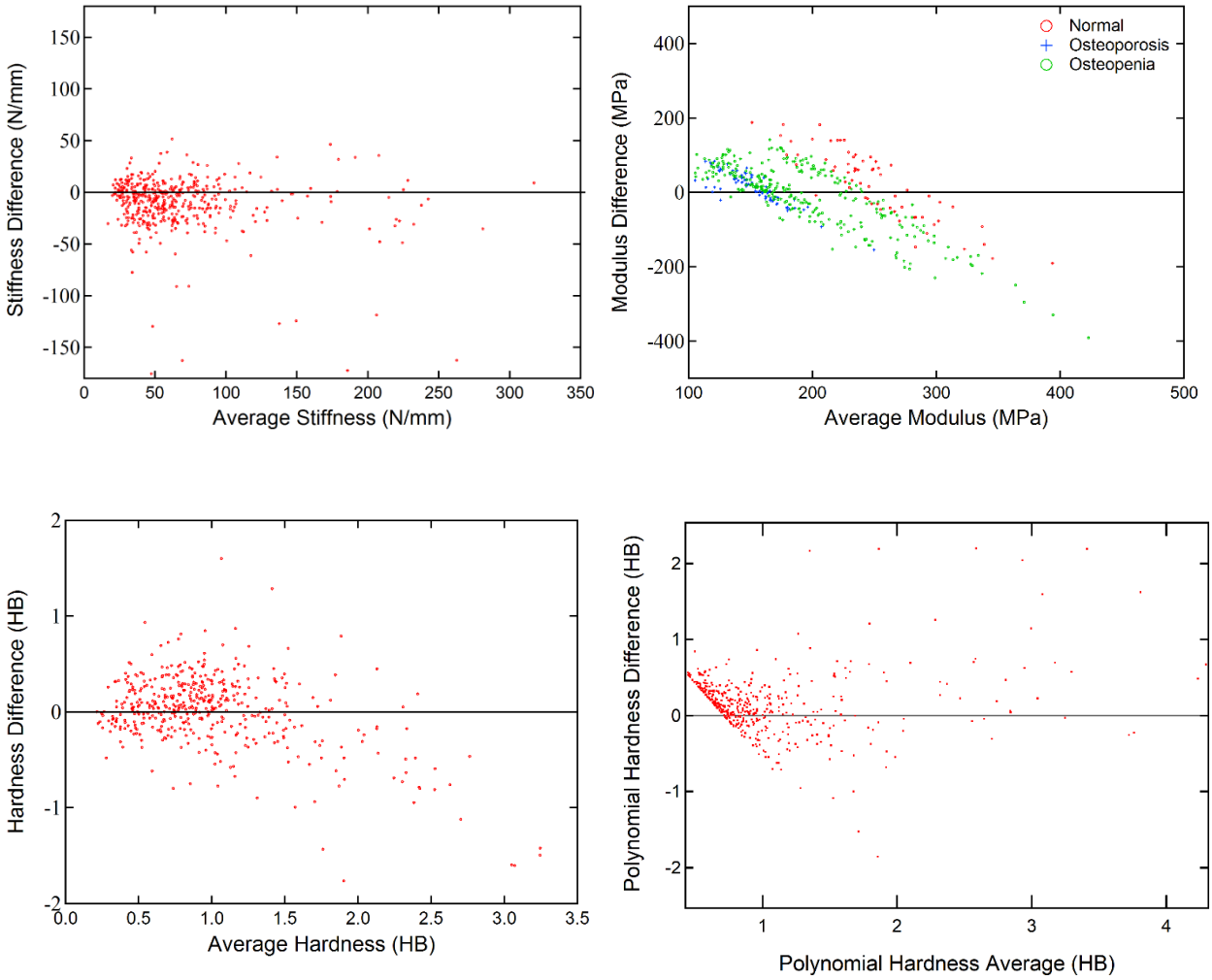

Figure 14: Bland-Altman analysis of each model. the Y-axis of each graph shows the difference between the modelled and measured mechanical property and the x-axis shows the average of the two methods. Points should be randomly distributed vertically across the full range of values measured. Stiffness (top left) shows a well fitted model as points are distributed randomly above and below the 0 line. Modulus (top right) shows a model requiring additional information to fit the data well. Both hardness MODELS (bottom) demonstrate a well fitted model. The polynomial model shows a slight artifact at low hardness values, but the rest of the model fits the measured values well.

selection rather than a statistical artifact. The bands are shown in Figure X with markers indicating bone status was a cause of the artifact seen in the analysis.

Discussion

The purpose of this study was to develop a predictive model for endplate mechanical properties at a scale relevant to implant design and behavior using radiographic and demographic patient data. Stiffness, apparent Oliver-Pharr modulus, MTP, and Brinell Hardness were evaluated across normal, osteopenic, and osteoporotic endplates (10 L1 and 10 L2 vertebrae) and demonstrated a wide range of properties, with the standard deviations of each property being between 49% and 72% of the mean values. It is important to note that this is the first study to look at mechanical properties to help separate elastic, plastic, and time-dependent effects during loading by using this set of properties. The resulting "apparent" or "effective" mechanical properties provide a measure of structural behavior of the endplate on a length scale relevant to bone-implant interactions. In particular, these properties can be used to guide the design of interbody fusion cages that aim to minimize the mismatch in material behavior between the implant and adjacent bone. As stated previously, current implants rely on solid materials designed to avoid fracture under physiological loading. However, in this study, we found that even the strongest endplates had stiffness values far below those of commonly used implant materials. The Oliver-Pharr modulus was introduced as a method to capture an elastic measurement of the composite structure of the endplate in order to directly compare it to the moduli of common materials. Though this study focused on many different properties of the endplate, in all cases, it was found that current implants materials have mechanical properties orders of magnitude higher than those of native endplate bone. The authors believe that this study demonstrates that a drastic shift is needed in the discussion of material properties with regards to implant design. The endplates measured in this study showed apparent moduli

significantly lower than those measured in previous research as it evaluated modulus at a scale which includes the structural effects of endplate defects and underlying bone density. Current implants not only are significantly stiffer than the surrounding bone but also have teeth and other protrusions which can cause stress concentrations. These concentrations combined with the low apparent modulus of the endplate are cause for concern and future designs should account for this during development. Further, previous studies demonstrate have shown the use of softer materials such as poly-L-lactic acid in lumbar cages reduces subsidence under axial loading as well as in vivo. This study aimed to quantify the properties of the endplate as well as develop a method for their prediction which demonstrated the reasoning and mechanism leading to subsidence in these studies.

In this study, results concerning mean values and distributions of maximal load, MTP, and stiffness corresponded with previously published data suggesting significant repeatability and high likelihood that the same results can be obtained in different populations with identical anthropometric characteristics.[31,32] For example, the model correlation to indentation tests for stiffness in this study (r=.85, n=447) and the previous study by Noshchenko *et al*. (r=.87, n=1056) were not significantly different (p=.173). Furthermore, the current study defines standardized mechanical indices attributed specifically to elastic and plastic properties and elucidates confounders that contribute to their high variability. In particular, it was found that apparent modulus varied significantly between osteoporotic, osteopenic, and normal bone, with a two-fold difference between the osteoporotic and normal bone in terms of elastic response. This is indicative that poor bone density (i.e., low bone mineral density and increased bone porosity) will significantly decrease the modulus of the vertebral endplate. This result is in agreement with previous studies which found that subsidence correlates significantly with osteoporotic

status.[40,41] However, in this study, the osteoporotic status of the bone was used as a direct predictor of mechanical properties rather than a general quantification of risk of subsidence, allowing for additional comparison to implant material properties. Additionally, several studies have shown subsidence to occur as a time-dependent injury rather than acutely, occurring between 0.25 and 8 months after surgery.[42] This may occur due to a combination of factors, including mechanical creep, resorption of underlying bone tissue by osteoclasts, and/or local failure of the endplate. The mechanical characteristics modeled via *CT* imaging can be used as indices of the time dependent response of bone to loading during fusion reflecting risk of subsidence or other complications such as vertebral fracture or correction loss. It can be confirmed by the creep response shown in **Figure 9** that decreased modulus allows for more rapid creep. In the case of the osteoporotic bone shown on the far right with lowest apparent modulus (106 MPa), the indenter crept significantly more than that of the normal bone over 30 seconds. It was found that after 30 seconds of holding, the creep rate was constant, and did not increase. No other properties measured in this study captured the time-dependent characteristics of the vertebral endplate.

Stiffness in this study, unlike modulus, measured both the plastic and elastic response of bone to loading as the indentation stresses the endplate beyond fracture. Therefore, it can provide an index to predict subsidence caused by permanent bone deformation. Previous studies have shown that the endplate contributes significantly to the indentation stiffness of the vertebra; however, the underlying cancellous bone contributes approximately 20% of the stiffness, indicating that stiffness is still dependent on the underlying bone density and structure, unlike modulus. As such, it may provide a more accurate predictor of subsidence.

The studied endplate mechanical indices had significant correlations with different characteristics such as: 1) radiographic (endplate thickness, endplate density, underlying cancellous bone density, bone mineral density); 2) demographic (age and sex); and 3) physiologic (weight). Interestingly, the mechanical characteristics are proportional to the patient's weight, the endplate thickness, and densitometric indices of the vertebra corresponding to Wolff's law, which states that greater physiological demands on the bone will produce a more robust structure due to bone adaptation.[43] Multiple regression analysis confirmed previous findings that mechanical properties of the lumbar vertebral endplates can be approximated by combinations of radiographic indices obtained by conventional *CT*, despite low resolution as well as variable demographic (age) or physiologic (weight) indices.[32] In particular, stiffness and Brinell hardness can be approximated most accurately (**Figures 11, 12**) with some tendency to overestimate. Apparent modulus can be defined less precisely (**Figure 13**) with a tendency to underestimate because the relatively low resolution of the conventional *CT* does not allow accurate assessment of density and roughness at the endplate surface. As sub-voxel level measurements were not possible using our methodology, the endplate bone density and lacunarities could not be captured at the endplate surface where the modulus measurement is performed, leading to the decreased accuracy of the modulus model. Of note, the diagnostic value of these approximations is relatively high for diagnosis of the softest sites across endplates with low stiffness (<125 N/mm), low hardness (<1.5 BH), and low apparent modulus (<200 MPa), (**Table 7**) allowing for the use of these predictive models as a diagnostic tool to predict relatively weak bone. Additionally, it was found that volumetric endplate density was a stronger predictor of mechanical performance than areal bone mineral density for all measured properties.

This phenomenon has been described in previous studies, as the volumetric density accounts for 3-dimensional structure rather than the 2-dimensional measurement of areal *BMD*.[44]

Results of the current study are in agreement with previous findings that the mechanical properties of lumbar vertebrae endplate show a right-skewed distribution, [31,32] with a predominance of relatively weak sites with low *MTP*, low apparent modulus, and Brinell Hardness comparable with the hardness of soft wood (1.6 BH). The average mechanical characteristics of vertebral endplates are significantly lower than that of the most commonly used interbody implant materials such as titanium or titanium alloys, cortical bone allografts (femoral or tibial rings), and *PEEK* (**Table 8**). In the case of apparent modulus, the endplate showed a measured modulus at least 10 times lower than the various materials on average. It is possible that using materials tailored to the distribution of material properties across the endplate would decrease the risk of subsidence; however, further research is needed to fully understand the effects of using such a material. Theoretically, the large differences seen in mechanical properties between the endplate and current implant materials suggest high risk of endplate damage resulting from interaction with such implant types.[4] Results of this study suggest that the demonstrated approach could be used in clinical practice as an *in vivo* diagnostic procedure for patient-specific selection of implant and surgical planning. Additionally, this study found that osteoporotic patients are significantly more susceptible to creep-induced subsidence, indicating additional planning is required when performing fusion in such cases. Finally, the high stiffness of current surgical materials compared to vertebral bone requires further research into more compliant materials for implantation in spinal fusion to better distribute load across the endplate and reduce stress concentrations. Other methods of reducing excessive endplate loading could

include the use of posterior fixation (e.g. pedicle screws and rods) to transfer additional load to the posterior spine rather than the endplate or augmentation of the vertebra using bone cement.

Table 8: Mechanical characteristics of materials used for intervertebral implant manufacturing.

Mechanical characteristic	Material	Source of data	Details of material sample	Indices
Stiffness/(N/mm)	CPTi/Ti alloys	Literature[32,45]	Interbody cage	3200
			Surgical rods	1900-2700
	PEEK	Current study	Interbody cage	509-819
			Raw material	1365-1368
	Cortical bone	Literature[32]	Allograft ring	500-1600
		Current study	Allograft ring	611-1674
Brinell Hardness (HB)	CPTi/Ti alloys	Literature[46]	NS	223-653
	PEEK	Literature	NS	NS
		Current study	Interbody cage	10-12
			Raw material	21
	Cortical bone	Current study	Allograft ring	8-25
Oliver-Pharr modulus (GPa)	Ti/Ti alloys	Literature[47]	Cylindrical specimens	80-140
	PEEK	Literature[48]	Specimens for NIT	4-16
	Cortical bone	Literature[48,49]	Specimens for NIT	15-26

One limitation of this study was the relatively low resolution from *CT* imaging, preventing analysis of radiographic indices at the endplate surface at the scale of the Oliver-Pharr

indentation depth (≈0.15mm), limiting the accuracy of the apparent Oliver-Pharr modulus modeling. However, the image resolution used in this study is comparable to that available using *CT* imaging of patients. Therefore, the ability of *CT*-based indices to predict endplate stiffness shows promise for potential clinical applications. Further, the whole lumbar spines were imaged ex-situ, and thus are not surrounded by other muscle and organs which could affect image quality; however, using proper reconstruction filters should minimize this effect.

Conclusions

The mechanical properties of the lumbar vertebral endplates are variable across the surface, with a right-skewed distribution. These properties are also significantly decreased by osteoporosis and osteopenia when compared to normal bone.

1. The studied mechanical properties showed significant correlations with radiographic and demographic characteristics. Bone status (osteoporosis and osteopenia) showed the greatest effect on all properties, causing decreases between 30-50%.
2. Using a combination of radiographic and demographic indices allows for the prediction of vertebral endplate mechanical properties. Model correlations (r^2) were found to be 0.72, 0.68, and 0.19 for stiffness, hardness, and apparent modulus respectively.

CHAPTER III

BIOLOGICAL AND FINITE-ELEMENT MODELING OF POROUS POLY(PARA-PHENYLENE) FOR ORTHOPEDIC IMPLANTS

Introduction

As discussed in the previous chapter, over 500,000 lumbar interbody fusion (LIF) surgeries are conducted annually in the United States[50]. Current approaches to LIFs use devices made from traditionally solid materials to restore disc height and provide stability for fusion; however, these designs do not evenly distribute loads across the vertebral endplates and can lead to micro-fractures and subsidence, which compromise the effectiveness of the procedure and contribute to adjacent level disease [51-53]. Metallic materials have been used for their high strength and bioinert properties; however, signal artifact interference during imaging makes these materials less than optimal for tracking success of the procedure. Furthermore, the high modulus of the material can lead to a material property mismatch at the interface with the bone, resulting in uneven load distribution and potential bone resorption or subsidence [54]. Alternatively, polymeric materials can avoid radiographic noise signals and have material properties closer to bone. Ideally, a load-bearing orthopedic material would possess similar mechanical properties, such as elastic modulus and strength, to the adjacent native bone to help avoid stress concentrations and stress-shielding [55].

Porous implants have been introduced to better match the mechanical properties of bone, enhance osseointegration, and promote vascularization throughout orthopedic devices. Osseointegration itself is a complex and highly structured biological process. First, progenitor cells must be able to migrate and propagate into the porous materials and then subsequently differentiate and through endochondral or intramembranous processes form mineralized bone [56,57]. The newly formed bone is subsequently remodeled forming mechanically stable mature

bone [58,59]. During the early stages of this process, the interface between the bone and the device is occupied by a provisional environment (e.g., collagen fibrils and high micro-vasculature) that must be stabilized to allow the new bone to form [60]. Mismatched mechanical properties can induce excessive motion that can stimulate fibrosis at the interface and result in failure of the implant. Even though bulk porosity can promote interaction between the native bone and the material, it is challenging to maintain the structural integrity of the construct over the time course associated with healing. In addition, porous materials show increased wear rates or pore collapse at contact surfaces due to decreased contact area; this can lead to particle generation due to increased contact pressure [61]. Therefore, implants often have to satisfy two relatively opposing design criteria: increased porosity to improve osseointegration, while at the same time, sufficient mechanical strength to support physiologic loading. High strength polymeric materials may be suitable for porous applications while maintaining sufficient mechanical strength.

Poly(*para*-phenylene) (PPP) is an aromatic polymer which has higher strength and stiffness (σ_y=175 MPa, E=5.0 GPa) than polyetheretherketone (PEEK) (σ_y=118 MPa, E=2.2~4.2 GPa), the gold standard material for polymeric orthopedic implants [14,62]. PPP has exceptional mechanical strength and stiffness due to its repeating aromatic rings that provide strong anti-rotational biaryl bonds. Frick *et al*., investigated the degradation of PPP soaked in saline over a year and observed about 1wt.% increase, and mechanical properties did not show a statistical difference. To demonstrate nontoxicity of material, PPP soaked media treated to mouse fibroblast and observed no cell lysis and change of proliferation [14]. Furthermore, PPP has an amorphous structure making it relatively insensitive to molding fabrication technique and processes. By comparison, PEEK is more challenging to manufacture (particularly with thermal processing), partially because its mechanical properties are greatly influenced by processing

conditions and degree of crystallinity [63]. This ability to manufacture different architectures and use different processes while maintaining mechanical properties makes PPP a very promising potential orthopedic biomaterial.

To date, only a limited number of studies have investigated PPP as an orthopedic biomaterial [64-66]. The authors have previously investigated the mechanical behavior of PPP scaffolds with varying pore size and porosity. It was determined that a 70 vol% porosity with pore size of 420–500 μm closely resembled the modulus of natural trabecular bone [15]. Further, with the ability to vary porosity across a wide range, the mechanical properties of porous PPP can be tailored to match a wide variety of bone properties which can vary significantly due to age or pathology. Other studies have utilized finite element modeling of the L4-L5 motion segment in the spine and also suggested a 70 vol% porous PPP interbody spacer could be sufficiently compliant, reduce stress concentrations, and still withstand axial compressive loading in the spine [67]. While the mechanical properties of porous PPP scaffolds have been studied, the potential osteocompatibility and osseointegration of these scaffolds have not been demonstrated in a biological setting.

The purpose of this study was to investigate the performance of PPP scaffolds *in vitro* and *in vivo*, as well as to evaluate the biomechanical properties associated with bone integrating with the polymeric scaffolds using finite element analysis (FEA). In addition, we manufactured both solid and porous scaffolds from PPP and PPP and compared osseointegration. Four different scaffold groups were used in this study: 1) solid PPP, 2) solid PEEK, 3) porous PPP and 4) porous PEEK. Osteocompatibility was assessed by culturing pre-osteoblasts on disc-shaped wafers of each material and evaluating osteogenic differentiation. Osseointegration was assessed by implantation of cylindrical material scaffolds into circular defects in the rat tibia metaphysis.

We hypothesized that the 70 vol% porosity of PPP material would provide enhanced osseointegration through the entire construct. The mechanical response of porous implants with bone ingrowth was analyzed using a finite element push-out test. Implants with simulated bone ingrowth were subjected to a known displacement to measure reaction forces and stress dissipation within the implant to determine push-out force. Studying these structured materials may provide insight into the potential utility of PPP as an orthopedic biomaterial.

Materials and methods

Material Fabrication

Porous and solid implants were manufactured via compression molding using a uniaxial testing machine (Insight 30, MTS Systems, Eden Prairie, MN, USA). PPP and PEEK powder (Solvay PrimoSpire PR-250 and KetaSpire KT-820) were provided by Solvay Specialty Polymers (Alpharetta, GA, USA) and were mixed to a volume ratio of 30:70 polymer powder-to-salt for porous scaffolds using salt crystals sifted to between 420-500 μm as used in previous studies by the authors [16]. Solid implants were molded using pure polymer powder. PPP scaffolds were heated to 180°C for 20 minutes in a 2 mm x 18 mm mold and then compressed to a stress of 85 MPa for 20 minutes. PEEK scaffolds were heated to 370°C and compressed for the same time and stress. After compression, molds were removed from the oven and immediately quenched to ambient conditions in water (~22°C). Porous scaffolds were placed in rapidly stirred water baths for 24 hours at 60°C to ensure all salt was dissolved away. Scaffolds were then placed in a vacuum oven for 1 hour at 80°C to dry. All four surfaces were measured for average surface roughness, S_a, with a laser confocal microscope (LEXT OLS4000, Olympus, Center Valley, PA, USA) using a 20x objective, 100 nm step size, λ_c = 100 μm and 150 μm x 150 μm evaluation area (n=3, 3 spots per sample). Morphometric analysis of the scaffold pores

was conducted using the BoneJ plugin for ImageJ software (National Institutes of Health, USA). Specifically, strut thickness (μm), strut connectivity (connections/cm^3), structural model index, and anisotropy of the structure were quantified. Following material fabrication, the modulus of each porous scaffold type was measured using dynamic mechanical analysis and simulated using FEA. Each scaffold was potted in a custom fixture and cyclically strained 0.2% at 1 Hz to measure the elastic modulus. FE models were compressed by 2% of their overall length, and reaction forces were recorded to measure the apparent modulus of the material.

In Vivo Animal Surgery

All animal care and experimental procedures were approved by the Veterans Affairs Institutional Animal Care and Use Committee (IACUC) for the VA hospital in Atlanta, GA and carried out according to the guidelines. Thirteen-week-old male Sprague-Dawley rats (n=6/groups, Charles River Labs, Wilmington, MA, USA) were used in this study. After pre-operative preparation, animals were anesthetized by isoflurane inhalation (2~3%). The proximal tibia was exposed by a 1.5-2 cm longitudinal incision through the skin. The muscle tissue was then separated using blunt dissection along the muscle bundle divisions. One transcortical hole (2.5 mm diameter) was created at the proximal tibial metaphysis using a low speed rotational drill speed (~800 rpm) under cooling with sterile saline. One sterile cylindrical scaffold of each sample group was placed into the predrilled holes through both cortices. The muscle was then sutured closed with absorbable 4-0 sutures and skin and closed with wound clips. Buprenorphine SR (0.03 mg/kg; 1 ml/kg) was used as an analgesic and applied via subcutaneous injection.

Digital Radiographic Evaluation

Animals received serial x-ray imaging at 2, 4, 6 and 8-weeks post-surgery. *In vivo* X-ray scanning (In-Vivo Xtreme, Bruker Corp., Billerica, MA, USA) was performed on the tibial

region at an exposure time of 15 s and a voltage of 25 kV. To assess bone ingrowth throughout implant and osseointegration, micro-computed tomography (micro-CT) scans (Micro-CT40, Scanco Medical, Bruttisellen, Switzerland) were performed following euthanasia at 8 weeks (n=6/groups). Samples were scanned with a 20 μm voxel size at a voltage of 55 kVp and a current of 145 μA. The bone volume of interest was assigned by contouring the perimeter of each implant. Three dimensional reconstructions were obtained from evaluations of 500 slices of two-dimensional X-ray images. New bone formation was evaluated by application of a global threshold corresponding to 50% of the cortical bone density (386 mg hydroxyapatite/cm^3) [11].

Histological Analysis

After euthanasia at 8 weeks post-surgery, tibial explants were fixed with 10% neutral buffered formalin (10% NBF) for 3 days then stored in 70% ethanol until processing. Samples were dehydrated through ascending grades of alcohol and cleared in xylene. To observe mineralized bone structure, fixed bone samples were processed in plastic (methyl methacrylate; MMA) resin for a week. After embedding, plastic blocks were cut using a grinding system (EXAKT 400 CS, Exakt Technologies, Inc., Oklahoma City, OK, USA) to an average thickness of 25 μm. Sections were stained with methylene blue and acetic fuchsin or Goldner's Trichrome staining (n=1/each staining). Images were obtained with the Axio Observer Z1 microscope (Carl Zeiss, Jena, Germany) and captured using the Axio Vision software (Carl Zeiss Micro Imaging, Thornwood, NY, USA).

Finite Element (FE) Simulated Push-Out Test

Micro-CT scans of the implants were segmented using Simpleware ScanIP (Synopsys, Mountain View, CA, USA). Percent porosity was verified following segmentation by subtracting material volume from the total volume of the cylinder. A 2.6 mm length of each

implant was computationally modeled and embedded in a bone block to simulate a push-out test. Bone ingrowth was modeled as a layer of bone following the shape of the pores through the implant. Simulated ingrowth was modeled to match ingrowth percentages measured from the rat model scans. Material properties were assigned as shown in **Table 9**.

Table 9:Material Properties assigned to bone and scaffolds in simulated push-out test

	Yield Stress (MPa)	Elastic Modulus (MPa)	Poisson's Ratio
Bone	178	13,000	0.3
PEEK	118	4,100	0.3
PPP	175	5,000	0.3

The coefficient of friction between bone and implants was defined as 0.25 for all implant types [68,69]. To increase computational efficiency, it was assumed that the implant would show symmetry about its axes and a half implant was modeled in the case of the porous scaffolds. Symmetric boundary conditions were applied on the plane of symmetry for the implant, and reaction forces were doubled after measurement to determine the push-out for the full implant. Perfectly plastic behavior was assumed for all materials after yielding. The modulus of newly formed bone was estimated as 13 GPa based on mineral density measurements using the empirical relationship developed by Wagner *et al.*[70] The simulated push-out was performed using ABAQUS (3DS SIMULIA, Johnston, RI, USA). The bone block was pinned in all directions, and a displacement equivalent to 2% of the implant length was applied to the implant and ingrown bone at the top of the block. This loading level was chosen to exceed that of the ultimate strain of cortical bone. Reaction forces at the surface of the implant and bone were taken to measure load sharing and total push-out force. Average stress at 0, 20, 40, 60, 80, and 100% of the length of the implant was calculated to determine stress dissipation within the scaffold. A model of this method can be seen in **Figure 15**.

In addition to pushout testing, apparent modulus of porous implants was calculated as a function of porosity and bone ingrowth. 2.5 mm porous cube scaffolds between 50% and 85% porosity were segmented in the same manner as described previously and modelled with varying amounts of bone ingrowth from 0 to 100%. Bone ingrowth was defined as Ingrowth (%) = BV/PV where BV is the volume of ingrown bone and PV is the free volume of pores within the implant. Implants were pinned on the inferior portion of the cube and a displacement equal to

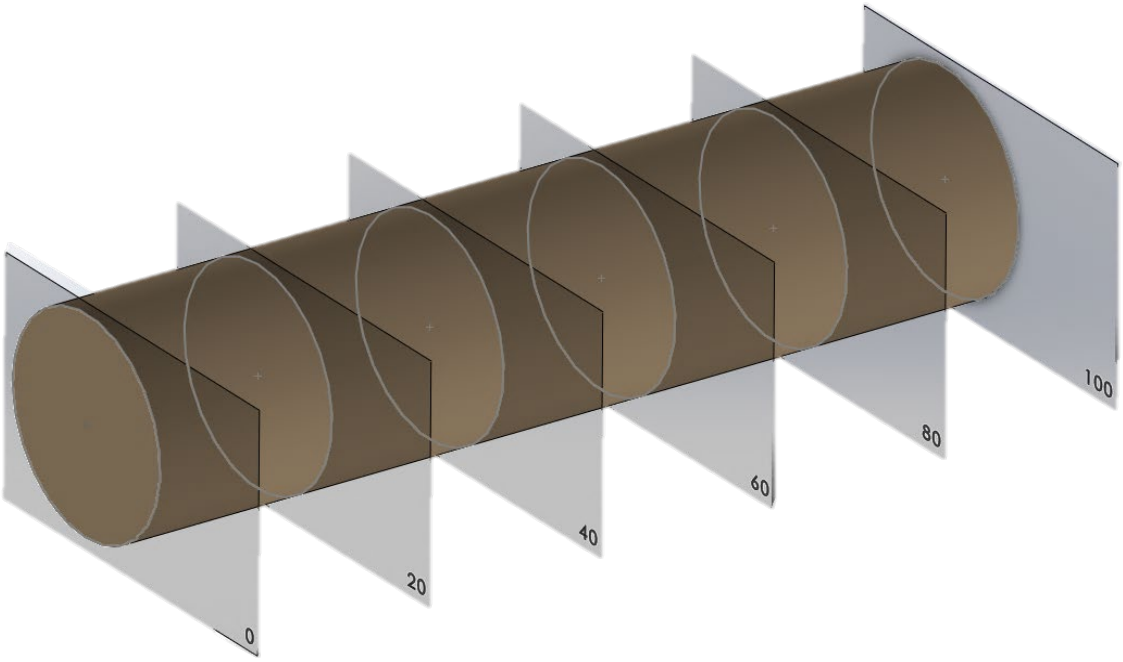

Figure 15: Depiction of equally spaced intervals for stress dissipation measurement.

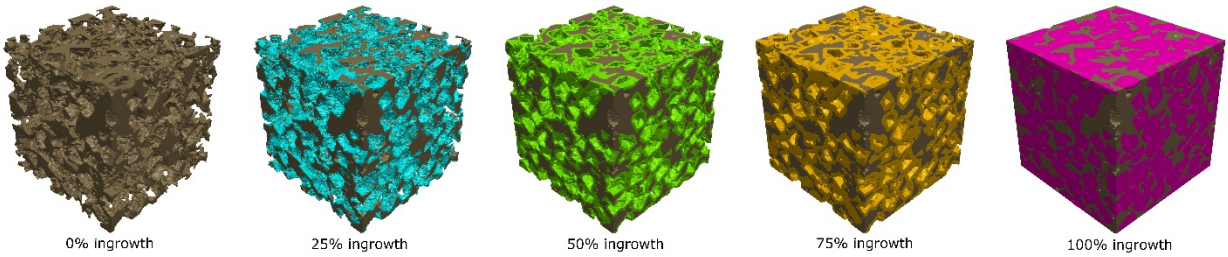

Figure 16: representative image of simulated ingrowth into a porous scaffold. Ingrowth was simulated from 0 to 100% infill layers contouring the inner surfaces of the pores.

2% of the implant height was applied at the superior portion of the cube. Apparent modulus and load sharing between the implant and bone were recorded for each porosity and bone ingrowth

level. Load sharing was defined as the percentage of total force being transmitted through the bone or implant. A representative depiction of the modelled bone ingrowth can be seen in **Figure 16** showing a 2.5 mm cube with ingrowth from 0% to 100%. Additionally, stress concentration factors for the various porosities without bone ingrowth were calculated based on the apparent stress applied at the top of the cube and the maximum stress within the cube before plastic deformation occurs. Calculation of the stress concentration factor will allow for evaluation of material stresses in porous implants while modelling them as a solid body, simplifying future analyses of porous implants. Additionally, it allows for the determination of implant fatigue life and evaluation of the long-term viability for implantation in load bearing applications.

Statistical Analysis

Statistical significance for quantitative results were assessed with one-way analysis of variance (ANOVA) with Tukey's multiple comparison post-hoc test. As appropriate (and specified in the results section), unpaired Student's two-tailed *t*-test were used for analysis. P-values less than 0.05 indicated statistical significance. Numeric values are presented as the mean ± S.E.M. All statistical analysis was performed using GraphPad Prism 5.0 software (GraphPad, La Jolla, CA, USA).

Results

Scaffold Fabrication

Four types of materials were fabricated for this study, including solid and 70 vol% porous scaffolds made from either PPP or PEEK. Representative images of these scaffolds are presented in **Figure 17**. The solid PPP samples are visually transparent and have a yellowish color, compared to solid PEEK samples that were opaque and brown. Both sets of PPP samples were

more uniform in color and appearance, although the porous PPP sample lost its transparency due to the presence of pores. PEEK samples had a variation in color, which is due to the difficulty of producing the samples as well as changes in the degree of crystallinity throughout the samples. Porosity of representative scaffolds was measured using 3D segmented micro-CT scans to be 68-71% (st. dev.= .021, n=3). In addition, micro-CT verified that all salt particles had been

Figure 17: Representative images of implants. Micro-CT (top), Cylindrical implants for insertion in rat tibia (middle), and disk-shaped cylinders for cell culture (bottom)

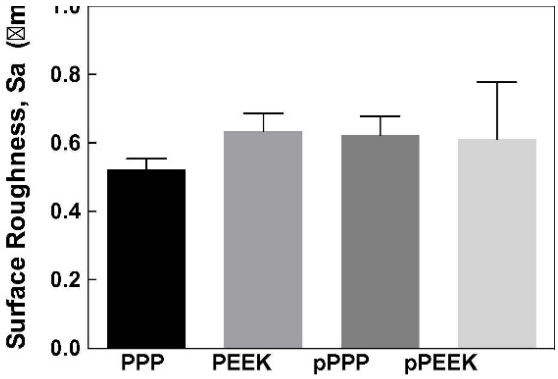

Figure 18: Surface roughness for each type of implant. No significant differences between each type was measured.

successfully leached out of the scaffold during manufacturing. Surface roughness (S_a) was measured for each sample and were not statistically different between groups (**Figure 18.** one-way ANOVA, Tukey, n=3; PPP: 0.5237 +/- 0.0304 µm, PEEK: 0.6349 +/- 0.0522 µm, pPPP:

0.6233 +/- 0.0544 µm, pPEEK: 0.6111 +/- 0.1679 µm). Data and microscopy regarding pore sizes using this method can be found in the previous studies by the authors [16]. Pore morphometry for porous PPP and PEEK scaffolds showed strut thickness values of 112.4 µm and 100 µm for PPP and PEEK, respectively. Additionally, strut connectivity densities for PPP and PEEK were measured to be 54780 and 78228 connections/cm^3, respectively. The structural model index calculation for the scaffold indicated the pores were primarily oblong with rounded edges with SMI values of 3.08 and 2.515 for PPP and PEEK, respectively, where 0 indicates a flat structure, 3 indicates a cylindrical shape, and 4 indicates a spherical pore. The scaffold structure was found to be primarily isotropic with PPP and PEEK scaffolds showing degrees of anisotropy of 0.13 and 0.20. Representative images of trabecular thickness and spacing measurements can be seen in **Figure 19**.

The apparent modulus of the porous scaffolds was measured using dynamic mechanical analysis (DMA), and was found to be 212 ± 2.8 MPa (n=2) for porous PEEK and 231 ± 19.8 MPa (n=2) for porous PPP. These results closely matched those of the simulated compression test of the materials, which showed moduli of 153 and 213 MPa for PEEK and PPP respectively. Data

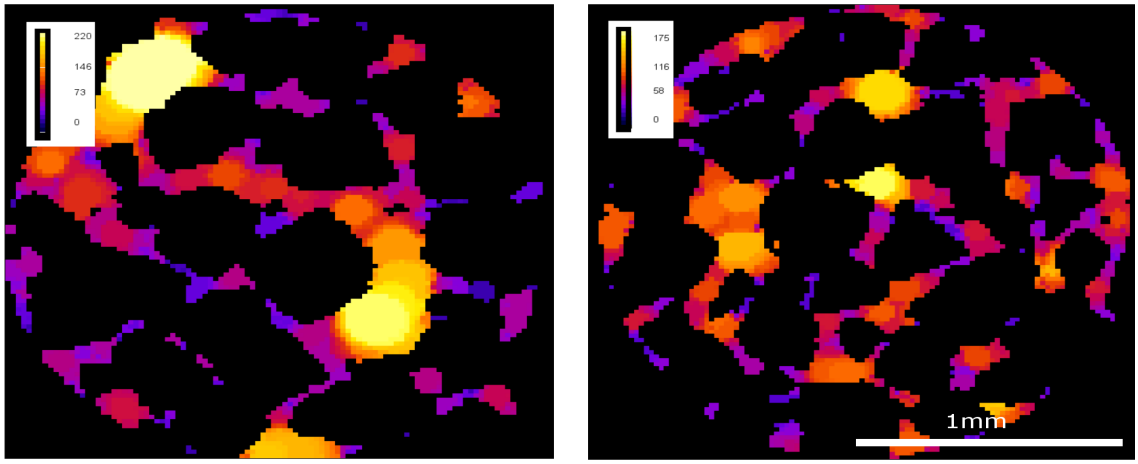

Figure 19: Trabecular thickness measurements for pPPP (left) and pPEEK (right). Areas shown in black are pores within the implant and colored areas depict a heatmap of trabecular thickness of the implants. Heatmap colorbar is given in units of µm

from this comparison allowed for validation of the finite element model used in the study as the direct measurement of the scaffold apparent modulus correlated well with the finite-element compression test of the scaffolds. Further, these moduli were compared to the Gibson-Ashby cellular solid model. The results measured from DMA and FEA were significantly lower than those predicted by the model.

Implant Osseointegration

To investigate material osseointegration, we implanted solid and porous cylindrical materials into defects in the rat tibia. X-ray radiographs were taken at 8-weeks post-surgery to visualize bone formation **(Figure 20A)**. For solid implants, an empty cylindrical region in the

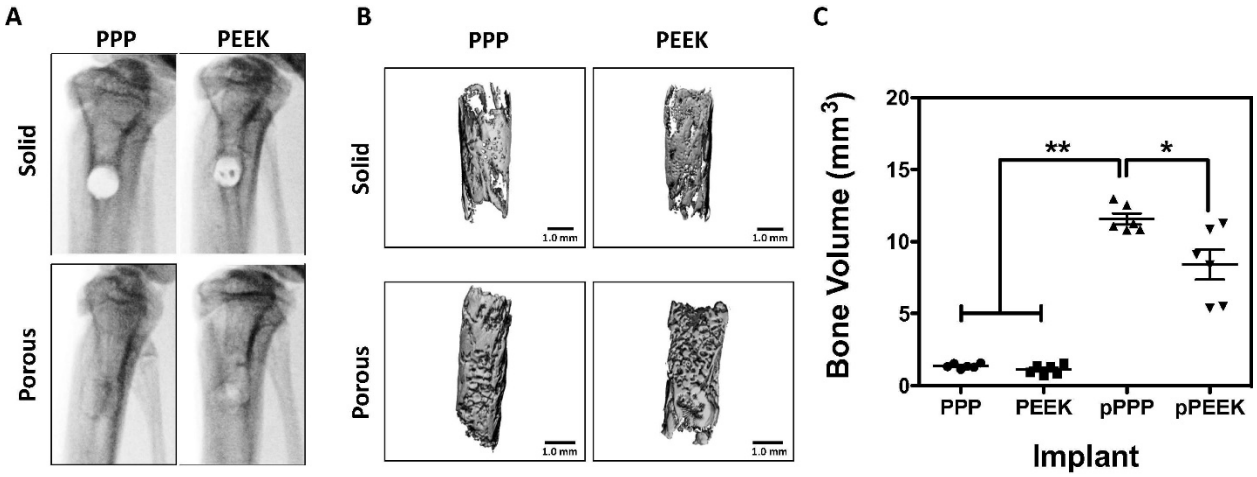

Figure 20: Bone ingrowth throughout porous materials, especially PPP showed significantly increased bone ingrowth. A) in vivo x-ray radiographs post-surgery. B) representative micro-CT reconstructions of the same specimens from x-ray images. C) quantitative measurement of mineralized bone volume of implants. Solid scaffolds showed no significant difference of BV between groups. Porous PPP explants showed significantly increased BV value compared to any other explants *$p<0.05$; **$p<0.0001$; n=6; data presented as mean ± SEM

tibial metaphysis that matched the surgically created defect was still identifiable by radiograph at the 8-week time point. Conversely, radiographs of rats with porous implants showed filling of the defect, suggestive of bone ingrowth and mineralization. To confirm the x-ray studies, tibiae were analyzed *ex vivo* using micro-CT, and bone formation was quantified **(Figure 20B)**. Solid

implants from both materials showed a thin layer of new bone formation along the material surface, while the porous materials showed mineralization not only on the surface, but also throughout the entire implant. The bone volume (BV) was measured within the pores of the

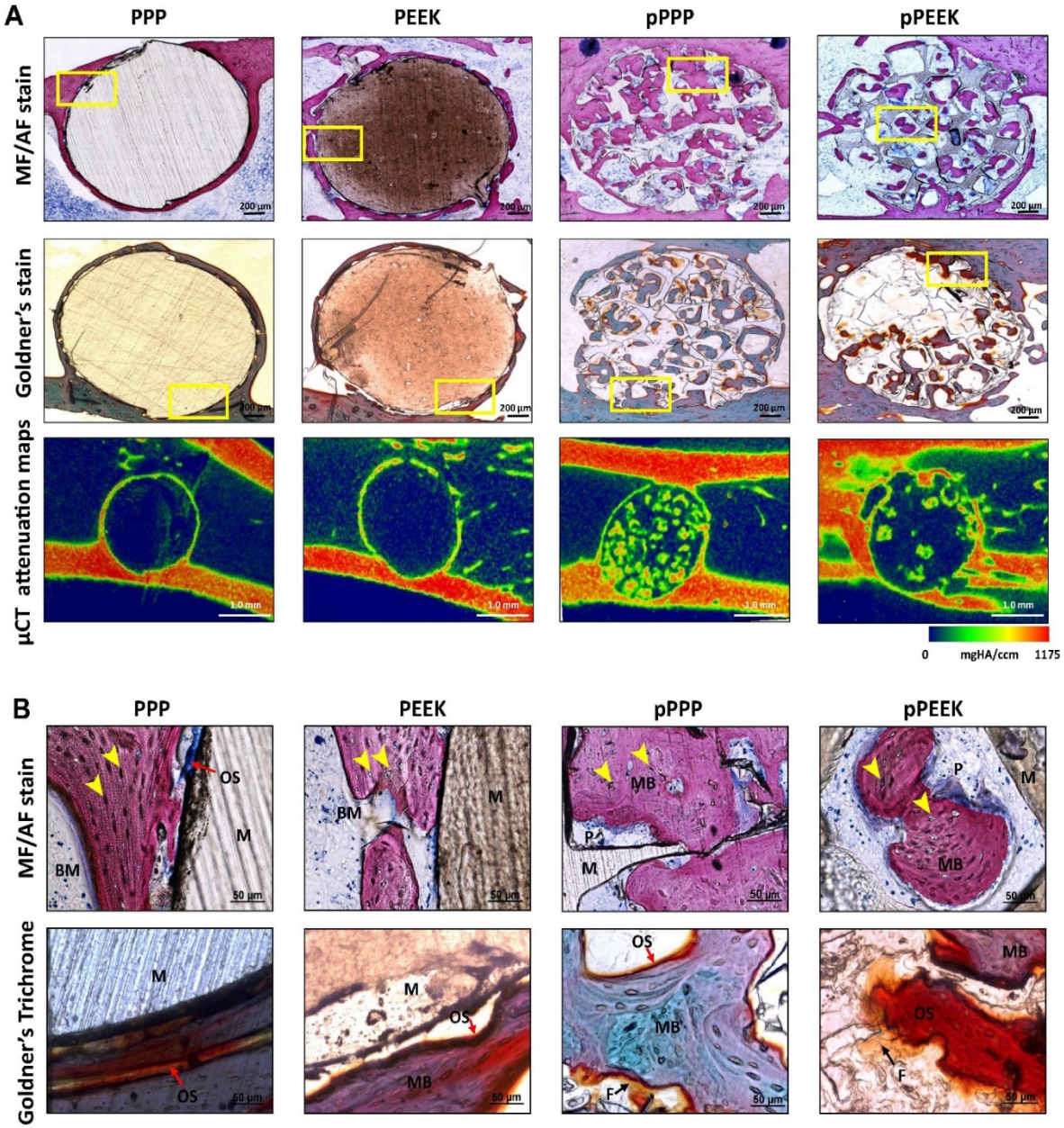

Figure 21:Histological analysis of bone ingrowth in implants. A) Coronal slices of implants with surrounding tissue. B) Magnified images of the same regions. Notably, pPPP showed enhanced cellularization and substantial bone formaiton. MB- mature bone (stained as pink in MF/AF staining or purple to green from Goldner's trichrome.; M- material (stained as brown); OS- Osteoid seam (red arrow); F-Fibrotic tissue (Black arrow); Osteocyte (yellow arrow); BM (bone marrow); P (implant pore)

implants; overall, there were no significant differences between solid (non-porous) implants (PPP 1.36±0.07 mm^3, PEEK 1.11±0.14 mm^3) **(Figure 20C)**. The porous PPP implants had a significantly higher BV compared to the other three implant types (11.57±0.38 mm^3; $p<0.0001$ vs solid PPP or PEEK). Specifically, porous PPP implants demonstrated a 40% increase in BV compared to porous PEEK ($p=0.0176$ vs porous PEEK). These data suggest that porous PPP may be an effective material for osseointegration due to remarkable mineralization than other materials.

Histological assessment showed bone formation throughout the porous PPP and porous PEEK structures (**Figure 21A**). Bone cells (osteocytes marked with a yellow arrowhead at **Figure 21B,** magnified images of **Figure 21A**) were observed in the mineralized new bone around the solid implants (stained as pink from MF/AF staining or stained as purple to green from Goldner's staining). In the porous implants, cubic shaped pores were filled with mineralized bone (**Figure 21B**). Similar to micro-CT analysis, porous PPP samples showed qualitatively more mineralized new bone formation, enhanced cell infiltration, and less fibrosis (yellow stain from Golder's trichrome staining) within the implant compare to porous PEEK implants. Representative micro-CT attenuation heat maps also showed the differences in new bone formation between porous groups (**Figure 21A**).

FE Simulated Push-Out Test

Using segmented implants from micro-CT scans, 3D models of implants with simulated bone ingrowth were generated and underwent a simulated push-out test. Reaction forces and load sharing were calculated for each type of implant. Load sharing and total push-out force is shown in **Figure 22**. Porous PEEK had a total push-out force of 367 N while porous PPP had a push-out force of 624 N. These forces equate to shear strengths of 21.3 and 36.5 MPa for PEEK and

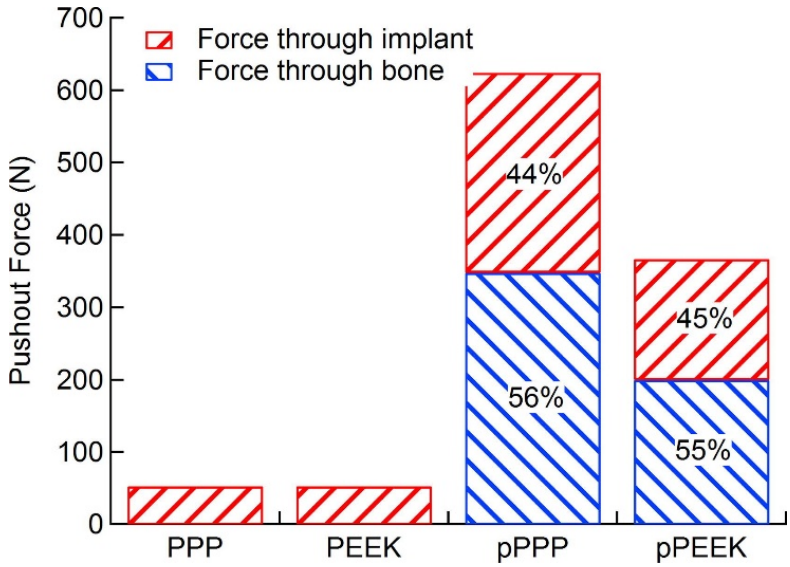

Figure 22:Total pushout force and load sharing behavior of solid/porous PEEK and PPP. Reaction forces from the bone and implant were taken to determine load sharing. Porous PPP showed significantly higher push-out force than porous PEEK. Load sharing between bone and implant in porous scaffolds was nearly identical. Both solid scaffolds showed identical push-out force with all force transmission through the implant as there was no bone ingrowth.

PPP, respectively. The load sharing between bone and implant in both porous materials were approximately the same at 45% and 55% for implant and bone, respectively. Both PEEK and PPP solid implants had push-out forces of 53 N with 100% of the force transmitting through the implant, as there was no bone ingrowth. The shear strength of both solid implants was 3.08 MPa.

Stresses were visualized as a heat map on the FE model to qualitatively show dissipation and average stresses were taken along the length of the implant to quantify the amount of stress dissipation within the implant. Stress dissipation within the various implants is shown in **Figure 23**. Both solid implants showed a relatively constant stress throughout the implant length with PEEK showing slightly higher stresses at all positions compared to PPP. Both porous implants showed a near linear decrease in stress from the initial surface to the end with average stresses in each implant decreasing approximately 80%. The porous PPP implant, which had greater bone ingrowth, showed higher average stresses throughout the implant compared to the porous PEEK.

Stress as a function of distance through the implant is shown in **Figure 23B**. Von Mises stresses in the implant were plotted with the loaded end on the left for all implants in **Figure 23A** with a

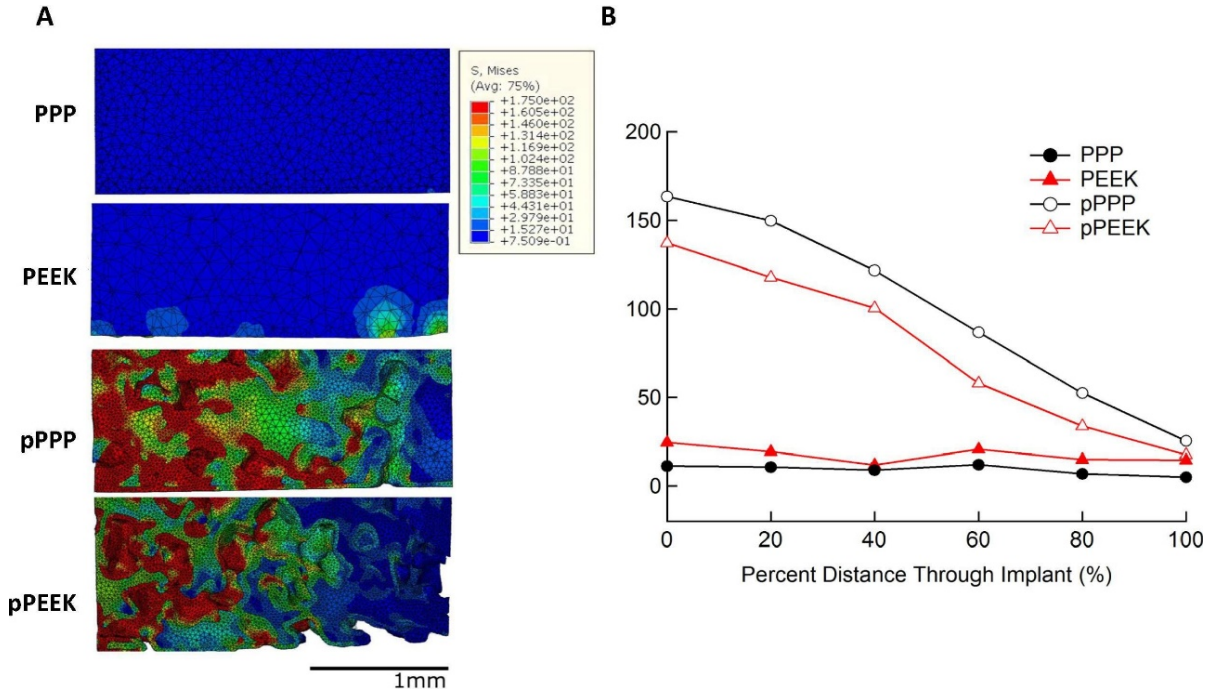

Figure 23: Stress dissipation within scaffolds during simulated push-out testing. heatmaps of von Mises stress within each scaffold type (left) showed little stress in the center of the implant for solid PEEK and PPP while both porous scaffolds showed high stress at the top of the implant which then dissipates moving through the implant. Average stress in the implant at equally spaced intervals (right) in the implant show porous PPP and PEEK having similar stress dissipation responses while there is no dissipation within the solid implants.

color map representing various levels of stress from 0 MPa (dark blue) to 175 MPa (red). Stress dissipation in the implants can be seen as the high stress red areas transition to green and blue along the implant length. Both porous implants showed a similar response, with the majority of stress being dissipated in the first half of the implant.

Apparent modulus and load sharing in representative cubes of porous PPP was calculated as a function of bone ingrowth and porosity. Apparent modulus of these cubes is plotted against bone ingrowth in **Figure 24**. Apparent modulus increased as a function of bone ingrowth for all porosities tested. The initial modulus for each porosity showed an inverse relationship with

porosity prior to bone ingrowth with 50% porous implants having the highest initial modulus (1125 MPa) and 85% porous PPP showing the lowest initial modulus (7.86 MPa). Each porosity

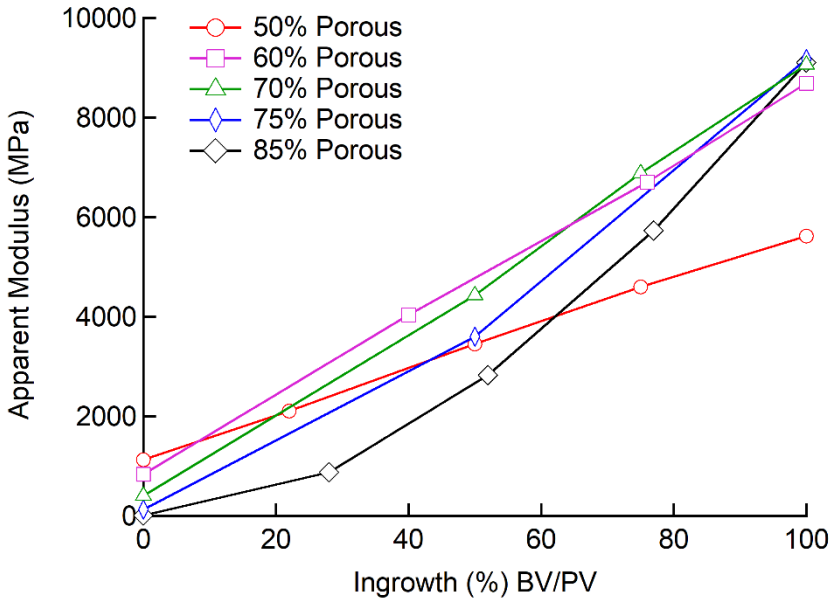

Figure 24: Apparent modulus of various porosity PPP implants as a function of bone ingrowth.

tested showed increasing apparent modulus with increased ingrowth. Interestingly, as porosity is decreased, the apparent modulus curves become more linear with the apparent modulus of 85% porous PPP showing a non-linear increasing response to bone ingrowth and 60% and 50% porosity having a linear response. Additionally, the 70%, 75%, and 85% porosity cubes seemed to converge at approximately 9000 MPa for 100% bone ingrowth, while 60% showed a lower apparent modulus at approximately 8500 MPa, and 50% porosity showing the lowest apparent modulus at 100% bone ingrowth at 5600 MPa.

Load sharing percentages for the bone and implant for each porosity are plotted as function of bone ingrowth in **Figure 25**. It was found that all implant porosities showed a similar load sharing response where initially all load is borne by the implant and gradually more load is transferred to the bone with increasing ingrowth after which the load sharing percentage plateaus. However, the rate of this transfer is different for each porosity with higher porosity

implants transferring load to the bone sooner and plateauing the load sharing percentage at lower ingrowths. Additionally, it can be seen that the ingrowth at which the majority of the load is taken by the bone decreases as the porosity is increased with 50% porous implants transferring a majority of the load to bone at approximately 70% ingrowth, 60% porous implants at

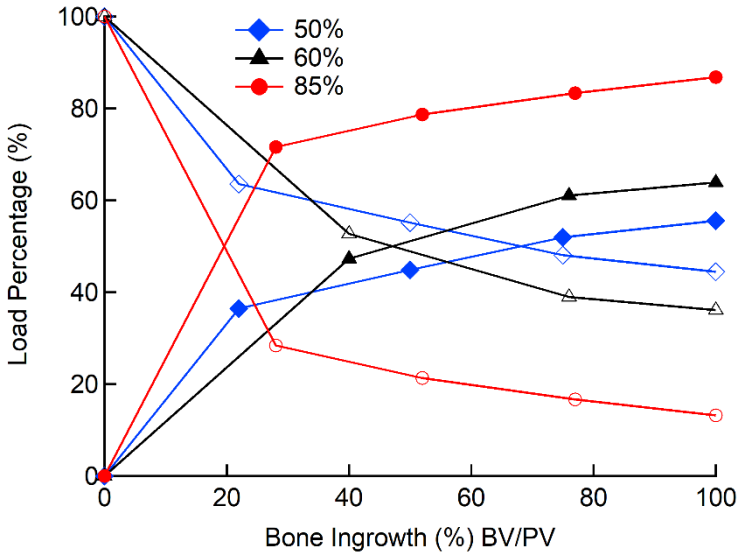

Figure 25: Load sharing percentage for 50, 60, and 85% porous ppp implants. hollow Markers indicate load through the implant while solid markers indicate load through the bone.

approximately 45% ingrowth, and 85% porous implants at approximately 20% ingrowth.

Discussion

The purpose of this study was to investigate the biological response of PPP as a novel load-bearing orthopedic material, and evaluate the mechanical properties associated with bone ingrowth by FE stimulated push-out simulation. It was hypothesized that high porosity throughout PPP implants (this study used 70% porosity) would allow for enhanced osseointegration and increased push-out force compared to solid implants as well as porous PEEK implants. The hypothesis was confirmed as this study demonstrated that porous implants showed higher cellular compatibility and osteogenic potential *in vitro* and increased osseointegration *in vivo* compared to solid implants. Porous PPP also showed higher

osseointegration and total bone volume following implantation when compared to both solid PPP, solid PEEK and porous PEEK. Finite element analysis predicted that this increased bone ingrowth would result in a higher push-out force compared to porous PEEK and both solid implants.

While many studies have analyzed the biological response to various porous scaffolds, previous studies have not yet examined the cell proliferation or osteogenic potential of PPP scaffolds, either with solid or porous architectures. This study demonstrated that mouse pre-osteoblasts could adhere and proliferate on both solid and porous PPP and PEEK scaffolds. While cell growth on porous materials peaked at day 3, cells grown on solid surface continuously proliferated over time. The difference in growth behavior could be interpreted as a consequence of geometric difference between in two different scaffolds (2D surface vs 3D surface). Additionally, several reports demonstrated that small pore sizes (96–150 μm) could facilitate cell attachment and proliferation [71]; however, a larger pore size was efficient to accommodate new bone formation and vascularization [72]. Our data also demonstrated substantial bone ingrowth within 420–500 μm pore size throughout the porous networks **(Figure 20)**. Early osseointegration has been shown to be influenced by surface topography, which is a crucial factor in determining cell adhesion and proliferation [73,74]. In this study, no significant differences in surface roughness were observed between the two materials, which may explain the similar cell proliferation rate between PPP and PEEK **(Figure 18)**. In both materials, osteogenic potential was increased in porous scaffolds compared to solid scaffolds **(Figure 3)**. Similar reports have previously been observed, [75,76] demonstrating bone cells in 3D culture secreted enhanced osteogenic specific proteins (e.g., osteonectin, type I collagen and alkaline phosphatase) and showed a 10-fold increase in mineral deposition compared to 2D cultures.

These studies also implicated surface roughness and architecture as a major contributing factor in the cellular response *in vitro*. Thus, a porous structure made from either material has the potential to be more osteocompatible compared to solid implants when translating these materials *in vivo*.

Osseointegration is a time dependent healing process beginning with cell adhesion [77] to the implant surface (i.e., peri-implant tissue formation) and matrix formation [78] subsequently leading to mineralization of the tissue [60]. Successful osseointegration can be categorized by direct anchorage of an implant without fibrotic tissue formation, which can interfere with the direct contact at the bone-implant surface resulting in implant failure and associated increased morbidity [79]. The porous PPP implants, as seen in **Figure 5,** were filled with cells and mineralized bone, consistent with micro-CT attenuation maps. On the contrary, porous PEEK showed significantly decreased mineralized bone ingrowth measured by micro-CT analysis and also showed some fibrotic tissue formation in the pores by histology. Evans *et al*., reported that surface-porous PEEK implants were filled with cellularized, mineralized bone with less fibrotic tissue compared to smooth surfaces [11]. In that study, the implants had a different pore size and porosity, 279.9 ± 31.6 μm and 67.3 ± 3.1% respectively, and were only on a thin surface layer; whereas, our implants had a larger pore size and porosity throughout the whole implant, which might have affected bone ingrowth. The difference in the material topography (surface porous structure vs entire porous structure) may be a critical factor affecting the biological response as well. While we did not do an isolated evaluation of mineralization into the surface layer of these constructs, it was apparent that more mineral formed in the porous PEEK samples in the surface layer compared to the central regions and may account for these differences. Overall, both studies showed significant osseointegration into these high strength polymeric scaffolds with

porous structures and suggests that the architecture and porosity is a critical factor in improving osseointegration of these materials.

The strong correlation between the measured and simulated apparent modulus measurements helped verify the utility of our finite element model. As such, we believe the simulated pushout test provided accurate results which match those seen in other studies. Based on the simulated push-out test, porous PPP showed a significantly higher push-out force compared to porous PEEK. This difference is likely attributed to the increased bone ingrowth seen during implantation in porous PPP. Additionally, PPP has a significantly higher yield stress compared to PEEK, and as such would show increased reaction forces during push-out. The total push-out forces were found to be comparable to those measured in previous studies. Oonishi *et al*., found surface porous titanium implants to have shear strengths of 25.4 MPa [72]. Additionally, Guyer *et al*., showed surface porous titanium and solid PEEK implants to have shear strengths of 10.2 and 1.5 MPa respectively [80]. Whereas we found push-out shear strengths of 21.3 and 36.5 MPa for porous PEEK and PPP respectively and 3.08 MPa for both solid implants. The differences in the finite element push-out and the experimental values seen here are likely due to the idealized nature of the model, with the bone perfectly following the pore shape with no gaps in bone growth. Both implants showed similar load-sharing properties, as the ratio of the bone modulus to that of the implants was similar in both cases. Furthermore, the porosity of each implant was the same, and as such there would be a similar cross-sectional area for bone and implant in each case.

In the case of load dissipation, both porous PEEK and PPP exhibited a similar response by dissipating approximately 80% of the stress through the implant in a linear fashion. The porous PPP implant displayed higher stresses through the entire scaffold than porous implant.

This phenomenon was due to the implants being modeled as a perfectly plastic material; the higher yield stress in PPP (approximately 50% higher than PEEK) allowed for an overall higher amount of loading before yield at all points along the implant. The solid implants on the other hand showed little stress dissipation, transferring most of the stress from the implant top to bottom. This observation may be explained by the majority of the stress being dissipated by struts within the porous implant and bone yielding during push-out. In solid implants, no such structure was available for dissipation of stresses applied to the implant. The ability of porous structures to dissipate this stress also afforded itself to more ideal load sharing with the bone, and showed a behavior which could not be captured by solid implant designs.

Apparent modulus calculations of porous scaffolds as a function of bone ingrowth are important to the adequate design of implants to correctly analyze the mechanical behavior of a porous orthopedic implant over time. The results from this study revealed that the apparent modulus of a given porous scaffold will increase with increased bone ingrowth due to the decreased free volume within the structure and the higher modulus of bone (13-18 GPa) compared to pPPP (4.5 GPa). It should be noted that there have been no previous studies analyzing the mechanical behavior of porous PPP as a function of bone ingrowth. Previous research regarding pPPP as an orthopedic biomaterial have focused on its initial material properties prior to any bone ingrowth. DiRienzo *et al*. found a similar response to the initial moduli seen in this study while measuring the apparent modulus of porous PPP scaffolds ranging from 50 to 90% porous. The 50% porous scaffolds showed near identical moduli to those calculated in this study; however, moduli for higher porosity samples in their study tended to have higher moduli. This is likely due to the small size of the cubes modelled in this study as there is a notable size effect in porous materials with smaller samples tending to have a higher

proportion of their volume made of up peripheral pores which do not contribute to the mechanical properties seen in larger samples. Modelling of a larger cube in this study would provide a more accurate modulus calculation; however, this would prove to be limited by the computational power required for large models.

To fully quantify the behavior of a porous implant in the body, it is necessary to analyze the effect of bone ingrowth and how the behavior of the material will change over time. Studies have investigated the effect of bone ingrowth on the mechanical properties of metal foams or biodegradable scaffolds and have found similar results to those seen here. Li *et al*. found that the apparent modulus of porous tantalum and nickel-titanium scaffolds increased with bone ingrowth; however, the resulting relationship between ingrowth and modulus cannot be directly compared to this study as they utilized materials significantly stiffer than PPP, which would alter the modulus response to ingrowth. Martin *et al*. found a linear response between ingrowth and modulus described by the equation Y=26.5X-134 where Y is the modulus in MPa, and X is volume fraction of ingrowth as a percentage. The authors utilized 65-75% porous hydroxyapatite scaffolds and showed ingrowth percentages of approximately 75%. This study found similar results for the tested porosities in that range. The 60 and 70% porous implants showed relatively linear responses up to 75% ingrowth.

The load-sharing response seen in this study has not been previously reported for porous PPP implants. A recent study by Carpenter *et al*. found similar responses for porous PEEK and titanium implants with an increasing load being transferred to the bone with increasing ingrowth. Interestingly, that study also noted that at no point after ingrowth in the porous titanium implant did the bone bear a majority of the load, lending credence to the use of porous polymeric materials for orthopedic applications. The response seen in this study is indicative that novel

polymeric scaffolds using PPP could be used to provide varied mechanical properties over time in a manner which optimizes loading onto the bone over time, possibly by varying porosity throughout the implant to provide additional loading to the bone where additional ingrowth is needed.

The solid implants used in this study are representative of current spinal fusion cage designs; made up of solid materials, which can only interface with the bone at their surface and have moduli significantly higher than the bone at the vertebral endplate (typically by an order of magnitude) [81]. This disparity between the mechanical properties of the implant and vertebral bone is believed to be a leading cause of complications post-implantation due to subsidence [10]. The high modulus of the implant relative to the bone leads to stress-shielding and stress concentrations on the vertebral endplate, increasing the likelihood of subsidence. Porous PPP represents a possible solution to these limitations as it possesses a modulus much closer to that of trabecular bone and, as we modeled in this study, is able to dissipate stress within the implant. In addition, the finite element models presented that porous PPP evenly shared the load with the ingrown bone and dissipated stress upon loading. These two results together suggest that porous PPP would be able to minimize stress shielding, decreasing the likelihood of subsidence following fusion with a porous PPP device. Also, the ability to interface with the bone throughout the implant could allow for increased strength due to the mechanical interlocking of the bone and the implant rather than simply due to friction at the surface [82]. However, despite the enhanced osseointegration of porous PPP, further fundamental investigation is needed such as protein adsorption to the surface and fibrin network formation to influence the local osseointegration within the scaffolds.

In conclusion, the porous PPP material demonstrated excellent cellular compatibility and strong integration with living bone, which are critical factors in load bearing implants. The use of porous PPP in orthopedic implants can offer many benefits, which may be advantageous compared to current spinal fusion devices, including ones made from porous PEEK. Specifically, the high yield stress and modulus of PPP allows for the introduction of high porosity in the implant without sacrificing mechanical integrity. Moreover, the ability of porous polymer implants in general to dissipate stress demonstrates a fundamentally unique behavior which cannot be captured by solid implants or metal implants. The exceptional properties of PPP suggest that it could be uniquely suited to such applications. PPP is a highly promising orthopedic biomaterial with relative flexibility in manufacturing processes, a favorable biological response, and comparable mechanical properties to native bone.

CHAPTER IV

EVALUATION OF VERTEBRAL ENDPLATE STRESSES UNDER LOADING WITH VARIOUS IMPLANT DESIGNS: FINITE ELEMENT GUIDED DESIGN OF LUMBAR INTERBODY FUSION CAGES WITH POROSITY AND CONTOURING

Introduction

Lumbar interbody fusion is one of the most common surgical methods of treating severe back pain due to disc degeneration and spinal stenosis. According to Millennium Research Group, over 237,000 procedures were performed in 2013, and this number is expected to grow to over 357,000 procedures by 2023.[50] This procedure, can lead to significant complications after surgery. The most commonly occurring complication following lumbar fusion is subsidence of the implant and graft into the vertebral endplate, with subsidence rates following surgery ranging from 17% to 52% of cases. It is currently believed that subsidence occurs due to a large mismatch in material properties between the endplate and the fusion cage, with the cage often being significantly stiffer and stronger than the vertebral bone; however, there has not been a conclusive study which investigated this claim clinically. Previous studies have shown that the use of more compliant materials such as PEEK compared to titanium implants significantly decreases endplate stress and decreases the risk of subsidence.[81] It is currently believed that use of a more compliant material will reduce endplate stress by reducing the material mismatch between the vertebral bone and the implant. Several studies have also shown that lowered bone mineral density is a strong predictor of subsidence risk. This observation further enforces the concept of material mismatch leading to subsidence, as with decreased bone mineral density, the overall modulus of the bone would be further decreased, exacerbating the mismatch between the implant and bone. In order to minimize this effect, current medical device companies have begun development of novel implants that use porous materials to better distribute stresses across the endplate .[58,83-85] The assumption behind porous implants is they are better able to distribute

stress due to the ability to conform to the endplate and reduce stress concentrations at the implant boundaries. Further, porous implants allow for osseointegration at the endplate surface preventing implant migration following surgery. Other factors such as implant geometry may play a significant role in minimizing subsidence. A study by Chatham *et al*. proposed a customized spacer designed in a manner which contours the endplate to reduce stresses. It was found that this design reduced endplate stresses for each material used. The study also found that the use of solid implants made of PEEK or titanium did not provide a significant difference in endplate stress, but that the use of a less stiff material such as porous titanium or porous PPP significantly reduced these stresses.[86] It has been proposed that the contact area between implants and endplates significantly affects subsidence rates; however, studies which have analyzed this have found mixed results, indicating other factors likely play a role in dictating endplate stresses. For example, Steffen *et al*. found that an implant fully covering the endplate and one with the same outer footprint but an open center demonstrated the same compressive strength and ultimate strength.[87] Other studies have found that a single implant placed obliquely in the center of the endplate reduces endplate stresses more than two implants placed in parallel.[88] The exact mechanisms behind these variations remain unclear and the effectiveness of drastic implant design changes remains uninvestigated.

To date, no studies have conducted a cross-sectional test of multiple implant designs with patient tailored mechanical properties, implant-bone conformation, total implant-bone contact area, and introduction of implant surface porosity. It is currently unknown whether matching material properties of the implant to those of the patient's endplate will help reduce stress concentrations. Previous investigations of endplate stresses have utilized grayscale-based bone material properties, which do not adequately capture the structural effects of the vertebral body on the

endplate properties. Further, it is currently unknown whether tailoring material properties of the implant to match those of the patient can help reduce stress concentrations or if customized material implants provide additional benefit beyond that of fully porous implants. Understanding the cooperative and synergistic effects of various design choices such as material or geometric variations is vital to the design of spinal cages and can lead to improved designs which reduce the risk of endplate subsidence due to stress concentrations. The purpose of this study is to perform a cross sectional analysis of various design parameters in lumbar interbody cages and determine the design which best minimizes endplate stresses.

Methods

Designs Tested

This study systematically analyzed a variety of design parameters which have been shown to affect endplate stresses in polymer based fusion cages. A table of implant designs tested in this study can be seen in **Figure 26**. Implants were designed to have the same overall footprint while varying the geometry of the graft holes and the material of the implant. With regards to implant geometry, variations included a traditionally shaped implant with two large holes for bone graft, an implant with drastically reduced graft holes, and both of these designs with contouring to match endplate geometry. With regards to material changes in the implant, the designs were modeled either as solid implants made from PEEK, fully porous implants made from PPP, a surface porous implant with a solid core and a layer of porous material at the surface, and implants with material properties tailored to match those of a patient. Traditional cages were not assigned patient-specific properties as there would not be enough material within the implant to feasibly create the porous zones to match the endplate moduli, and the implant would realistically be too weak to support significant loading seen in the spine. The total area of

contact with the endplate and volume available for bone ingrowth (either into pores or large holes) were also determined for each design.

Finite-Element Modeling

Multiple implant parameters were chosen for analysis and were categorized into either geometric or material variation in the design. Traditional implant geometries were used as a

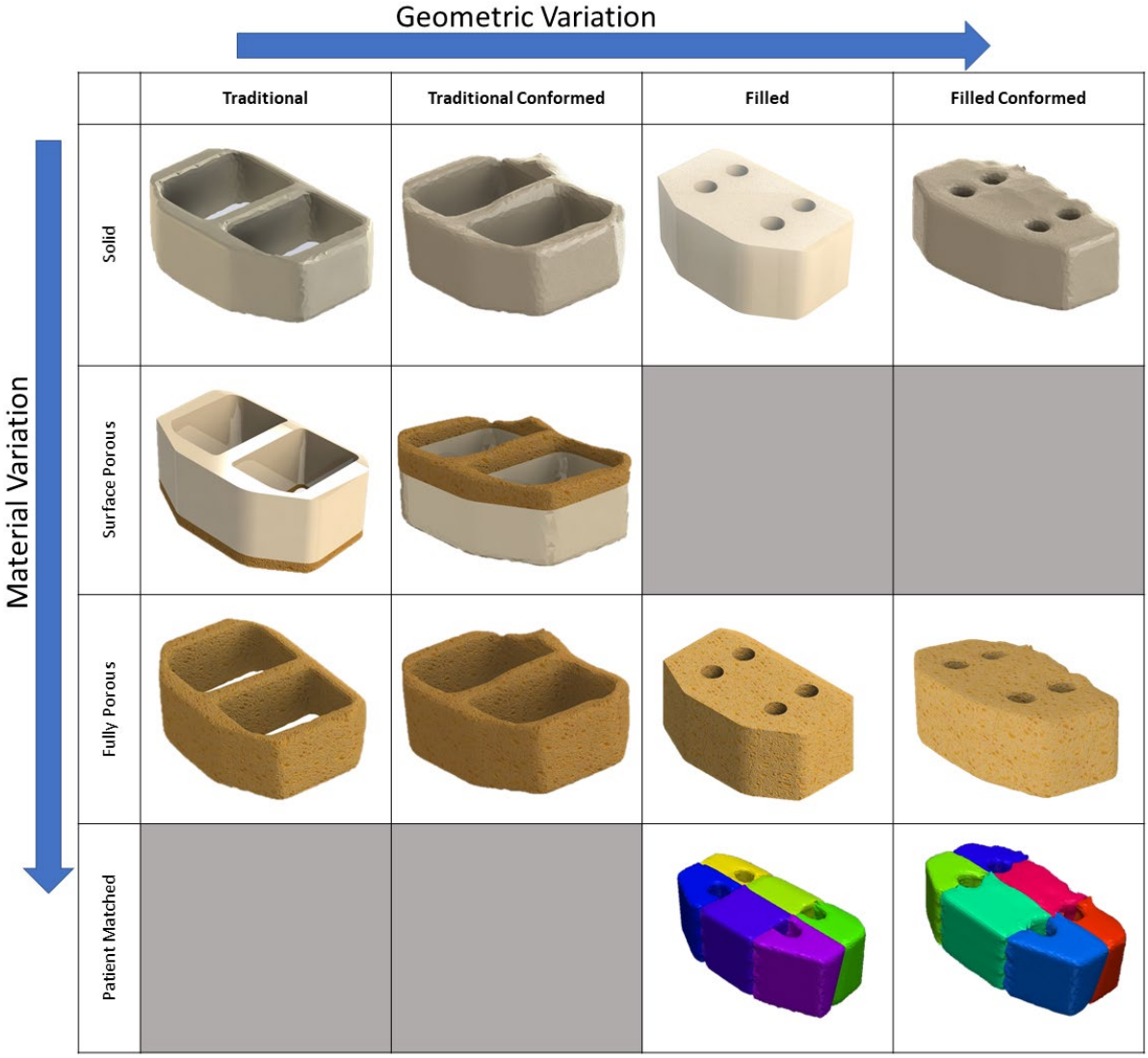

Figure 26: Design matrix depicting all implant designs and material variations tested.

representative geometry for current implants on the market. Filled implant geometries were modelled as implants to maximize the contact area with the endplate by removing the internal bone graft holes while maintaining the same standard outer geometry of the traditional implants.

Conformed implant geometries utilized the same outer footprint of either the traditional or filled implants, but their shape was contoured to match the patient's endplate geometry exactly. Solid material implants were modelled as solid PEEK as implants currently available on the market. Surface porous implants were modelled to analyze the effects of surface porosity as utilized in some newly available implants. Full porous implants were modelled with the material properties of 70% porous PEEK, and patient matched implants were modelled by taking the average of the modulus under each of the 6 zones shown by the colors in Figure 26. Surface porosity was not modelled with the filled style implants as traditional style surface porous implants were only modelled to analyze the implants currently available on the market. Patient matched properties were not applied to the traditional or traditional conformed implants as there would not be enough material in the implant to divide it into the various zones as seen in the filled implants.

The L2 vertebral body was segmented from CT imaging of a cadaveric spine using Simpleware ScanIP (Synopsys, Mountain View, CA). The endplate was segmented as a separate

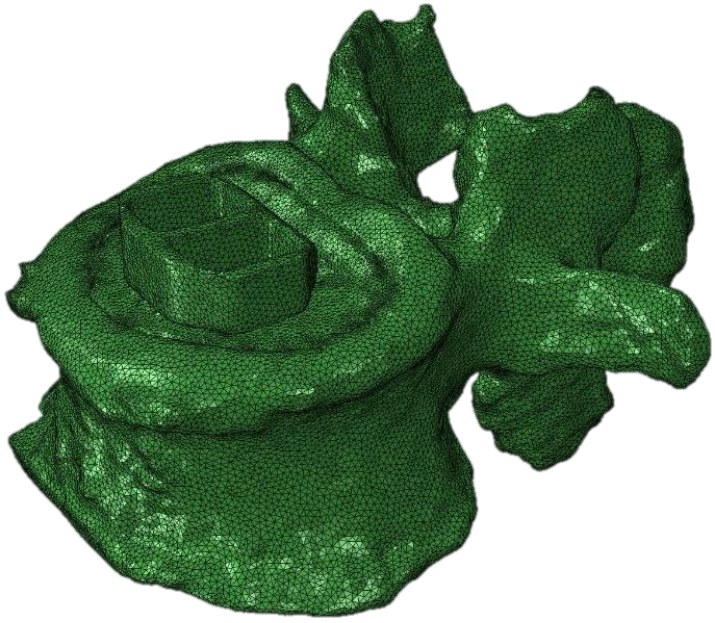

Figure 27: Representative image of the finite element model used in the study. The separately segmented endplate can be seen below the traditional geometry implant.

mask from the rest of the vertebral body. Grayscale-based material properties were assigned to

the vertebral body using the method described in Matsuura *et al*.[89] In brief, grayscale values from the CT image were correlated to bone mineral density (BMD) using a quantitative CT phantom produced by Mindways (QCT Pro, Mindways, Austin, TX), which was then used to assign mechanical properties using an empirically fitted equation. Implants were placed on the endplate

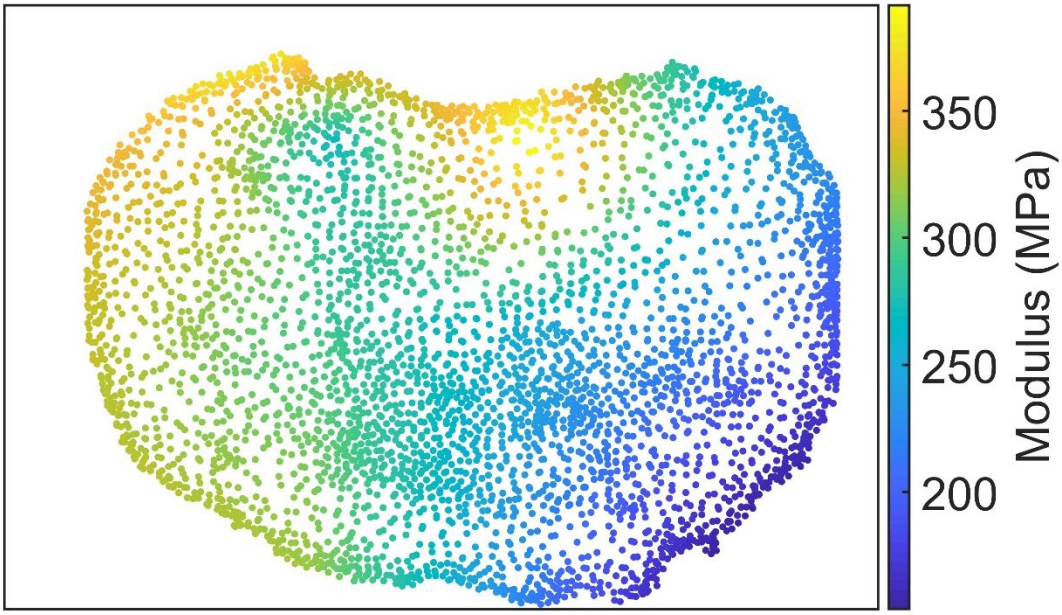

Figure 28: Heatmap of interpolated modulus on the endplate utilized in the finite element model.

in a manner which minimized overlap of the endplate and implant masks, after which the model was either meshed directly in the case of non-contoured implants, or implant material was then added to match the geometry of the endplate. A contact surface was defined between the implant and endplate for all implant types to simulate the interface immediately following surgery, prior to bony ingrowth around and through the implant body. Following meshing of the model with linear 4-node tetrahedral elements, moduli of the endplate elements were assigned via two-dimensional interpolation of values measured using indentation in a previous study [90] Based on the coordinates of the element centroid, the modulus was interpolated using a custom MATLAB code to output a modified ABAQUS input file. The MATLAB code used in this study is

provided in the appendix. A heatmap of interpolated moduli for the endplate is shown in **Figure 28**. The endplate modulus showed distributions similar to those described in literature. Modulus tended to be higher in the posterior portion of the endplate and lower in the anterior portions. Additionally, implants were placed in areas bounded by the experimentally measured points to minimize the effects of artifacts from interpolation at the periphery of the endplate.

Loads applied to the implant were based on OrthoLoad data for a vertebral body replacement for walking at 6 km/.[91] Loads were applied to the implant under the assumption that posterior fixation would be used during the procedure to reduce endplate loading. According to Ahn *et al*. 2008, posterior fixation using titanium rods bears approximately 71% of axial load applied across a motion segment. Using this assumption, the load applied to the endplate was 29% of the maximum force seen in the OrthoLoad data.[91] Loads were assigned in ABAQUS as concentrated forces across the superior surface of the implant. The total applied load was divided amongst each node, to give a total static load of 211 N applied axially. Loading was applied evenly as load distributions across the endplate are typically relatively uniform.[92] A pinned boundary condition was applied on the inferior endplate to prevent translation of the vertebra during loading. Stresses for all elements within the endplate were recorded to determine the effect of various implant designs on endplate stress concentrations as well as stresses within the implant to determine long-term viability of each implant type. All solid models used PEEK material properties with E=4,100 MPa, ν=0.3 while porous cages utilized properties for a 70% porous PEEK (E=369 MPa ν=0.1 calculated using the Gibson-Ashby cellular solid model).[48,93] Patient matched implants used properties that matched the endplate properties as measured in a previous study.[90] Patient matched implants were divided into 6 zones which had material properties based on the average of the endplate moduli under each region **(Figure 26)**.

Results

Endplate Stresses

Finite element analysis of the implant-bone interface between a fusion cage and the vertebral endplate was conducted to evaluate stress concentrations for the different implant designs. Images of the endplates following this analysis are shown in **Figure 29**. Non-conformed designs produced high stress concentrations at areas of the endplate in contact with the implant which tend to concentrate at the edges of the endplate due to its naturally concave shape. The concentrated areas showed high stresses in excess of 5MPa ranging to over 150 MPa in the case of the traditional solid design. High stress areas tended to fall on the highest points of the endplate with all traditional design implants showing concentrations in the same areas.

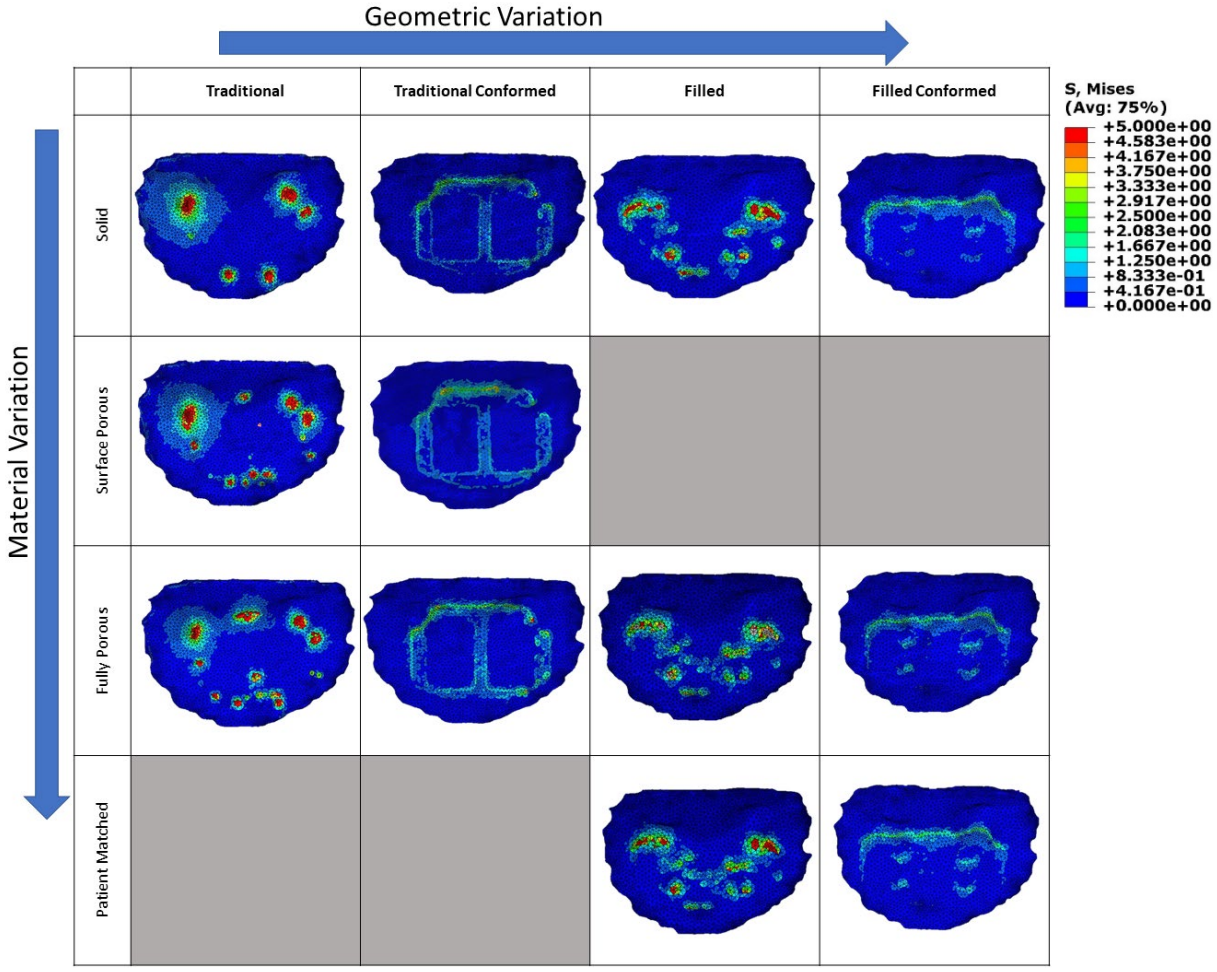

Figure 29: Stress heatmaps of the endplate after loading with various implant designs.

However, as the porosity of the implant is increased, additional areas on the endplate begin to come in contact with the implant and transfer stress. For example, in the traditional solid implant, stress concentrations tended to fall to the lateral sides of the endplate, but with increased porosity from the surface porous and fully porous implant, additional concentrations developed in the center, indicating that the implant is flexing to come in contact with the endplate. Though additional areas began to experience stress, the overall level of the stress on the endplate was decreased with increasing porosity. The same result is seen with the filled implants, with the solid filled implant experiencing stress concentrations at more places compared to the solid traditional cage, but with lower peak stresses (approximately 30 MPa) compared to the solid traditional implant. Reducing the modulus by increasing porosity or matching the patient endplate modulus did not result in large reduction in endplate stresses.

While non-conformed implants showed areas of high stress concentrations between 30 to 150 MPa, endplate conformed cages reduced these concentrations to below 5 MPa ranging from 2 to 3 MPa across the endplate surface. Endplates loaded with conformed implants exhibited stress outlines in the shape of the implant rather than stress concentrations at the highest points on the endplate as is the case in the solid implants. Solid conformed cages produced large reductions in stress across the endplate, reducing peak stresses by approximately 85% between the traditional solid cage and the traditional conformed solid cage. Fully porous conformed implants demonstrated a similar behavior to the solid material implants, in that the conformed designs produced significantly lower stresses that were more evenly spread across the endplate. Filled and conformed implants had the lowest stresses for all 3 materials. Stresses were concentrated at the posterior portion of the endplate and at the graft holes in the footprint of the implant. Stresses did not appear to vary significantly between the various materials used. The

traditional conformed implants experienced higher stresses than the filled and conformed, and they had lower stresses than those of the non-conformed implant designs. The overall footprint of the stress can be seen to increase as the material is varied from solid to fully porous, indicating more of the implant comes in contact with the endplate after loading.

To better understand the distribution of stresses on the endplate, a box and whisker plot of endplate stresses for each implant design is shown in **Figure 30A**. The variations in implant design did little to reduce average endplate stresses compared to a traditional solid cage. There are slight decreases in average endplate stress by changing the implant material from solid to porous to patient matched. For example, in the filled implants, solid, porous and patient matched implants led to average endplate stresses of 0.295 0.294, and 0.293 MPa, respectively. This result was unexpected, as previous studies have shown reduced implant modulus to significantly reduce endplate stresses. However, when focusing on the regions of highest stress on the endplate, the effect of implant design was more evident. Another box and whisker plot of endplate stresses for each implant type can be seen in **Figure 30B**. In this case, the outliers (elements with F-scores more than 1.25 times the interquartile distance) are plotted as well, and a striking result can now be observed. It can be seen that implant geometry, namely contouring to the endplate surface, led to a dramatic reduction in peak endplate stress values. Further, the filled implants had significantly reduced stress concentrations compared to traditional implants. These results suggest that increasing surface contact between the implant and bone is more effective at reducing endplate stresses than using a more compliant material. Rather than decreasing the average endplate stress, increasing surface area in contact with the endplate lowers the magnitude of the highest stresses on the endplate. A plot of average endplate stresses

normalized to that of the traditional solid implant is shown in **Figure 31**. This result reveals that all implant material and geometric changes will reduce the average endplate stress

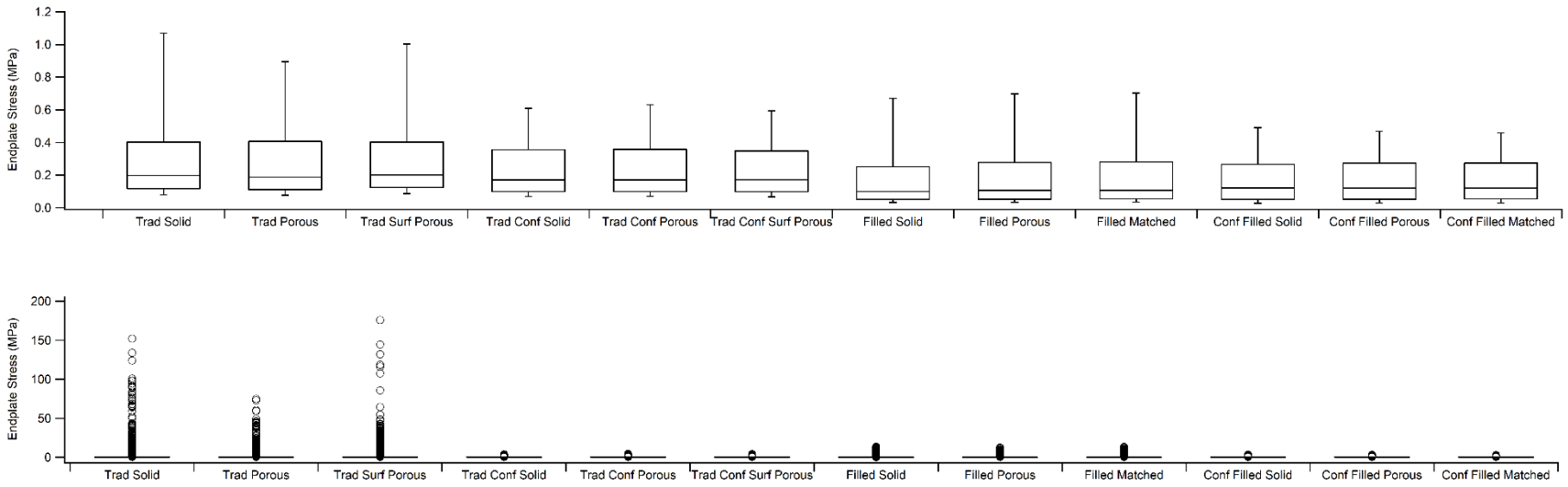

Figure 31: A) Box and whisker plot of endplate stresses for each implant design tested. B) box and whisker plot of endplate stresses for all designs tested.

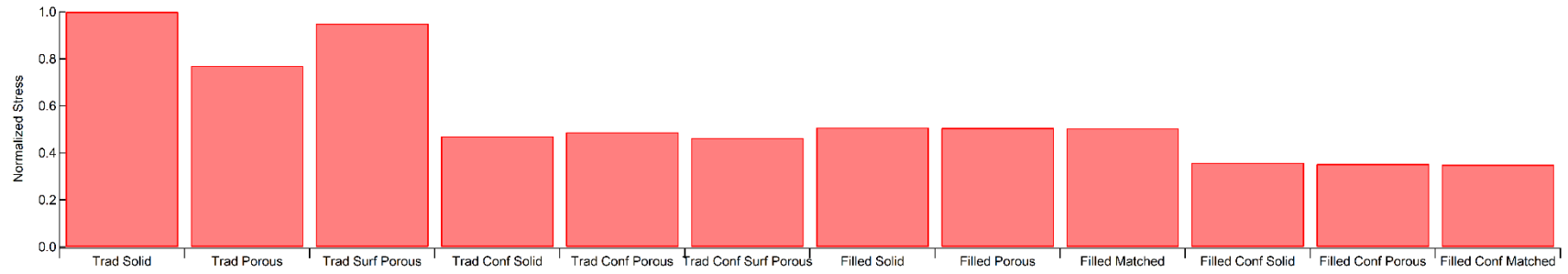

Figure 31: Average endplate stress for each implant type normalized to average endplate stress for the traditional solid implant

compared to the traditional solid material design. However, the extent of the reduction is highly dependent on the exact variation in question. For example, the surface porous traditional implant only showed a reduction of approximately 5% compared to the traditional implant while the fully porous traditional implant showed approximately 22% reduction in average endplate stresses. All other designs showed reductions of at least 50% in all cases. The filled conformed implants showed the greatest reduction in endplate stress compared to the traditional cage designs, reducing average endplate stress by 65% in all three cases. Additionally, variation in material between solid, porous, and patient matched showed little reduction in average endplate stress.

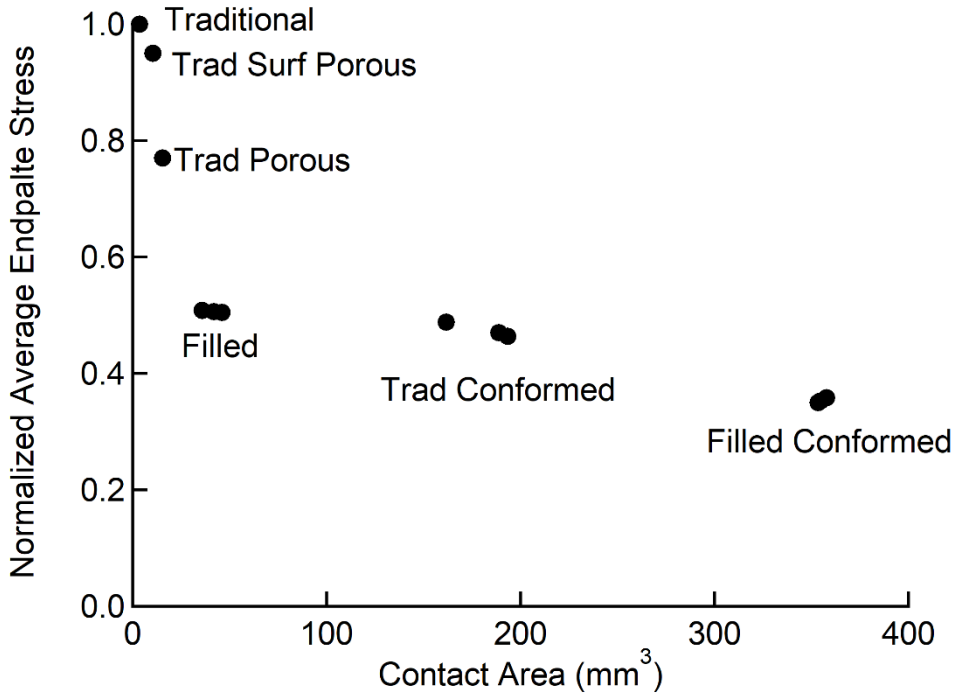

Figure 32: Contact area between the bone and implant following loading for each implant design vs normalized average stress. A diminishing response is seen with increased contact area beyond approximately 50 mm^3. Changes in material within a given implant geometry do not appear to have a large effect on average endplate stresses.

The filled implants showed reductions of 50% for all three designs and again achieved very little reduction by material variation. These results also correlate strongly with the amount of contact area between the endplate and the implant. A plot of the normalized stress vs the contact area

after loading can be seen in **Figure 32**. An initial sharp decrease in average stress can be seen as contact area increases, but further increases in contact area lead to a much more gradual decrease in average endplate stress. Initial increases in contact area as seen from the traditional solid to traditional conformed solid implant (3.61 mm^2 to 188.7 mm^2) resulted in a large reduction in endplate stress of approximately 50%. Material variation for a given implant geometry created negligible reductions in average endplate stress in the case of implants with an available surface contact area greater than 50 mm^2.

Implant Stresses

In addition to investigating the endplate stresses, the influence of these parameters on the stresses

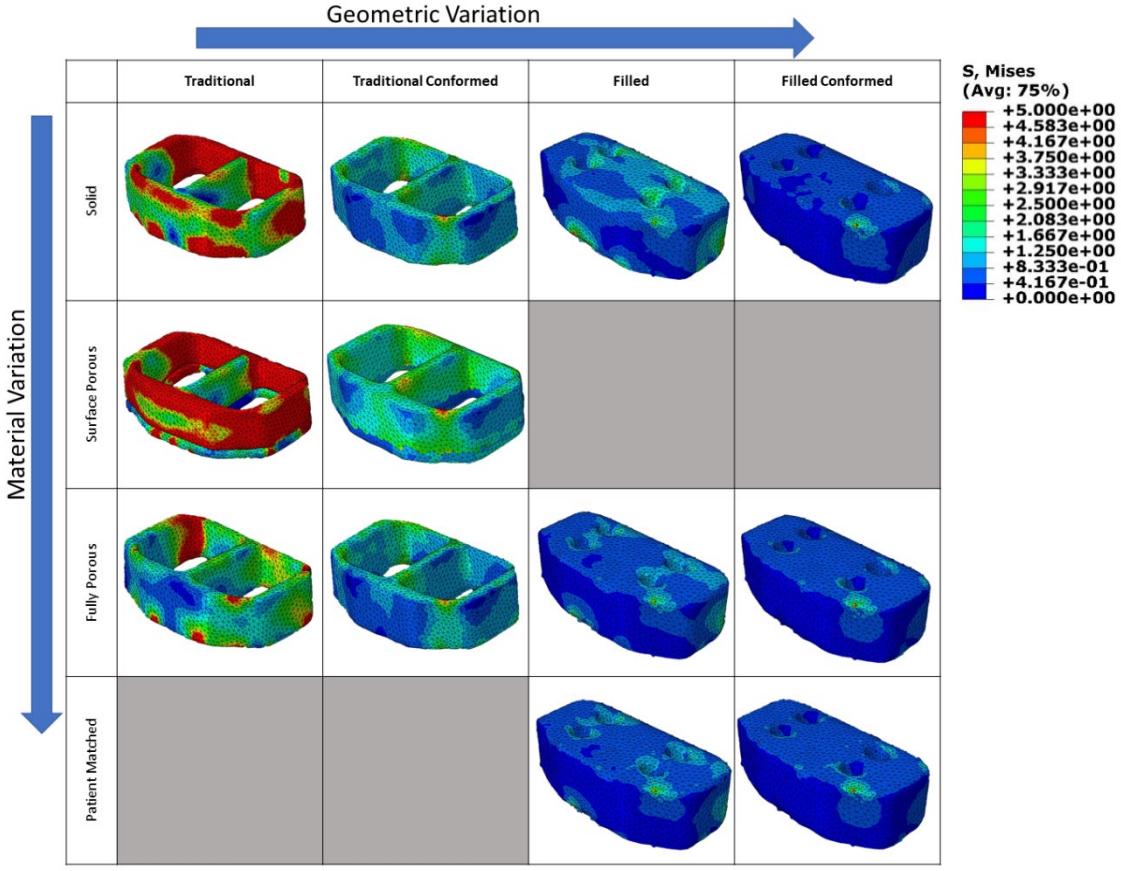

Figure 33: Heatmaps of stress within the implant body. stresses greater than 5MPa are shown as red. It can be seen that stresses are highest in traditional solid implants. Conformed implants show the lowest stresses for any design type and increasing porosity

within the implant body was analyzed to asses viability of long-term implantation. Heatmaps of

implant stresses can be seen in **Figure 33**. Traditional implants were found to have the highest stresses within the implant body for any design type, while filled conformed implants were shown to have the lowest stresses. Increasing cross sectional area of the implant had the greatest effect on implant stress, as shown by the transition from a traditional to filled cage. Additionally, introducing porosity produced a dramatic reduction in stress. The traditional porous implant experienced much lower stress compared to the solid material implant. The same result can be seen in the other 3 implant geometries; however, the effect is diminished by their increased cross-sectional area.

Implant stresses are shown as a box and whisker plot in **Figure 34**. It can be seen that varying the material from solid to fully porous dramatically decreased the stress within the implant. In the case of the traditional design implants, the average implant stress is reduced from approximately 4 MPa to 2MPa by changing from a solid PEEK implant to a fully porous PPP cage. Stresses within the surface porous cage were plotted as two separate bodies: the main body of the cage and the porous layer. The porous layer showed significantly less stress than the

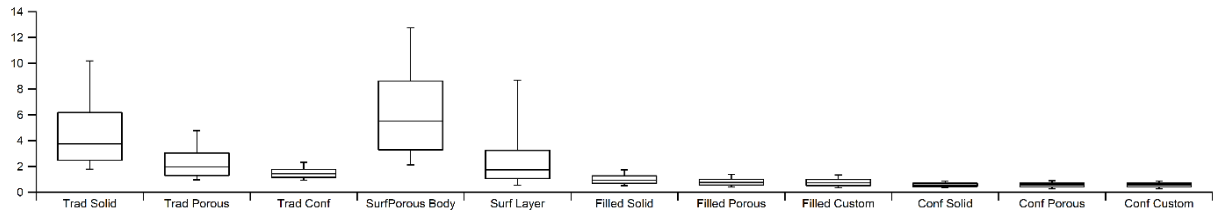

Figure 34: Distribution of stresses within the implant body for various implant designs. Whiskers represent the 90th and 10th percentiles, boxes represent 70th (top), median (center), and 25th (bottom) percentiles.

body; however, it showed higher average stresses compared to the fully porous implant. Further, the solid portion of the surface porous implant showed higher stresses than the traditional solid implant indicating that the combination of a porous layer on a solid body leads to some sort of stress concentration. The filled and conformed cages experienced lower stresses compared to the

traditional designs due to their increased surface area. The conformed cages had the lowest overall stresses, because they were conformed to the endplate, maximizing their contact surface.

Discussion

The purpose of this study was to analyze endplate stresses under loading with various implant designs and materials and to determine the design and material choice that best minimizes stress concentrations in the endplate as well as implant. This study presented a design matrix to evaluate the endplate stresses experienced under loading with various implant designs using FEA. Previous studies have investigated this phenomenon; however, these studies were limited to single material changes or to evaluations of single designs. This study attempted to evaluate combinations of these variations to determine if there were any synergistic effects between geometric as well as material changes to the implants. It was found that implant conformity to the endplate was the single most effective means of reducing stresses on the endplate. As shown in **Figure 31**, increases in contact area provided the greatest reduction in endplate stresses. While there were minor reductions in endplate stresses by using porous materials and matching the properties to the patient, these reductions were negligible compared to the reductions seen in conformed implants.

With regards to endplate stresses, previous studies have shown that reductions in implant moduli significantly reduce endplate stress with traditional cage designs. For example, Vadapalli *et al*. found that reducing the implant modulus by switching from titanium to PEEK cages reduced endplate loading and reduced subsidence risk.[4] In this study, it was found that further reducing the implant modulus led to a somewhat diminished return on endplate stress reduction. The reduction of modulus from 4100 MPa for a solid PEEK implant to 369 MPa for a fully porous PEEK implant only reduced endplate stress by approximately 0.3% and further reducing the modulus by matching the modulus to the patient reduced it by an additional 0.2%. It should

be noted that the introduction of porosity in this implant substantially reduces the overall strength of the implant, removing its utility as a load bearing implant. This study demonstrated that customizing the implant material to a patient's endplate properties did not substantially decrease endplate stresses. Rather, the largest effect seen in this study was the conformation of the implant to the endplate surface, which led to dramatically reduced stress concentrations. This result agrees with previous studies that analyzed the effect of implant conformation on endplate stresses. Chatham *et al*. demonstrated diminished endplate stresses using a porous PPP implant conformed to the endplate. Further, other studies have analyzed the use of 3D printed patient specific cages to conform to the endplate.[86] Spetzger *et al*. demonstrated the workflow for manufacturing and implanting a patient-specific selective laser melted titanium cage for cervical fusion.[94] The implanted cage significantly increased the load bearing area across the endplate and showed potential for significantly reducing subsidence. The case study also mentioned the added benefit of preventing implant dislocation due to the mechanical interlocking of the cage to the endplate, preventing any lateral translation of the cage after implantation. A study by de Beer *et al*. mechanically tested various spinal segments using a traditional vs a conformed implant. The contact area at the bone interface under loading as well as the total stiffness of the segment were analyzed and found to be significantly increased in conformed cages with a 137% increase in stiffness using a conformed cage compared to a traditional flat cage.[95] These results support our data, as the increased contact area will further increase the stiffness by reducing stress concentrations and significantly reducing subsidence. Further, a recent patent by SpineMedica LLC. claims the workflow of developing a patient specific implant for fusion cages. The patent details an automated process with options for user input for developing a conformed implant based on patient CT data.[96] These recent studies and patents demonstrate

that current developments in the spinal fusion market are moving towards a customized implant for each individual patient.

This study also demonstrated that increased area in the case of the filled implants reduced endplate stress concentrations. This result was somewhat expected, as previous studies have indicated the use of multiple implants or the use of implants with larger footprints will significantly reduce the endplate stresses by dispersing them across a larger area. Kumar *et al*. found similar results while comparing ALIF cages to PLIF cages and those made from mesh.[97] The resulting stresses within the vertebral body were maximized with mesh cages with the smallest contact area while they were smallest with the ALIF cages with the largest contact area. A study by Steffen *et al*. found that cage surface area did not have a significant effect on fusion construct stiffness or ultimate strength and that an implant with 30% endplate coverage provides the same properties as one with full support. However, this study utilized cages with serrated teeth on the surface for better anchoring of the implant to the endplate surface. These teeth also lead to significant stress concentrations, which would be expected to alter the mechanical behavior of the implants and confound the direct comparisons between the implant designs.[87] It should be noted that, while maximizing the contact area with the bone reduces the overall endplate stresses, it does minimize the amount of bone graft in contact with the patient's natural bone, potentially hindering fusion.[98] A balance must be struck between these two factors, and future research could investigate the effect of graft contact vs. implant contact area with the patient bone. However, in the case of this study, it should be noted that the use of a filled implant with smaller graft holes necessitates the use of a porous material. A solid implant with this design would not permit a significant amount of bone ingrowth, leading to a potentially unstable fusion construct and potential non-union of the vertebrae following surgery. With a porous

implant, bone can fully infiltrate the internal structure of the implant, allowing for more ingrowth for fusion. Additionally, the surface area is not the only factor which affects endplate stresses seen upon loading. Several studies have found that the positioning of implants plays a significant role in the stresses seen at the endplate-implant interface. For example, Tsuang *et al*. found that endplate stresses using a single cage versus double cage are not significantly different when utilizing posterior fixation; however, loads in the posterior rods increase significantly when using a single cage. Additionally, their study found that the orientation of a single PLIF cage during insertion can significantly affect endplate stresses.[88] A single cage placed obliquely across the midline of the endplate leads to lower endplate stresses compared to a unilateral insertion of the same cage due to symmetrical loading across the vertebral plate. These factors must be accounted for when designing implants; however, in the case of this study with ALIF implants, these confounders are minimized by the large footprint of the implant.

Interestingly, this study found that increasing porosity of the material did little to reduce endplate stresses with the exception of the traditional porous cage. This is likely due to the greater effect of contact area compared to material changes on endplate stresses. The results from this study initially seem to contrast with previous investigations in porous lumbar fusion cages, which have found that material changes significantly affect the endplate stresses. However, the majority of these studies have utilized traditional cage designs, which inherently have lower contact areas with the bone, so the results seen in this study actually follow the trends described previously. For example, Zhang *et al*. found that in a traditional cage, using porous titanium significantly reduced endplate stresses by more closely matching the endplate properties. However, as these cages utilized porous titanium with the most porous cage having a modulus of 675 MPa, higher than the materials tested in this study; they may not reach the

diminishing return of reducing modulus as described in this study.[99] Adam *et al*. proposed a bending beam analogy for endplate properties and stated that the total bending stiffness of the endplate and implant be compared rather than simply the elastic modulus.[100] This phenomenon could describe the results seen in this study, as varying the material properties of an implant would significantly affect its bending stiffness making it more closely match the bending stiffness of the endplate. For example, the surface porous implants created higher endplate stresses than the fully porous materials similar to those of the solid implant, which is likely due to their increased bending stiffness relative to the endplate. Further, by introducing implant conformity, this phenomenon is reduced as the endplate no longer has to bend in relation to the implant; rather, the loads are transferred evenly in an axial direction through the endplate.

This study found that porous implants tended to have lower apparent internal stresses than those seen in the solid cages of the same design type. This is likely due to the decreased modulus of the porous material compared to the solid implants. Previous studies have found similar results when comparing porous and solid titanium cages. Zhang et. al found porous titanium cages showed significantly lower maximum stresses compared to solid cages in a finite element model of the lumbar spine with solid implants showing approximately 45 MPa under flexion compared to porous implants showing a maximum stress of 8.64 MPa. The study also found that a solid PEEK implant would experience approximately 10 MPa under flexion and bending, which closely matches the implant stresses seen in the solid implants used in this study.[99] In the case of the filled and conformed implants, varying material properties had little effect on implant stresses. This is likely due to all loading of the implant being directly transferred through the material and a lack of stress concentration points at the bone-implant interface. Similar responses were noted by Tsuang *et al*. where single cages showed

significantly higher stress than paired cages.[88] Though it was also found that a single cage placed obliquely across the endplate provided the lowest stresses, this is likely due to the cage better being able to fit the concavity of the endplate compared to individual cages. These studies also only reported the maximum stress seen in the implant, which can skew results in cases of stress concentrations within the model.

Of special interest in this study was the behavior of the surface porous implant. The stress within the body was found to be higher than the traditional solid implant, and the stresses within the porous portion of the implant were higher than the traditional porous implant. Load applied across the top of the implant is directly transferred into the porous portion of the implant which then applies load to the endplate. This is likely due to more of the stress being applied to a smaller number of elements in the thin porous layer of the implant and all of the stress being applied to the body of the solid portion evenly.

As measured from finite-element models of porous scaffolds, it was found that the stress concentration factor within porous implants can be as high as 15 times the applied apparent stress on the implant which is in agreement with previously published research.[101] The long-term implantation viability of porous polymeric implants is still a topic of discussion as they tend to have issues with cyclic fatigue and densification of the pores. In the case of this study, based on implant stresses seen, it can be deduced that they are not suitable for use in a high load use case as seen in the lumbar spine. Namely, the traditional porous implants would rapidly fatigue and fracture due to their relatively small cross-sectional area. In order to utilize porous implants, they would naturally be designed in a manner similar to the filled implants tested in this study. To further extend the life of these implants, a conformed design should be used with porous materials to minimize both endplate stress as well as the stress within the implant. The results

from this study demonstrated that a fully porous conformed cage could effectively provide support and reduce implant subsidence by reducing endplate stresses. It should be noted that implant body stresses calculated in this study assumed a solid geometry with the apparent modulus of a porous material applied. A porous material will have areas of significantly increased stress at the edges its pores due to reduced material thickness at the pore margins which significantly affects predictions of the fatigue limit in porous materials.

As this study was specific to ALIF cages, these results may change when comparing designs of other cages such as those used in PLIF or TLIF procedures, though it is expected that the fundamental results would be similar in those cases. Additionally, this study focused on strictly axial loading to analyze endplate stresses when in clinical application, there are various complex loading patterns which can be seen in the lumbar spine. Future research could examine the effect of cage design and implant material during these load cases.

In conclusion, the results from this study provided valuable insight into the use of porous and contoured implants for lumbar interbody fusion. The results suggest that the use of conformed implants is most effective method for reducing endplate stresses and, as a result, decreasing the risk of subsidence. Additionally, this study found that varying material properties for a single implant type did not strongly affect endplate stress. With these considerations, future implants should focus on providing a more contoured surface to match the endplate geometry, maximizing endplate contact to reduce subsidence.

CHAPTER V

CONCLUSIONS AND FUTURE WORK

The overarching goal of this research was to investigate the feasibility of a fully porous, patient-specific poly(para-phenylene) spinal cage for lumbar interbody fusion. It developed and utilized a novel indentation method for measurement of endplate mechanical properties, which have not been previously reported in literature. This research also was the first to demonstrate the osseointegrative behavior of porous PPP scaffolds in-vivo, showing its potential as an orthopedic biomaterial and providing vital information of the behavior of bone in these porous implants. Using the information garnered about the mechanical behavior of the endplate and the biological behavior of bone within these porous scaffolds, a model was developed which allowed for the prediction of endplate stresses utilizing various materials and implant designs. These studies provide significant insight into the mechanical behavior of porous materials in orthopedic applications, and provide guidance for optimal implant designs.

Chapter II in this study proposed and developed several predictive models for endplate mechanical properties, specifically endplate stiffness, Brinell hardness, and apparent elastic modulus. This study utilized a novel indentation method validated on simulated bone to directly measure endplate mechanical properties on a scale relevant to implant design. Additionally, it demonstrated that it is possible to non-invasively predict endplate properties using demographic and radiographic data. With the ability to predict stiffness (N/mm), surgeons can determine optimal implant placement to avoid areas of low stiffness which are susceptible to subsidence. In addition, this study demonstrated that the structural effect of the underlying cancellous bone as well as the lack of cortical bone support from the outer shell of the vertebra leads to significantly reduced modulus compared to grayscale-based properties. Further, the modulus

was found to also be correlated with time dependent creep behavior of the endplate. Low modulus areas of the endplate tended to show more deformation over time compared to higher modulus areas.

The first in-vivo ingrowth experiment utilizing porous PPP was presented in Chapter 3. The study analyzed the amount of bone ingrowth in a porous PPP implant and found that PPP permitted significantly more ingrowth compared to porous PEEK implants with approximately 76% of the pore volume filled with bone compared to PEEK which showed approximately 49% ingrowth. Additionally, it characterized the mechanical behavior of PPP scaffolds with bone ingrowth, finding that the apparent modulus of a PPP cube will converge to approximately 9,800 MPa with 100% bone ingrowth and higher porosity samples show a delayed increase in modulus during bone ingrowth as demonstrated by the 85% porous PPP implant. Furthermore, the load sharing characteristics of the implant with bone ingrowth were analyzed and found that higher porosity implants transferred more load to the bone at lower ingrowth levels compared to lower porosity implants, allowing implant scaffolds to be designed in a manner which promotes bone ingrowth via additional loading to the bone. Finite element push-out testing of the porous implants showed that there was an identical load sharing response between porous PPP and PEEK implants, further solidifying the potential of PPP as an orthopedic biomaterial.

Finally, Chapter IV described a multifaceted approach to implant stress modelling, utilizing patient-specific properties, novel implant designs, and analysis of a novel material for lumbar interbody cages. It was found that material variation, such as porosity, tends to have a diminished effect at lower moduli and matching the material properties to the endplate leads to negligible improvements in endplate stress. It was found that the largest factor in reducing endplate stress is contouring of the implant to the endplate to maximize contact area with

contoured implants reducing average endplate stress by at least 50%. Additionally, it was found that contoured implants result in the lowest average stresses for any implant design, and utilizing a porous material would inherently require a contoured cage to minimize implant stresses for long-term implantation to prevent fatigue. The results from this study concluded that applying a patient specific approach by matching endplate properties was not a practical method to reduce endplate stresses as the reduction in endplate stress was approximately 1% compared to the same geometry solid material. Though these results ultimately found that patient specific porous PPP implants do not provide the reduction in endplate stresses as hypothesized, the results provide valuable insight into the behavior of porous materials in orthopedic applications and can help to guide future research and implant designs.

Future Research Suggestions

The final study in this research utilized a finite element approach to determine the best implant for minimizing endplate stresses; however, as was noted in the initial study, the behavior of cadaveric bone can be significantly different from the methods used in modeling. As such, it would be recommended to perform an in-vitro cadaveric study of the various implants to determine the best design. Additionally, the study utilized vertebrae from a patient with normal bone mineral density and without any severe endplate pathologies. These factors could play a significant role in the behavior of implants, and future research could focus on evaluation of contoured implants in cases of endplate defects or osteoporotic patients. The methods utilized in the final study could directly be applied to these cases. For this case, a copy of the MATLAB code used to apply patient specific properties is included in the Appendix.

Additionally, while the final study did not utilize the bone ingrowth modeling described in Chapter 3, those methods could be applied in analyzing stresses within the vertebra as well as

range of motion studies of various implant designs with bone ingrowth. The results from this research would yield valuable data in determining the effect of various implant materials on the stability of the fusion constructs during bone ingrowth prior to a successful fusion.

REFERENCES

Spinal Implants US 2015 Market Analysis. Toronto, Ontario July, 2015 2015. RPUS20SP15.

Marchi L, Abdala N, Oliveira L, Amaral R, Coutinho E, Pimenta L. Radiographic and clinical evaluation of cage subsidence after stand-alone lateral interbody fusion. *Journal of neurosurgery Spine.* 2013;19(1):110-118.

Joseph JR, Smith BW, La Marca F, Park P. Comparison of complication rates of minimally invasive transforaminal lumbar interbody fusion and lateral lumbar interbody fusion: a systematic review of the literature. *Neurosurgical focus.* 2015;39(4):E4.

Vadapalli S, Sairyo K, Goel VK, et al. Biomechanical rationale for using polyetheretherketone (PEEK) spacers for lumbar interbody fusion–a finite element study. *Spine.* 2006;31(26):E992-E998.

Sato T, Yonezawa I, Todo M, Takano H, Kaneko K. Use of Nonlinear Finite Element Analysis of Bone Density to Investigate the Biomechanical Effect in the Bone around Intervertebral Cages in Posterior Lumbar Interbody Fusion. *Journal of Biomedical Science and Engineering.* 2017;10(10):445.

Wymysłowski P, Zagrajek T. Bone Remodelling Model Incorporating Both Shape and Internal Structure Changes by Three Different Reconstruction Mechanisms. A Lumbar Spine Case. *Archive of Mechanical Engineering.* 2016;63(4):549-563.

Choi JY, Sung KH. Subsidence after anterior lumbar interbody fusion using paired stand-alone rectangular cages. *European Spine Journal.* 2006;15(1):16-22.

van Dijk M, Smit TH, Sugihara S, Burger EH, Wuisman PI. The effect of cage stiffness on the rate of lumbar interbody fusion: an in vivo model using poly (l-lactic Acid) and titanium cages. *Spine.* 2002;27(7):682-688.

van Dijk M, Smit TH, Arnoe MF, Burger EH, Wuisman PI. The use of poly-L-lactic acid in lumbar interbody cages: design and biomechanical evaluation in vitro. *European Spine Journal.* 2003;12(1):34-40.

Lam FC, Alkalay R, Groff MW. The Effects of Design and Positioning of Carbon Fiber Lumbar Interbody Cages and Their Subsidence in Vertebral Bodies. *Journal of Spinal Disorders & Techniques.* 2012;25(2):116-122.

Evans NT, Torstrick FB, Lee CS, et al. High-strength, surface-porous polyether-ether-ketone for load-bearing orthopedic implants. *Acta biomaterialia.* 2015;13:159-167.

Bashkuev M, Checa S, Postigo S, Duda G, Schmidt H. Computational analyses of different intervertebral cages for lumbar spinal fusion. *J Biomech.* 2015;48(12):3274-3282.

Melton GH, Peters EN, Arisman RK. 2 - Engineering Thermoplastics. In: Kutz M, ed. *Applied Plastics Engineering Handbook.* Oxford: William Andrew Publishing; 2011:7-21.

Frick CP, DiRienzo AL, Hoyt AJ, et al. High-strength poly(para-phenylene) as an orthopedic biomaterial. *J Biomed Mater Res A.* 2014;102(9):3122-3129.

DiRienzo AL, Yakacki CM, Frensemeier M, et al. Porous poly(para-phenylene) scaffolds for load-bearing orthopedic applications. *J Mech Behav Biomed Mater.* 2014;30:347-357.

Hoyt AJ, Yakacki CM, Fertig RS, 3rd, Dana Carpenter R, Frick CP. Monotonic and cyclic loading behavior of porous scaffolds made from poly(para-phenylene) for orthopedic applications. *J Mech Behav Biomed Mater.* 2015;41:136-148.

Noshchenko A, Hoffecker L, Lindley EM, Burger EL, Cain CM, Patel VV. Long-term Treatment Effects of Lumbar Arthrodeses in Degenerative Disk Disease: A Systematic Review With Meta-Analysis. *J Spinal Disord Tech.* 2015;28(9):E493-521.

Cahill KS, Chi JH, Day A, Claus EB. Prevalence, complications, and hospital charges associated with use of bone-morphogenetic proteins in spinal fusion procedures. *Jama.* 2009;302(1):58-66.

McInnis MM, Olchanski N, Kemner JE, Goss T. PMS17 BUDGET IMPACT OF NEW RHBMP-2 FORMULATION IN PATIENTS UNDERGOING POSTEROLATERAL SPINAL FUSION PROCEDURES FOR DEGENERATIVE DISC DISEASE IN RANDOMIZED CONTROLLED TRIAL (RCT). *Value in Health.*13(7):A305.

Carreon LY, Glassman SD, Djurasovic M, et al. RhBMP-2 versus iliac crest bone graft for lumbar spine fusion in patients over 60 years of age: a cost-utility study. *Spine.* 2009;34(3):238-243.

Glassman SD, Carreon LY, Djurasovic M, et al. RhBMP-2 versus iliac crest bone graft for lumbar spine fusion: a randomized, controlled trial in patients over sixty years of age. *Spine.* 2008;33(26):2843-2849.

Alvin MD, Lubelski D, Abdullah KG, Whitmore RG, Benzel EC, Mroz TE. Cost-Utility Analysis of Instrumented Fusion Versus Decompression Alone for Grade I L4–L5 Spondylolisthesis at 1-Year Follow-up: A Pilot Study. *Clinical spine surgery.* 2016;29(2):E80-E86.

Deyo RA, Martin BI, Kreuter W, Jarvik JG, Angier H, Mirza SK. Revision surgery following operations for lumbar stenosis. *The Journal of bone and joint surgery American volume.* 2011;93(21):1979.

Marchi L, Oliveira L, Coutinho E, Pimenta L. Results and complications after 2-level axial lumbar interbody fusion with a minimum 2-year follow-up. *Journal of Neurosurgery: Spine.* 2012;17(3):187-192.

Rodriguez AG, Rodriguez-Soto AE, Burghardt AJ, Berven S, Majumdar S, Lotz JC. Morphology of the human vertebral endplate. *Journal of Orthopaedic Research.* 2012;30(2):280-287.

Hulme PA, Boyd SK, Ferguson SJ. Regional variation in vertebral bone morphology and its contribution to vertebral fracture strength. *Bone.*41(6):946-957.

Fields AJ, Costabal FS, Rodriguez AG, Lotz JC. Seeing double: A comparison of microstructure, biomechanical function, and adjacent disc health between double-layer and single-layer vertebral endplates. *Spine.* 2012;37(21):E1310-E1317.

Class II Special Controls Guidance Document: Intervertebral Body Fusion Device. In: Health CfDaR, ed: Food and Drug Administration; 2007.

Dall'Ara E, Karl C, Mazza G, et al. Tissue properties of the human vertebral body sub-structures evaluated by means of microindentation. *Journal of the mechanical behavior of biomedical materials.* 2013;25:23-32.

Grant J, Oxland TR, Dvorak MF, Fisher CG. The effects of bone density and disc degeneration on the structural property distributions in the lower lumbar vertebral endplates. *Journal of orthopaedic research.* 2002;20(5):1115-1120.

Grant JP, Oxland TR, Dvorak MF. Mapping the structural properties of the lumbosacral vertebral endplates. *Spine.* 2001;26(8):889-896.

Noshchenko A, Plaseied A, Patel VV, Burger E, Baldini T, Yun L. Correlation of vertebral strength topography with 3-dimensional computed tomographic structure. *Spine.* 2013;38(4):339-349.

Liebschner MA, Kopperdahl DL, Rosenberg WS, Keaveny TM. Finite element modeling of the human thoracolumbar spine. *Spine.* 2003;28(6):559-565.

Oliver WC, Pharr GM. An improved technique for determining hardness and elastic modulus using load and displacement sensing indentation experiments. *Journal of materials research.* 1992;7(6):1564-1583.

Oliver WC, Pharr GM. Measurement of hardness and elastic modulus by instrumented indentation: Advances in understanding and refinements to methodology. *Journal of materials research.* 2004;19(1):3-20.

Zhang J, Niebur GL, Ovaert TC. Mechanical property determination of bone through nano-and micro-indentation testing and finite element simulation. *Journal of biomechanics.* 2008;41(2):267-275.

Rouleau L. *Modélisation vibro-acoustique de structures sandwich munies de matériaux visco-élastiques*, Conservatoire national des arts et metiers-CNAM; 2013.

ISO E. 6506-1: 2008. Metallic materials-Brinell hardness test-Part 1: Test method. In: Warszawa, Polish Committee for Standardization; 2008.

Glantz SA. *Primer of biostatistics.* McGraw Hill Professional; 2012.

Oh KW, Lee JH, Lee J-H, Lee D-Y, Shim HJ. The Correlation Between Cage Subsidence, Bone Mineral Density, and Clinical Results in Posterior Lumbar Interbody Fusion. *Clinical Spine Surgery.* 2017;30(6):E683-E689.

Tempel ZJ, Gandhoke GS, Okonkwo DO, Kanter AS. Impaired bone mineral density as a predictor of graft subsidence following minimally invasive transpsoas lateral lumbar interbody fusion. *European Spine Journal.* 2015;24(3):414-419.

Zhang Jd, Poffyn B, Sys G, Uyttendaele D. Are stand-alone cages sufficient for anterior lumbar interbody fusion? *Orthopaedic surgery.* 2012;4(1):11-14.

Oxland TR, Grant JP, Dvorak MF, Fisher CG. Effects of endplate removal on the structural properties of the lower lumbar vertebral bodies. *Spine.* 2003;28(8):771-777.

Dall'Ara E, Pahr D, Varga P, Kainberger F, Zysset P. QCT-based finite element models predict human vertebral strength in vitro significantly better than simulated DEXA. *Osteoporosis International.* 2012;23(2):563-572.

Noshchenko A, Xianfeng Y, Armour GA, et al. Evaluation of spinal instrumentation rod bending characteristics for in-situ contouring. *Journal of Biomedical Materials Research Part B: Applied Biomaterials.* 2011;98(1):192-200.

Alloys S. Aerospace Materials Specifications for Titanium & Titanium Alloys. 2015; http://www.supraalloys.com/specs.php. Accessed 10/31/2017, 2017.

Sen I, Ramamurty U. Elastic modulus of Ti–6Al–4V–xB alloys with B up to 0.55 wt.%. *Scripta materialia.* 2010;62(1):37-40.

Rho J-Y, Tsui TY, Pharr GM. Elastic properties of human cortical and trabecular lamellar bone measured by nanoindentation. *Biomaterials.* 1997;18(20):1325-1330.

Zysset PK, Guo XE, Hoffler CE, Moore KE, Goldstein SA. Elastic modulus and hardness of cortical and trabecular bone lamellae measured by nanoindentation in the human femur. *Journal of biomechanics.* 1999;32(10):1005-1012.

Millenium Research Group. *Spinal Implants | US | 2015 | Market Analysis.* 2015.

Beutler WJ, Peppelman WC, Jr. Anterior lumbar fusion with paired BAK standard and paired BAK Proximity cages: subsidence incidence, subsidence factors, and clinical outcome. *Spine J.* 2003;3(4):289-293.

Kim MC, Chung HT, Cho JL, Kim DJ, Chung NS. Subsidence of polyetheretherketone cage after minimally invasive transforaminal lumbar interbody fusion. *J Spinal Disord Tech.* 2013;26(2):87-92.

Chrastil J, Patel AA. Complications associated with posterior and transforaminal lumbar interbody fusion. *J Am Acad Orthop Surg.* 2012;20(5):283-291.

Ryan G, Pandit A, Apatsidis DP. Fabrication methods of porous metals for use in orthopaedic applications. *Biomaterials.* 2006;27(13):2651-2670.

Navarro M, Michiardi A, Castano O, Planell JA. Biomaterials in orthopaedics. *J R Soc Interface.* 2008;5(27):1137-1158.

Davies JE. Mechanisms of endosseous integration. *Int J Prosthodont.* 1998;11(5):391-401.

Franchi M, Fini M, Martini D, et al. Biological fixation of endosseous implants. *Micron.* 2005;36(7-8):665-671.

Ramp LC, Jeffcoat RL. Dynamic behavior of implants as a measure of osseointegration. *Int J Oral Maxillofac Implants.* 2001;16(5):637-645.

Turkyilmaz I, Sennerby L, McGlumphy EA, Tozum TF. Biomechanical aspects of primary implant stability: a human cadaver study. *Clin Implant Dent Relat Res.* 2009;11(2):113-119.

Berglundh T, Abrahamsson I, Lang NP, Lindhe J. De novo alveolar bone formation adjacent to endosseous implants. *Clin Oral Implants Res.* 2003;14(3):251-262.

Vardavoulias M, Jouannytresy C, Jeandin M. Sliding-Wear Behavior of Ceramic Particle-Reinforced High-Speed Steel Obtained by Powder-Metallurgy. *Wear.* 1993;165(2):141-149.

Davim JP, Reis P, Lapa V, Antonio CC. Machinability study on polyetheretherketone (PEEK) unreinforced and reinforced (GF30) for applications in structural components. *Compos Struct.* 2003;62(1):67-73.

Martin AC, Lakhera N, DiRienzo AL, et al. Amorphous-to-crystalline transition of Polyetheretherketone–carbon nanotube composites via resistive heating. *Composites Science and Technology.* 2013;89:110-119.

Burstone CJ, Liebler SA, Goldberg AJ. Polyphenylene polymers as esthetic orthodontic archwires. *Am J Orthod Dentofacial Orthop.* 2011;139(4 Suppl):e391-398.

Vuorinen AM, Dyer SR, Vallittu PK, Lassila LV. Effect of water storage on the microtensile bond strength of composite resin to dentin using experimental rigid rod polymer modified primers. *J Adhes Dent.* 2011;13(4):333-340.

Vuorinen AM, Dyer SR, Lassila LVJ, Vallittu PK. Bonding of BisGMA-TEGDMA-Resin to Bulk Poly(Paraphenylene) Based Rigid Rod Polymer. *Compos Interface.* 2011;18(5):387-398.

Chatham LS, Patel VV, Yakacki CM, Dana Carpenter R. Interbody Spacer Material Properties and Design Conformity for Reducing Subsidence During Lumbar Interbody Fusion. *J Biomech Eng.* 2017;139(5).

Zhu BH, He XF, Zhao TL. Friction and wear characteristics of natural bovine bone lubricated with water. *Wear.* 2015;322:91-100.

Feerick EM, Kennedy J, Mullett H, FitzPatrick D, McGarry P. Investigation of metallic and carbon fibre PEEK fracture fixation devices for three-part proximal humeral fractures. *Med Eng Phys.* 2013;35(6):712-722.

Wagner DW, Lindsey DP, Beaupre GS. Deriving tissue density and elastic modulus from microCT bone scans. *Bone.* 2011;49(5):931-938.

Akin FA, Zreiqat H, Jordan S, Wijesundara MB, Hanley L. Preparation and analysis of macroporous TiO2 films on Ti surfaces for bone-tissue implants. *J Biomed Mater Res.* 2001;57(4):588-596.

Karageorgiou V, Kaplan D. Porosity of 3D biomaterial scaffolds and osteogenesis. *Biomaterials.* 2005;26(27):5474-5491.

Albrektsson T, Wennerberg A. Oral implant surfaces: Part 2--review focusing on clinical knowledge of different surfaces. *Int J Prosthodont.* 2004;17(5):544-564.

Puleo DA, Thomas MV. Implant surfaces. *Dent Clin North Am.* 2006;50(3):323-338, v.

Kale S, Biermann S, Edwards C, Tarnowski C, Morris M, Long MW. Three-dimensional cellular development is essential for ex vivo formation of human bone. *Nat Biotechnol.* 2000;18(9):954-958.

Ferrera D, Poggi S, Biassoni C, et al. Three-dimensional cultures of normal human osteoblasts: proliferation and differentiation potential in vitro and upon ectopic implantation in nude mice. *Bone.* 2002;30(5):718-725.

Futami T, Fujii N, Ohnishi H, et al. Tissue response to titanium implants in the rat maxilla: ultrastructural and histochemical observations of the bone-titanium interface. *J Periodontol.* 2000;71(2):287-298.

Meyer U, Joos U, Mythili J, et al. Ultrastructural characterization of the implant/bone interface of immediately loaded dental implants. *Biomaterials.* 2004;25(10):1959-1967.

Mavrogenis AF, Dimitriou R, Parvizi J, Babis GC. Biology of implant osseointegration. *J Musculoskelet Neuronal Interact.* 2009;9(2):61-71.

Oonishi H, Yamamoto M, Ishimaru H, et al. The effect of hydroxyapatite coating on bone growth into porous titanium alloy implants. *J Bone Joint Surg Br.* 1989;71(2):213-216.

Vadapalli S, Sairyo K, Goel VK, et al. Biomechanical rationale for using polyetheretherketone (PEEK) spacers for lumbar interbody fusion-A finite element study. *Spine (Phila Pa 1976).* 2006;31(26):E992-998.

Fujibayashi S, Takemoto M, Neo M, et al. A novel synthetic material for spinal fusion: a prospective clinical trial of porous bioactive titanium metal for lumbar interbody fusion. *Eur Spine J.* 2011;20(9):1486-1495.

Carpenter RD, Klosterhoff BS, Torstrick FB, et al. Effect of porous orthopaedic implant material and structure on load sharing with simulated bone ingrowth: A finite element analysis comparing titanium and PEEK. *Journal of the mechanical behavior of biomedical materials.* 2018;80:68-76.

Lee Y-H, Chung C-J, Wang C-W, et al. Computational comparison of three posterior lumbar interbody fusion techniques by using porous titanium interbody cages with 50% porosity. *Computers in biology and medicine.* 2016;71:35-45.

Sato T, Yonezawa I, Todo M, Takano H, Kaneko K. Biomechanical Effects of Implant Materials on Posterior Lumbar Interbody Fusion: Comparison of Polyetheretherketone and Titanium Spacers Using Finite Element Analysis and Considering Bone Density. *Journal of Biomedical Science and Engineering.* 2018;11(04):45.

Chatham LS, Patel VV, Yakacki CM, Dana Carpenter R. Interbody Spacer Material Properties and Design Conformity for Reducing Subsidence During Lumbar Interbody Fusion. *Journal of Biomechanical Engineering.* 2017;139(5):0510051-0510058.

Steffen T, Tsantrizos A, Aebi M. Effect of implant design and endplate preparation on the compressive strength of interbody fusion constructs. *Spine.* 2000;25(9):1077-1084.

Tsuang Y-H, Chiang Y-F, Hung C-Y, Wei H-W, Huang C-H, Cheng C-K. Comparison of cage application modality in posterior lumbar interbody fusion with posterior instrumentation—A finite element study. *Medical engineering & physics.* 2009;31(5):565-570.

Matsuura P, Waters RL, Adkins RH, Rothman S, Gurbani N, Sie I. Comparison of computerized tomography parameters of the cervical spine in normal control subjects and spinal cord-injured patients. *J Bone Joint Surg Am.* 1989;71(2):183-188.

Patel RR, Noshchenko A, Dana Carpenter R, et al. Evaluation and Prediction of Human Lumbar Vertebrae Endplate Mechanical Properties Using Indentation and Computed Tomography. *Journal of Biomechanical Engineering.* 2018;140(10):101011-101011-101019.

Bergmann G. OrthoLoad. In: Berlin CU, ed2008.

Homminga J, Weinans H, Gowin W, Felsenberg D, Huiskes R. Osteoporosis Changes the Amount of Vertebral Trabecular Bone at Risk of Fracture but Not the Vertebral Load Distribution. *Spine.* 2001;26(14):1555-1560.

Gibson LJ, Ashby MF. *Cellular solids: structure and properties.* Cambridge university press; 1999.

Spetzger U, Frasca M, König SA. Surgical planning, manufacturing and implantation of an individualized cervical fusion titanium cage using patient-specific data. *European Spine Journal.* 2016;25(7):2239-2246.

de Beer N, Scheffer C. Reducing subsidence risk by using rapid manufactured patient-specific intervertebral disc implants. *The Spine Journal.* 2012;12(11):1060-1066.

Betz R, Denoziere G. Patient-specific spinal implants and related systems and methods. In: Google Patents; 2012.

Kumar N, Judith MR, Kumar A, Mishra V, Robert MC. Analysis of stress distribution in lumbar interbody fusion. *Spine.* 2005;30(15):1731-1735.

Polikeit A, Ferguson SJ, Nolte LP, Orr TE. Factors influencing stresses in the lumbar spine after the insertion of intervertebral cages: finite element analysis. *European Spine Journal.* 2003;12(4):413-420.

Zhang Z, Li H, Fogel GR, Liao Z, Li Y, Liu W. Biomechanical Analysis of Porous Additive Manufactured Cages for Lateral Lumbar Interbody Fusion: A Finite Element Analysis. *World Neurosurg.* 2018;111:e581-e591.

Adam C, Pearcy M, McCombe P. Stress analysis of interbody fusion—finite element modelling of intervertebral implant and vertebral body. *Clinical Biomechanics.* 2003;18(4):265-272.

Maîtrejean G, Terriault P, Devís Capilla D, Brailovski V. Unit cell analysis of the superelastic behavior of open-cell tetrakaidecahedral shape memory alloy foam under quasi-static loading. *Smart Materials Research.* 2014;2014.

APPENDIX

Appended below is the code used to apply patient specific material properties to the endplate by writing a new ABAQUS INP file.

```
close all
clear
clc
%%Open File and convert it into a long cell array for indexing
[targetFile,targetPath] = uigetfile('*','Select input file (.inp)');
inFile = fopen([targetPath targetFile]);
originalFile = textscan(inFile, '%s', 'Delimiter','\n', 'CollectOutput',true );
originalFile=originalFile{1,1};
fclose(inFile);
originalLength = length(originalFile);

PartName=input('enter name of endplate part from INP file:','s');
nameLength=length(PartName);
%%search file for node data beginning and end
searchString = '**NODE DATA BEGIN';
stopString = '**NODE DATA END';
NodeBeginSearch = strncmp(searchString,originalFile,17);
NodeBeginLine=find(NodeBeginSearch==1)+6;%% Beginning of node data is 6 lines after
NODE DATA BEGIN
NodeEndSearch=strncmp(stopString,originalFile,15);
NodeEndLine=find(NodeEndSearch==1)-2;%%End of Node Data is 2 lines before NODE
DATA END

%%extract Node Data and put it into a matrix
nDataCells=originalFile(NodeBeginLine:NodeEndLine);
nData=[];
tic
for i=1:length(nDataCells)
   NodeCellLine=str2num(nDataCells{i});
```

```
    nData=[nData; NodeCellLine];
end
toc

ElemStartString = ['**ELEMENTS (TETRAHEDRA) - Part: ' PartName ' BEGIN'];
ElemStopString = ['**ELEMENTS (TETRAHEDRA) - Part: ' PartName ' END'];
ElemBeginSearch = strncmp(ElemStartString,originalFile,length(ElemStartString));
ElemBeginLine=find(ElemBeginSearch==1)+2;
ElemEndSearch=strncmp(ElemStopString,originalFile,length(ElemStopString));
ElemEndLine=find(ElemEndSearch==1)-1;

ElemData=originalFile(ElemBeginLine:ElemEndLine);
ElemInput={};
ElemMatrix=[];
tic
for i=1:length(ElemData)
    matIndex=i;
    ElemRow=str2num(ElemData{i});
    elenum=ElemRow(1);
    ElemText=[{['**ELEMENTS - Part: ' 'EP' PartName(1:2) '_' num2str(elenum) ' BEGIN']};...
            {['**Part Material: ' PartName '_' num2str(elenum)]};...
            {['**Material ID: PM' PartName '_' num2str(elenum)]};...
            {['**Material Index: ' num2str(matIndex)]};...

{'**============================================================================
============'};...
            {['**ELEMENTS (TETRAHEDRA) - Part: ' 'EP' PartName(1:2) '_' num2str(elenum) '
BEGIN']};...
            {['*ELEMENT, TYPE=C3D4, ELSET=PT_' PartName(1:2) '_' num2str(elenum)]};...
            ElemData{i};
            {['**ELEMENTS (TETRAHEDRA) - Part: ' 'EP' PartName(1:2) '_' num2str(elenum) '
END']};...
```

```
{'**==========
==========='};...
        {['**ELEMENTS - Part: ' 'EP' PartName(1:2) '_' num2str(elenum) ' END']};...

{'**==========
==========='};...

{'**==========
==========='};...
        ];
   ElemInput=[ElemInput;ElemText];
   ElemMatrix=[ElemMatrix; ElemRow];
end
toc

newElemfilebegin=originalFile(1:ElemBeginLine-8);
newElemfileend=originalFile(ElemEndLine+6:end);

ElemINP=[newElemfilebegin; ElemInput; newElemfileend];


load C130365Points
F=scatteredInterpolant(L2x,L2y,L2mod,'natural');

% load SpinePoints
% if PartName(1:2)=='L1'
%     F=scatteredInterpolant(L1Pointsx,L1Pointsy,L1mod,'natural');
% elseif PartName(1:2)=='L2'
%     F=scatteredInterpolant(L2Pointsx,L2Pointsy,L2mod,'natural');
% end

capspart=upper(PartName);
MatBeginString=['*SOLID SECTION, ELSET=PT_' capspart ', MATERIAL=PM_' capspart];
```

```
MatBeginSearch=strncmp(MatBeginString,ElemINP,length(MatBeginString));
MatBeginLine=find(MatBeginSearch==1)-4;
MatEndLine=find(MatBeginSearch==1)+4;
MatInput=[];
elemxcoords=[];
elemycoords=[];
elemodout=[];
for j=1:length(ElemMatrix)
   elenum=ElemMatrix(j,1);
   elemx=nData(ElemMatrix(j,2),2);
   elemy=nData(ElemMatrix(j,2),3);
   elemod=F(elemx,elemy);
   MatText=[{'**MATERIAL DEFINITION BEGIN'};...
         {['**Part: ' 'EP' PartName(1:2) '_' num2str(elenum) ' BEGIN']};...
         {['**Part Material: ' PartName '_' num2str(elenum)]};...
         {['*SOLID SECTION, ' 'ELSET=PT_' PartName(1:2) '_' num2str(elenum) ', '
'MATERIAL=PM' PartName(1:2) '_' num2str(elenum)]};...
         {['*MATERIAL, NAME=PM' PartName(1:2) '_' num2str(elenum)]};...
         {'*ELASTIC, TYPE=ISOTROPIC'};...
         {[num2str(elemod) ', 0.3']};...
         {'*DENSITY'};...
         {'1.00,'};...
         {'**MATERIAL DEFINITION END'};...

{'**=============================================================================
============'};...

{'**=============================================================================
============'}];
    MatInput=[MatInput;MatText];
    elemxcoords=[elemxcoords elemx];
    elemycoords=[elemycoords elemy];
    elemodout=[elemodout elemod];
end
```

```
NewMatFileBegin=ElemINP(1:MatBeginLine);
NewMatFileEnd=ElemINP(MatEndLine:end);

NewINP=[NewMatFileBegin;MatInput;NewMatFileEnd];




INPFilename=[targetFile(1:end-3) '_' PartName '.inp'];
outfile=fopen([targetPath INPFilename],'wt');
fprintf(outfile,'%s\n',NewINP{:});
fclose(outfile)

load handel
sound(y(1:16000),8000)

% for i=1:originalLength
%     if GSMaterialLines(i)==1
%         nData=[nData;i+4];
%     end
%     if strncmp(stopString,originalFile{1,1}{i,1},17) == 1
%         break;
%     end
% end
```